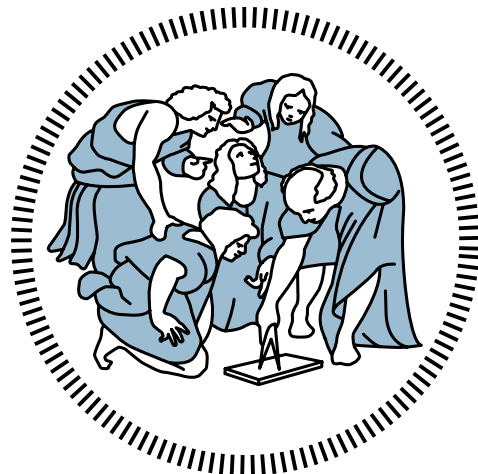


AUTOMATED TRAJECTORY REFINEMENT OF THREE-BODY ORBITS
IN THE REAL SOLAR SYSTEM MODEL

DIOGENE ALESSANDRO DEI TOS



POLITECNICO
MILANO 1863

Dynamical substitutes of Lagrangian points and quasi-periodic orbits about them

Master of Science
Department of Aerospace Science and Technology
Space Engineering
Politecnico di Milano

July 2014

Diogene Alessandro Dei Tos: *Automated trajectory refinement of three-body orbits in the real solar system model*, Dynamical substitutes of Lagrangian points and quasi-periodic orbits about them, Master of Science

SUPERVISOR:

Dr. Francesco Topputo

LOCATION:

Milano

TIME FRAME:

July 2014

Copyright © July 2014 Diogene Alessandro Dei Tos

All Rights Reserved

*Ohana means family.
Family means nobody gets left behind, or forgotten.*
— Lilo & Stitch —

Dedicated to the memory of my grandfather Gelindo, who taught me that being a man sometimes means give up. Shall his memory never fade from this world.

ABSTRACT

The restricted three-body problem (RTBP) is the ideal model to design unique solutions, ranging from Lagrange point orbits to low energy transfers. These orbits embed the effect of two gravitational attractions in a natural way, and therefore they are more accurate than the conics, solutions of the classic two-body problem. However, when three-body orbits are reproduced in the real solar system model, large errors are found. That is, as the three-body orbits are defined in the regions of phase space where the sensitivity is high, the additional terms of the real solar system model produce large effects along the orbits.

The core of this thesis is to present an automatic algorithm for the correction of orbits in the real solar system. The differential equations governing the dynamics of a massless particle are written as perturbation of the RTBP in a nonuniformly rotating and pulsating frame by using a Lagrangian formalism. The refinement is carried out by means of a multiple shooting technique, and the problem is solved for a finite set of variables. The generality of the algorithm lies in the possibility of handling both constrained and unconstrained boundary conditions. In the latter case, the problem is solved by minimising a certain performance index. Once the problem is stated, the gradient of the objective function, as well as the Jacobian of the constraints are computed and assembled in an automatic fashion.

Results are given for the dynamical substitutes of the collinear points of several three-body systems. Periodic and quasi-periodic orbits in the framework of the RTBP (e.g., halo orbits) are refined in the full gravitational solar system model by means of the proposed method.

The trajectory-refinement algorithm has been implemented with the idea of being versatile. With minor adjustments to the code backbone it can be applied to a large variety of practical astrodynamics problems, from stable orbits to optimised propelled trajectories and orbits that exploit the intrinsic dynamics of the solar system.

SOMMARIO

Il problema ristretto dei tre corpi (RTBP) è il modello ideale per calcolare soluzioni uniche, che vanno da orbite nell'intorno dei punti Lagrangiani ai trasferimenti a basso consumo energetico. Queste traiettorie incorporano l'effetto di due attrattori gravitazionali in modo naturale, e si prestano dunque ad uno studio più accurato rispetto alle coniche, soluzioni del classico problema di Keplero. Tuttavia, quando le orbite dei tre corpi sono riprodotte nel modello reale del sistema solare, si trovano grandi errori. In particolar modo, quando queste orbite sono definite nelle regioni dello spazio delle fasi in cui la sensibilità è elevata, le perturbazioni dovute ad altri corpi producono grandi effetti lungo le orbite.

Il fulcro di questo lavoro di tesi giace nello sviluppo di un algoritmo automatico per la correzione delle orbite al modello gravitazionale completo che descrive il sistema solare. Le equazioni differenziali che regolano la dinamica di una particella priva di massa sono scritte come perturbazione del RTBP in un sistema non uniformemente rotante e pulsante, utilizzando un formalismo Lagrangiano. La procedura di affinamento avviene mediante una tecnica di multiple shooting, e il problema è risolto per un insieme finito di variabili. La generalità dell'algoritmo consiste nella possibilità di gestire condizioni al contorno sia vincolate che non vincolate. In quest'ultimo caso, il problema è risolto tramite minimizzazione di un determinato indice. Formulato il problema, il gradiente della funzione obiettivo e il Jacobiano dei vincoli vengono calcolati e assemblati in modo automatico.

Vengono forniti i risultati per i sostituti dinamici dei punti collineari di diversi sistemi a tre corpi. Orbite periodiche e quasi-periodiche nel quadro del RTBP (ad esempio orbite halo) sono affinate nel modello completo a n corpi mediante il metodo proposto.

L'algoritmo di affinamento della traiettoria è stato implementato con l'idea di essere versatile. Con aggiustamenti minori al codice, esso può essere applicato ad una grande varietà di problemi pratici dell'Astrodinamica: da orbite stabili ad ottimizzazione di traiettorie propulse e orbite che sfruttano le dinamiche intrinseche del sistema solare.

*Do not go where the path may lead,
go instead where there is no path and leave a trail.*

— Ralph Waldo Emerson —

ACKNOWLEDGMENTS

I would like to thank professors Franco Bernelli Zazzera and Michèle Lavagna for their availability and readiness in answering my questions, both directly related to the thesis and concerning my future academic career. I withal appreciated the help of Dr. Luigi Mingotti.

I am grateful to my supervisor, Dr. Francesco Topputo, not only for his scientific support during the whole study period, but also for his human attitude towards me. He guided and followed me in this last part of my Master of Science.

Acknowledgements to my friends, which were there even if I was not. In particular to Marf, who taught me the intricacy of moralism and maybe brought me nearer to the engineering world; to Monai, fellow in misfortune; and to Vittorio Veneto's old dudes.

A special thank goes to 'polletti' Patrik, Sergio and Paolo, companions of adventure and shenanigans in 'Middle Earth', with whom I share the best, most hilarious and most difficult memories of my life.

Un immenso ringraziamento alla mia famiglia, mamma, papà, Mattia, Raffaele, Stefano, nonna Gianna e nonni paterni; che mi è stata vicino anche nella lontananza, e mi ha aiutato imperterrita in tutti questi anni.

此刻我很幸福，我要感谢与我一路同行的女友，因为你的陪伴让我得以专心学术，顺利完成此次毕业论文。

Diogene Alessandro Dei Tos

CONTENTS

1	INTRODUCTION	1
1.1	Historical legacy	1
1.2	Motivation and goals	3
1.3	State of the art	5
1.4	Organisation of the work	8
2	DYNAMICS MODELS	9
2.1	The problem of n bodies	9
2.2	The Kepler problem	12
2.2.1	Conservation of energy	13
2.2.2	Conservation of angular momentum	14
2.2.3	The trajectory	14
2.2.4	Kepler's laws	15
2.2.5	Orbit in three dimensions	16
2.3	The restricted three-body problem	19
2.3.1	Equations in the synodic frame	21
2.3.2	Lagrangian points	25
2.3.3	Motion near the equilibrium points	30
3	EQUATIONS OF MOTION IN THE ROTO-PULSATING FRAME	41
3.1	Change of coordinates and Lagrangian formulation	42
3.2	Coefficients for the equations of motion	52
3.3	Fourier analysis of the motion equations' coefficients	54
4	INTEGRATION AND VALIDATION	65
4.1	Integration scheme	65
4.1.1	Multi-step methods	67
4.1.2	Runge-Kutta methods	70
4.2	The JPL ephemeris model	71
4.2.1	Julian days count	75
4.3	Validation of the dynamical problem integration	78
4.3.1	Solar system barycentric integration	85
4.3.2	Roto-pulsating integration	88
4.3.3	Double-way validation	95
5	METHOD AND RESULTS	99
5.1	Two-point boundary value problem	99
5.1.1	The simple shooting technique	100
5.1.2	The multiple shooting method	103
5.2	The trajectory refinement algorithm	107
5.2.1	The modified multiple shooting	110
5.3	Dynamical substitutes of libration points	113

5.4	Quasi-periodic orbits refinement	119
5.4.1	The halo family	119
5.4.2	The planar Lyapunov family	121
6	FINAL REMARKS	125
6.1	Conclusions	125
6.2	Prospective work	126
A	ROTATION MATRICES PROPERITES	131
A.1	Properties of $\mathcal{C}^T \mathcal{C}$	131
A.2	Properties of $\mathcal{C}^T \dot{\mathcal{C}}$	132
B	FOURIER ANALYSIS	135
B.1	The Fourier integral: a continuous representation	135
B.2	The Fourier integral: a discrete representation	140
B.3	A refined Fourier analysis	144
BIBLIOGRAPHY		145

LIST OF FIGURES

- Figure 2.1 Geometry of the n-body problem in an inertial reference frame, XYZ 10
- Figure 2.2 Geometry of the two-body problem in an inertial reference frame, XYZ, and relative frame, xyz 12
- Figure 2.3 Elliptical orbit and its perifocal frame in the Kepler problem 15
- Figure 2.4 Geocentric equatorial and perifocal frame references with orbital parameters and Euler angles 17
- Figure 2.5 Sequence of three rotations transforming I, J, K into $\hat{e}, \hat{q}, \hat{h}$.
The ‘eye’ viewing down an axis sees the illustrated rotation about that axis. This image is courtesy of Curtis [11] 18
- Figure 2.6 Geometry of the three-body problem in an inertial reference frame, XYZ, centred at the primaries barycenter 20
- Figure 2.7 Synodic reference frame for the CRTBP 23
- Figure 2.8 Quintic polynomial for the evaluation of the collinear libration points, $f(x, 0, 0)$ 27
- Figure 2.9 Color-gradient visualisation of the potential function Ω , for $z = 0$ 28
- Figure 2.10 Contour map of $J = 2\Omega$, and zero-velocity curves for $\mu = 0.12$ at several interesting discrete values of the Jacobi constant, C 29
- Figure 2.11 Parameter c_2 36
- Figure 2.12 Planar Lyapunov orbits family for the Earth-Moon system around the first (left) and second (right) Lagrangian point 38
- Figure 2.13 Halo orbits family around the first collinear point L_1 of the Sun-Jupiter gravitational system 39
- Figure 3.1 Transformation geometry of the three-body problem in an inertial reference frame, XYZ 42
- Figure 3.2 Norm of Fourier transform of the motion equation ($b_i, i = 1, \dots, 6$) coefficients for the Earth-Moon case 56
- Figure 3.3 Norm of Fourier transform of the motion equation ($b_i, i = 7, \dots, 13$ excluding b_9) coefficients for the Earth-Moon case 56
- Figure 3.4 Norm of Fourier transform of the motion equation coefficients b_9 for the Earth-Moon case 57

Figure 3.5	Norm of Fourier transform of the motion equation ($b_i, i = 1, \dots, 6, 13$ excluding b_3) coefficients for the Sun-Earth case	58
Figure 3.6	Norm of Fourier transform of the motion equation ($b_i, i = 7, \dots, 12$) coefficients for the Sun-Earth case	58
Figure 3.7	Norm of Fourier transform of the motion equation coefficients b_3 for the Sun-Earth case	59
Figure 3.8	Norm of Fourier transform of the motion equation ($b_i, i = 1, \dots, 6$) coefficients for the Sun-Jupiter case	60
Figure 3.9	Norm of Fourier transform of the motion equation ($b_i, i = 7, \dots, 13$ excluding b_8) coefficients for the Sun-Jupiter case	60
Figure 3.10	Norm of Fourier transform of the motion equation coefficients b_8 for the Sun-Jupiter case	61
Figure 3.11	Norm of Fourier transform of the x components of the Sun (bottom) and Mercury (top). The positions are expressed in Kilometres and are written in the inertial frame of reference, centred at SSB	62
Figure 4.1	x-y projection of orbital trajectories of different small objects, centred at Earth	79
Figure 4.2	Trajectory of the Jupiter trojan Achilles, Sun-Jupiter rotopulsating frame	83
Figure 4.3	Error trend for Aten, class of the near-Earth asteroids Aten (Short period: 27 years). SSB integration.	85
Figure 4.4	Error trend for Quetzalcoatl, class of the Amor (Short period: 27 years). SSB integration.	86
Figure 4.5	Error trend for Juno, class of the Main-belt asteroids (Long period: 428 years). SSB integration.	86
Figure 4.6	x-y projection of orbital trajectories of different small objects in the Sun-Jupiter (top figures) and in the Sun-Earth synodic frame (bottom figures)	88
Figure 4.7	Error trend for Icarus, class of the Apollo. Sun-Jupiter synodic frame	89
Figure 4.8	Error trend for Aneas, class of the Jupiter trojan. Sun-Jupiter synodic frame	90
Figure 4.9	Error trend for Atira, class of the Atira. Sun-Earth synodic frame	91
Figure 4.10	Error trend for Brucia, class of the Mars-crossers. Sun-Earth synodic frame	92
Figure 4.11	Error trend for Hidalgo, class of the Centaurs. Sun-Earth synodic frame	92
Figure 4.12	Error trend for Deimos, natural satellite of Mars. Sun-Mars synodic frame	93

Figure 4.13	Double-way validation scheme	95
Figure 5.1	Example of a simple shooting	103
Figure 5.2	Multiple shooting strategy and defects vector	104
Figure 5.3	Solution of a Lambert problem trajectory with the multiple shooting method	106
Figure 5.4	Iterations of the multiple shooting method for the component x of the Lambert problem trajectory	107
Figure 5.5	Flux diagram of the iterative algorithm for orbits refinement	109
Figure 5.6	Coordinate projections of the dynamical substitutes of the L_1 (top), L_2 (middle) and L_3 (bottom) of the Sun-Jupiter system in the real ephemeris n-body dynamics (only the first 110 years of the computed orbits are displayed)	114
Figure 5.7	Coordinate projections of the dynamical substitutes of the L_1 (top), L_2 (middle) and L_3 (bottom) of the Earth-Moon system in the real ephemeris dynamics (1 year of computed orbits are displayed)	115
Figure 5.8	Coordinate projections of the dynamical substitutes of the L_1 (top), L_2 (middle) and L_3 (bottom) of the Sun-Earth system in the real ephemeris n-body dynamics (only the first 10 years of the computed orbits are displayed)	116
Figure 5.9	Fourier transform of the Sun-Earth L_3 dynamical substitute, x -component	117
Figure 5.10	Copernicus output text file for the computation of the Sun-Jupiter L_2 dynamical substitute	118
Figure 5.11	Coordinate projections of the refined Lissajous orbit of the Earth-Moon system L_3 in the real ephemeris n-body dynamics	119
Figure 5.12	Initial CRTBP guess (top) and refinement (bottom) of halo orbits with $A_z = 0.01$ (smallest orbit), $A_z = 0.03$, and $A_z = 0.06$ (largest orbit) of the Earth-Moon L_1 libration point. Only the first year is plotted here	119
Figure 5.13	Halo orbits ($A_z = 0.01$) and their numerical 50-year refinements around L_1 (top) and L_2 (bottom) of the Sun-Jupiter gravitational system. On the left hand side the orbits of the CRTBP taken as initial seeds are shown, and on the right hand side their refinements	120
Figure 5.14	Initial CRTBP guess (top) and refinement (bottom) of halo orbits with $A_z = 0.002$ (smallest orbit), and $A_z = 0.005$ (largest orbit) of the Sun-Earth L_2 collinear point. Only the first 11 years are plotted here	121

Figure 5.15	Fourier transform of the $A_z = 0.01$ halo orbit abut the L_2 of Sun-Earth gravitational system, x-component	122
Figure 5.16	Initial CRTBP guess (top) and 20-year numerical refinement (bottom) of planar Lyapunov orbits with $C_J = 3.039$ (smallest orbit), and $C_J = 3.02$ (largest orbit) of the Sun-Jupiter L_1 libration point	123
Figure 5.17	Initial CRTBP guess (top) and 1-year numerical refinement (bottom) of planar Lyapunov orbit characterised by Jacobi energy $C_J = 3.15$, of the Earth-Moon L_2 collinear point	123
Figure 5.18	Fourier transform of the z-component of the $C_J = 3.15$ planar Lyapunov orbit abut the L_2 of Earth-Moon system	124

LIST OF TABLES

Table 2.1	Main gravitational systems mass parameters and adimensional position of the collinear points	27
Table 3.1	Earth-Moon	57
Table 3.2	Sun-Earth	59
Table 3.3	Sun-Jupiter	61
Table 4.1	Adams-Basforth coefficients	69
Table 4.2	Adams-Moulton coefficients	70
Table 4.3	Butcher table	71
Table 4.4	Butcher table for a 4th order RK	71
Table 4.5	Recognised dwarf planets	78
Table 4.6	List of several natural satellites of planets, ordered by mass	80
Table 4.7	Asteroids	82
Table 4.8	Periods for the validation	82
Table 4.9	Maximum position and velocity error of the SSB integration for various asteroids classes. Short and medium periods	84
Table 4.10	Maximum position and velocity error of the SSB integration for various asteroids classes. Long period	87
Table 4.11	Maximum error of the roto-pulsating integration for various asteroids classes. Short period	90
Table 4.12	Maximum error for several selected natural satellites in their natural synodic frame	94

Table 4.13	Parameters of the double-way validation objects	96
Table 4.14	Errors of the double way validation study cases	97
Table 5.1	Shooting techniques results for a RTBP example	107
Table 5.2	Approximate order of magnitude [Km] of dynamical substitutes orbits	115
Table B.1	Some Fourier transform pairs	137
Table B.2	Main properties of the Fourier transform	139

1

INTRODUCTION

1.1 HISTORICAL LEGACY

Astronomy, etymologically ‘the law of the stars’, is the observation of celestial phenomena and the derivation of empirical laws from these observations. Astronomy is the oldest of physical science, our ancestors started to look at the sky thousands of years ago wondering what they were seeing and trying to fit it with laws of the world they were living in. Some heavenly phenomena were pretty well understood and correctly forecast among the Babylonian long before the Anno Domine, and philosophers in the ancient Greece had already speculated on common patterns in the celestial bodies motion. Their observations were so accurate that Aristarchos, as early as the second century BC, had the remarkable intuition of a Heliocentric system governing the Universe [30]. Several explanations were proposed in the course of the centuries, the Geocentric theory in the *Almagest* of Claudius Ptolemaus being probably the most renown and the one which dominated the astronomical panorama from around 200 AD until in 1543 Nicolaus Copernicus (1473-1543) published, the very same year he died, *De Revolutionibus orbium coelestium*. The Heliocentric model inspired a lot of scientists which aimed at demonstrating the veracity of this brand new theory. From extended and patient observations made by Tycho Brahe (1546-1601) and Galileo Galilei (1564-1642), it turned out predictions made with the Copernican model far walloped predictions made with the older Ptolemaic model in terms of accuracy and simplicity (Pannekoek [34]). With Sir Isaac Newton (1642-1727) the mightiest breakthrough of Modern Astronomy knew its acme: the universal theory of gravitation formulated by the well-known English scientist in its *Philosophiae Naturalis Principia Matematica* finally gave a solid mathematical foundation to Astronomy, relating the motion of planets in terms of geometrical arguments. This gravitational model gave evidence to the three laws of planetary motion Johannes Kepler (1571-1630) had been formulating after Copernicus death.

Although Newton had invented his version of the differential calculus, the method of fluxions, the more compact methods of Gottfried Leibniz (1646-1716) rapidly became the preferred mathematical tool for addressing dynamical problems. The application of the differential calculus to the motions of

astronomical bodies culminated in Pierre-Simon Laplace's (1749-1827) great five volume work, *Mécanique Céleste*, published between 1799 and 1825.

After Celestial Mechanics and the Theory of Gravity had been successfully unified, the attention of the scientific community was partly drawn to the study of the motion of an artificial body put within the gravitational web formed by the celestial bodies, the branch of science known as Astrodynamics. The dynamical model used by both Kepler and Newton in their researches accounts for only one attractor at a time, consequently named *two-body problem* or more commonly *Kepler problem*. It is a sore approximation that requires the artificial satellite to 'feel' only the gravitational presence of a main massive body, nonetheless it's been used reliably since the 17th century and it's still being used nowadays for preliminary design in space missions. Thanks to its simple mathematical formulation it's surprisingly the only dynamical model whose solution has been found and proved in a closed way. A more accurate dynamical model is the *restricted three-body problem*, often addressed as RTBP in this work, that deals with two main attractors and a non-massive artificial object. The first contribution to this approximation was made by Leonhard Euler (1707-1783) in 1722 as aid to his lunar theories, and later by Giuseppe Lodovico Lagrangia¹(1736-1813), thanks to his profound knowledge in Analytical Mechanics. Although a great deal of effort has been put into this dynamical model, no closed-form solution has been found yet. Euler had the brilliant idea of using a rotating reference frame instead of an inertial one, simplifying considerably the equations of motion; Lagrangia discovered 5 equilibrium points²; Jacobi found out an integral of motion named after him; and Hill delineated the region of coherent motion. The extraordinary piece of work *Le Méthodes Nouvelles de la Mécanique Céleste* by Poincaré (1854-1912) established the fundamentals of the *Dynamical System Theory*, which he used later as tool to analyse qualitatively the dynamic of the RTBP.

Further profound impacts on science were two theories proposed by Albert Einstein (1879-1955). He realised that all motion was relative and that the speed of light was a constant, being the same speed no matter how fast an observer is moving, which violated the Newtonian laws of motions but was later demonstrated experimentally. Using the Lorentz transformation he made the requirements that all defined laws must work with respect to all bodies of reference and that the speed of light with respect to all bodies was the same. With these formulas, he discovered that time and mass cannot be constant for the speed of light to be constant; thus, time can not be separated from space so the two must exist together in a four dimensional space-time continuum. In 1905, Einstein published his findings in his Special Theory of Relativity, only valid in the absence of gravitational fields. With the *General Theory of Relativity* (1916),

¹ An Italian scientist born in Turin, commonly known with his French appellative Lagrange.

² These special points within the RTBP are often termed Lagrangian points (after the scientist), libration points, fixed or stationary points, or simply equilibrium points.

his results were applied to the gravitational theory as well, basically saying that all matter curves space; and in turn, how space is curved affects the movement of matter, which explains gravitational fields. This theory is constantly being validated by modern scientific experiments. Historically, scientists started to doubt the Newtonian gravitational theory because of the observed anomaly in Mercury perihelion motion, rigorously explained within the framework of the General relativity theory in Earman et al. [13].

1.2 MOTIVATION AND GOALS

In Astrodynamics the n -body problem is among the most general models to describe the motion of a mass particle subjected to the gravitational field of other $n - 1$ celestial bodies. Trajectories within the solar system are well described in the framework of the n -body dynamics, governed by the renowned Newtonian Universal Law of Gravitation. In order to develop high-fidelity models, perturbations shall be accounted for: solar radiation pressure, oblateness of massive objects, energy dissipation (due to atmospheric drag or magnetic fields) and relativistic effects. A qualitative portrait of the real free dynamics in this model is rather complicated (even neglecting perturbations), and has been the object of thorough studies in the past decades, most of which have been carried out numerically and lack hence of the generality and insight typical of qualitative tools. The difficulty in understanding the global picture of the complete gravitational model is twofold. Firstly, the differential equations of motion posses no closed-form solution, except for rare simplified cases. Secondly, chaos stems from the strong non-linearity of the dynamics (see Devaney et al. [12] for formal introduction on chaotic dynamical systems). That is, an arbitrarily small perturbation on the initial condition can cause a large deviation from the expected solution. Sensitivity to the initial configurations is intensified also by phenomena like orbital resonance and bifurcation (Strogatz [41] and Meyer et al. [32]), thus impeding to tackle the problem in a traditional way.

In the initial stages of Space mission design, simplified models are traditionally used to assess feasibility, estimate costs and produce a first-approximation spacecraft trajectory.

The Kepler problem, being the simplest model available, has been extensively used in the past. Interplanetary trajectories are designed patching together keplerian arcs, characterised by a different primary body; and gravity assist is the sole way, apart from propulsion and perturbative actions, the orbit can change its energy. It is a well-established technique that gives reliable results when applied to region of the phase space where the attraction of one body clearly prevails over the others. Accordingly, the concept of *sphere of influence* has been created. Nonetheless, trajectories designed in this model might

be far from an optimum condition and do not fully exploit the potential of the gravitational dynamics.

Lately, a much deeper insight on the restricted three-body problem has been achieved. When considering three bodies, the spacecraft can exploit the natural dynamics of the gravitational vector field in a more convenient fashion, producing great advantages. Not only orbits closer to an optimum condition are achieved, for instance that minimise fuel consumption; new kinds of solutions also emerge as part of the more realistic gravitational model. Quasi-stable motion around libration points is an example, i. e. Halo and Lissajous orbits. Invariant manifolds, ballistic capture and weak stability boundaries techniques make low-energy transfer available within the framework of the RTBP. If, on the one hand, this model is much more accurate than the classic two-body problem, on the other hand, it still embeds some forms of approximation, which cause the orbits to deviate from those arising in the real solar system dynamics.

The aim of this thesis is to develop a numerical procedure that automatically refines trajectories designed in simplified models, such as two- and three-body problems, in the complete solar system panorama. In this regard several questions arise. Will the trajectory refined in the real ephemeris model still possess the same unique and desirable features it did when designed in a simpler framework? Furthermore, it is reasonable to presume the real vector field could force the trajectory to deviate from its original shape, producing in the worst-case scenario diverging orbits. If the refined trajectory differs significantly from the designed one, what are the most sensible parameters that can be modified in order to adjust the trajectory towards a desirable path? Due to this sensitivity of phase space, the numerical refinement might need a lot of iterations to disclose the problem and converge towards the real solution, yet provided it will. Planar and vertical Lyapunov orbits, Lissajous and Halo orbits of several three-body systems will be the targets for the refinement procedure.

It is well known that the RTBP flow possesses 5 equilibrium points where velocity and acceleration are by definition null. Fixed points exist because the vector field governing the restricted three-body problem (written in a co-rotating frame with the primaries) vanish. In finer models, where the equations depend both on the state and on time (usually the dependance implicitly contained in the potential function), the existence of these special points is not guaranteed. Since the gravitational flow varies with time, fixed points are assumed to vary with time as well, producing trajectories that can be interpreted as dynamically substitutes of the Lagrangian points. Using progressive more difficult gravitational models, starting from the RTBP and increasing the number of fundamental frequencies retained, in Gómez et al. [20] it is demonstrated that dynamical substitutes of the collinear points under very general non-resonance conditions between the natural modes around the equilibrium points and the perturbing frequencies are quasi-periodic solutions. The frequencies of the solution will be the perturbing frequencies of the RTBP at hand. Dynamical substitutes of

triangular points are regarded as unattractive because of their stability property. The refinement algorithm will be applied, with proper adaptation, to the problem of finding the dynamical substitutes of the collinear points of several three-body systems.

At last, interplanetary transfers can be the objects of the refinement procedure. Techniques such as weak stability boundary, ballistic capture and escape and invariant manifolds exploit in a natural way the attraction of several celestial bodies. In general, the solution to these problems requires determination of a set of points in phase space that support transitory behaviour and hence where the gravitational attraction of more massive bodies tend to balance. In literature there exist a vast number of references that provide optimised interplanetary trajectories for a quite wide range of selections.

The refinement will be done in a high-fidelity framework where the three-dimensional, restricted n -body problem is modelled with accurate planetary ephemeris, which is representative of the real dynamics of a spacecraft in the solar system.

The motivation underlying this thesis is dual. Firstly, it stems from a profound personal interest in the global picture of Celestial Mechanics within the solar system. Although the algorithm of trajectory refinement makes extensive use of brute computational force to disclose the general gravitational problem, it is a necessary step among the breakdown charts of a Space mission design. In addition, the drawbacks of using brute force are somehow mitigated, considering that input trajectories are already solutions, even if in approximated models. The solution to the major resources problems the Earth is facing might be the Space, along with the incredibly challenges it poses. An automatic algorithm to refine space trajectories in the real ephemeris dynamics allows both more reliable costs and risk analysis, and long-term precise estimations and forecasts. In a world where cost, time, and reliability are leading features of space mission design, I believe this tool is of great importance.

Future applications include set of permanent observatories of the Sun, the magnetosphere of the earth, links with the hidden part of the Moon. A wide range of missions can be refined to the real solar system dynamics, ranging from payload transfers and rendezvous manoeuvres to interplanetary propelled trajectories. In this perspective, *colonisation of Space* is a little step closer to reality, as highlighted by Prof. Franco Bernelli Zazzera in an online interview.

1.3 STATE OF THE ART

In this section the author wishes not to give a thorough presentation of all the literature works concerning Astrodynamics, it alone would require a whole book. The goal is to provide the reader with the main authors and works that are closely related with the topics of this thesis, that is trajectory refinement

in the real ephemeris model. However, some papers will be mentioned, dealing with trajectories calculation and optimisation in simplified models. This is because the author deems these works as essential to comprehend the global picture of Celestial Mechanics and because one cannot disregard solutions in those models, anyhow the only able, at present, to give a qualitative insight to the dynamics. In fact, solely relying on numerical techniques and results might be dangerous, in the sense that incongruences may arise which are difficult to ‘catch’ and usually do not concern the dynamics, rather they are due to round-off errors or internal machine mistaken procedures.

The secrets of the Kepler problem have been unveiled since long. Swing-bies are primarily designed in the framework of the two-body problem and then tested in the real solar system model. The Rosetta mission, for example, exploited a swing-by of Earth increasing its energy content in order to reach its final target, comet 67P/Churyumov-Gerasimenko (estimated rendezvous time: August 2014). This mission and others serve as benchmark for missions designed with more refined models. The simple Kepler model is often used in parallel with an electrical propulsive strategy, by which the spacecraft slowly escape the gravitational attraction of the primary through a long spiralling ascent. Dawn (NASA) and Artemis (ESA) missions made use of ion thrusters and definitely prove the reliability and break-through in the field of electrical propulsion applied to space flight. In Petropoulos and Sims [35] a review of some special exact solutions of a thrusting spacecraft in planar motion are presented. In the more general three-dimensional case, shape-based approaches are preferred. Izzo [26] and Wall and Conway [50] solve a rendezvous Lambert problem by means of an exponential sinusoids function. It is rather impressive such a simplified model provides meaningful results, not to mention that it’s still used in preliminary mission design and in international competition. To mention one, the Global Trajectory Optimisation Competition ([1]), now at its 7th edition, makes use of the two-body problem hypothesis to design trajectories aimed at minimising some performance index and characterised by high innovative content.

There are several works in literature concerning the dynamics and the phase portrait of the RTBP. The concept of weak stability boundaries (WSB) was first heuristically introduced by Belbruno in 1987 for designing fuel-efficient space missions and was subsequently proven to be useful in related applications ([4], [5]). The first application for an operational spacecraft occurred in 1991 with the rescue of the Japanese mission Hiten, which made use of a weak capture trajectory. The WSB was also applied in the European Space Agency spacecraft SMART-1 in 2004. Ballistic capture will be used to inject BepiColombo (ESA mission scheduled for 2015) into a Mercury polar orbit. Ballistic capture techniques have been studied within the elliptical restricted three-body model in Hyeraci and Topputo [25], paving the way to further and deeper studies.

Exploiting the saddle part of the linearised RTBP vector field leads to low-energy transfers that follow special pathways in space, sometimes referred to as the Interplanetary Transport Network. Conley [9], in a paper dating back to 1968, first explained the huge potential of low-energy orbits in the neighbourhood of the RTBP fixed points and the way a spacecraft could gain advantage by exploiting them. The unstable manifolds provide indeed the means to achieve free-transport conditions, as it was subsequently demonstrated and experimentally proved. The mission Genesis (NASA) exploited the dynamics in the neighbourhood of libration points to efficiently collect scientific data. The ‘Barcelona Group’ has made tremendous advancements regarding the mathematical formulation of invariant objects in the RTBP model (Jorba and Masdemont [28], Gómez and Mondelo [23], Gómez et al. [19]), developing techniques to calculate quasi-stable orbits and invariant manifolds. In Gómez et al. [17] they also show efficient methods to continue these objects to the real ephemeris model.

The dynamical panorama of the complete solar system model has been analysed in Tang et al. [45] and Lian et al. [29], as far as the Earth-Moon system is concerned. In these references an algorithm to calculate dynamical substitutes is presented. Such method will have similar traits to the one this thesis is intended to develop. Dynamical substitutes of the collinear points of several three-body points are calculated in Gómez et al. [21], exploiting simplified solar system models. The phase portrait around the collinear points of the Earth-Moon system has been extensively studied in Hou and Liu [24], with an analytical approach based on Fourier expansion of the coefficients of motion.

Finally several trajectories in the framework of the RTBP have been studied, highlighting the huge improvement regarding fuel expenditure with respect to classic two-impulse Hohmann transfers. In Belbruno and Miller [6] a Sun-perturbed Earth to Moon transfer with ballistic capture is explained. In Topputo [47] a two-impulse transfer is applied in the framework of the restricted four-body problem. A study of the transfer from the Earth to a halo orbit around the equilibrium point L_1 is analysed in Gómez et al. [17].

Lastly, Astrodynamics problems have sometimes been tackled via a statistic approach. This is not surprising, considering that the gravitational flow exhibits highly non-linear behaviour and hence chaos stems from the motion. This offers a possible alternate approach to studying special kinds of motion, one of which is dealing with chaotic system in a stochastic fashion. Belbruno [2] shows the stochastic approach applied to the RTBP, whereas in Varvoglis [49] the chaotic motion of bodies in the asteroid belt is studied under the perspective of the interactions and cataclysmic collisions that contributed to form the solar system the way we know it now.

1.4 ORGANISATION OF THE WORK

The work presented in this thesis is organised as follows:

DYNAMICAL MODELS The main dynamical models used throughout this work are shown in chapter 2. A comprehensive introduction of the general n -body problem is given. The Kepler problem is briefly addressed and its main features are shown. A deeper concern is put in the study of the restricted three-body problem. The synodic reference, as introduced by Euler, is explained highlighting the main advantages and the results concerning the Jacobi integral of motion. The phase space portrait in the neighbourhood of the libration points is analysed, explaining stability and existence of special periodic orbits around the fixed points of the RTBP flow.

PERTURBED n -BODY PROBLEM EQUATIONS In chapter 3 the differential equation of motion are written as perturbation of the RTBP. The equations correspond to the restricted motion of a particle within the n -body flow. The Lagrangian formalism is exploited and an ocultate adimensionalisation is performed, resulting in the thorough definition of the coefficients for the equations. These are then analysed by means of a Fourier expansion, and some qualitative information are deduced.

INTEGRATION AND VALIDATION Chapter 4 treats the numerical scheme adopted to integrate the differential equations of motion, once proper initial conditions are provided. Thanks to a high-order Bashforth-Moulton method, known objects are propagated forward and benchmarked against the database of small celestial objects implemented and updated by the Caltech Group at JPL. Several objects and three-body systems are considered.

RESULTS The results of the research are shown in chapter 5. First, two-point boundary value problems are tackled from an analytical perspective. Shooting techniques, simple and multiple, follow as tools able to integrate the TPBVP. Results concerning the dynamical substitutes of Sun-Jupiter, Sun-Earth and Earth-Moon are presented. Continuation of Halo and Lissajous orbits are shown in the Sun-Mars and Earth-Moon systems.

CONCLUSIONS Final remarks and observations on obtained results are discussed in this chapter. The implemented methodologies are objectively discussed and prospective work is suggested.

2

DYNAMICS MODELS

This chapter intends to give a brief introduction to the gravitational models used in Celestial Mechanics, the branch which studies the motion of celestial bodies, and Astrodynamics, concerned with the motion of artificial bodies within the same system. To this aim some common classifications of the dynamical models are discussed with respect to specific discriminants, such as the mass of the observed body, the motion of the celestial bodies and time.

First of all, gravitational problems are known as *general*, if the motion of the satellite influences the motion of the celestial bodies, or as *restricted* if it does not. Then, dynamical models can be classified as *coherent*, if the motion of the primaries is mutually influenced by their gravitational forces, or *noncoherent* if their motion arises from approximated and given functions of time, *a priori* assigned. Finally, the differential system describing the gravitation field of the problem can be defined as *autonomous*, if it does not depend explicitly on the time variable, or *nonautonomous*, if time appears explicitly in the dynamical equations.

2.1 THE PROBLEM OF n BODIES

From the stand-point of Astrodynamics the most general model for the description of the motion of a mass particle subjected to the gravitational field of other $n - 1$ celestial bodies is the n -body problem, whose geometry is shown in Figure 2.1. The dynamics of the mass particles $m_k, k = 1, \dots, n$, whose cartesian coordinates are $\mathbf{R}_k = (X_k, Y_k, Z_k)^T \in \mathbb{R}^3$ is governed by Newton's universal inverse law of gravitation:

$$\mathbf{F}_{jk} = \sum_{\substack{j=1 \\ j \neq k}}^{j=n} G m_j m_k \frac{\mathbf{R}_j - \mathbf{R}_k}{\|\mathbf{R}_j - \mathbf{R}_k\|^3} \quad \forall k = 1, \dots, n \quad (2.1)$$

where the resultant force \mathbf{F}_{jk} is the force exerted on the k -th body by the j -th body, directed as the vector joining them and pointing towards the j -th body; the quantity at denominator is the euclidean distance between k and j , hereafter denoted as R_{jk} and G is the universal gravitational constant. Applying

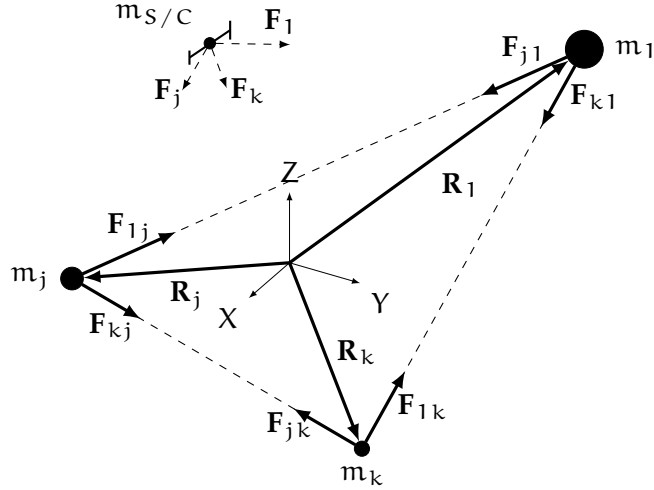


Figure 2.1: Geometry of the n -body problem in an inertial reference frame, XYZ

Newton's second law of motion and assuming constant masses, both for the celestial bodies and for the artificial satellite whose dynamics we're interested in, the equation may be written as:

$$m_k \ddot{\mathbf{R}}_k = \sum_{\substack{j=1 \\ j \neq k}}^{j=n} \frac{G m_j m_k}{R_{jk}^3} (\mathbf{R}_j - \mathbf{R}_k) \quad \forall k = 1, \dots, n \quad (2.2)$$

Equation (2.2) is written in an inertial reference frame and represents a set of $3n$ ordinary second order differential equations, or equivalently a set of $6n$ ordinary first order differential equations. They state the k -th mass particle moves under the influence of all the other $n - 1$ celestial bodies.

The gravitational force is a conservative force and as such it admits a potential. The potential energy for the gravitational force reads:

$$U = \sum_{\substack{j=1 \\ j \neq k}}^{j=n} \frac{G m_j m_k}{R_{jk}} \quad (2.3)$$

U is a function of the $3n$ variables \mathbf{R}_k . Provided $R_{jk} > 0$, it has been demonstrated that U is a smooth and well-defined function of its $3n$ variables, where smooth means continuous along with each order of partial derivative and real analytic. In the case at hand, since R_{jk} comes from a vectorial norm, it might be either positive or null, null being the case of collision between the j -th and k -th bodies. For the sake of simplicity it is assumed that no collisions occur¹.

¹ Note that a collision can be considered formally by means of a proper reduction, far beyond the scope of this analysis.

If $\nabla_k = (\partial/\partial x_k, \partial/\partial y_k, \partial/\partial z_k)^T$ is the gradient operator with respect to \mathbf{R}_k , the set of differential equations governing the motion of n mass particles moving in a cartesian three-dimensional space (XYZ) under their mutual gravitational influence might be written as:

$$m_k \ddot{\mathbf{R}}_k = \nabla_k U \quad \forall k = 1, \dots, n \quad (2.4)$$

The n celestial bodies have been considered point masses so far, that is their real shape is neglected. Their total mass is concentrated at the barycenter and the gravitational forces, exerted and felt, act on the same point. This assumption corresponds to a perfect spherical celestial body with symmetric internal mass distribution. It can be demonstrated ([48]) that the gravitational potential of a sphere with symmetric mass distribution coincides with the potential of a point placed at the sphere barycenter whose mass is the total sphere mass. The asphericity, or oblateness, of a celestial body can give rise to incongruence from the expected orbit, and is regarded as a perturbation in classic Astrodynamics.

In order to cast the initial value problem in a more compact state-space form, position and velocity vectors are grouped into $\mathbf{x} = (\mathbf{R}_1, \mathbf{R}_k, \dots, \mathbf{R}_n, \dot{\mathbf{R}}_1, \dot{\mathbf{R}}_k, \dots, \dot{\mathbf{R}}_n)^T \in \mathbb{R}^{6n}$,

$$\dot{\mathbf{x}} = \mathbf{f}(\mathbf{x}) \quad (2.5)$$

where $\mathbf{f} = (V_1, V_k, \dots, V_n, \nabla_1 U/m_1, \nabla_k U/m_k, \dots, \nabla_n U/m_n)^T$. Note that the vector field \mathbf{f} does not directly depends on the epoch, that is the gravitational dynamics cast onto an inertial frame of reference leads to an autonomous dynamical problem. Following Belbruno [3], Picard-Lindelöf theorem guarantees the existence and uniqueness of the Cauchy problem, provided that \mathbf{f} is Lipschitz in the continuous sense. Thanks to the smoothness property of the potential energy the sufficient condition is satisfied and the initial value problem admits a unique solution once a set of proper $6n$ initial conditions are provided.

Eqs. (2.4) possess a set of ten algebraic independent integrals, expressed by the common conservation law of linear momentum (6 constants), angular momentum (3 constants) and energy (1 constant). The first implies that the barycenter moves in an inertial fashion and therefore the dynamics can be written without loss of generality with respect to the barycenter of the n bodies; from now on, unless specified, the cartesian reference frame will be centred at the barycenter. The second somehow forces the way the bodies have to rotate about the barycenter and the last invariant of motion forces the dynamics at a precise energy level.

The system of equations (2.4) represents the complete dynamical description of the n -body problem, where all the position vectors of the celestial bodies are unknown and the acceleration of each mass particle depends on all the

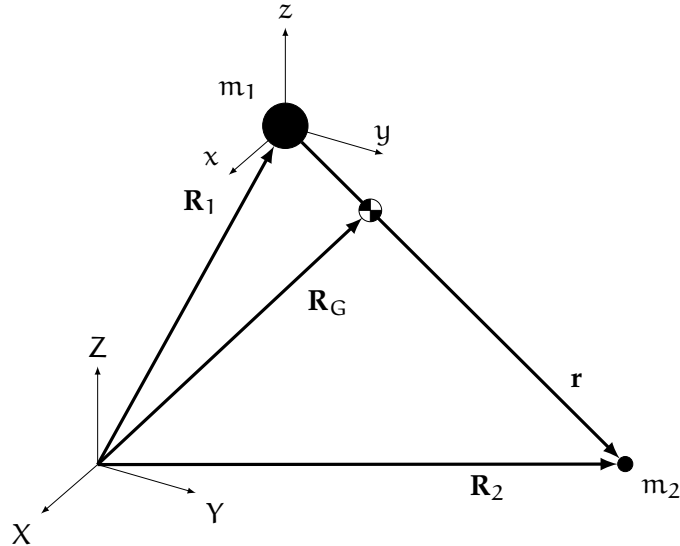


Figure 2.2: Geometry of the two-body problem in an inertial reference frame, XYZ , and relative frame, xyz

remaining ones. This is the general n -body problem. However, Astrodynamics is mainly concerned with the study of an artificial object, in this context the hypothesis of restricted dynamics has been applied with accurate results. The artificial object moves in the vectorial field created by the n celestial bodies, or alternatively it does not affect the motion of the n main bodies. It's quite clear that the mass of the artificial object under study has to be significantly less than the other objects' masses for this assumption to be valid. Another significant simplification can be obtained if the trajectories of the primaries are proper time-dependent functions, obtaining thus an incoherent model. Let S be the set of celestial bodies, the motion of an artificial satellite is represented by a system of three second order differential equations.

$$\ddot{\mathbf{R}} = \sum_{j \in S} \mu_j \frac{\mathbf{R}_j - \mathbf{R}}{\|\mathbf{R}_j - \mathbf{R}\|^3} \quad (2.6)$$

where $\mu_j = Gm_j$ is the mass parameter in $[Km^3/s^2]$ and $\mathbf{R} = (X, Y, Z)^T$ is the position of the artificial satellite.

2.2 THE KEPLER PROBLEM

In this section the classical problem of determining the motion of two bodies due solely to their own mutual attraction is briefly addressed, with the purpose of recalling the fundamental principles and invariants of motion of the simplest model available for preliminary design and observations. The equations describing the dynamics of the particle masses m_1 and m_2 read:

$$\ddot{\mathbf{R}}_1 = Gm_2 \frac{\mathbf{r}}{r^3} \quad (2.7)$$

$$\ddot{\mathbf{R}}_2 = -Gm_1 \frac{\mathbf{r}}{r^3} \quad (2.8)$$

where \mathbf{R}_1 and \mathbf{R}_2 are the position vectors of the corresponding particle, and $\mathbf{r} = \mathbf{R}_2 - \mathbf{R}_1$ is the relative position of m_2 with respect to m_1 as seen in Figure 2.2. Subtracting the first from the second equation the relative dynamics is obtained:

$$\ddot{\mathbf{r}} = -\mu_{2b} \frac{\mathbf{r}}{r^3} \quad (2.9)$$

where $\mu_{2b} = G(m_1 + m_2)$. The second order differential equation describing the relative motion of m_2 about m_1 , and consequently vice versa, has a closed-form solution. It's interesting to note that this does not mean that the complete two-body problem has been solved because inertial information of one of the mass particle is yet to be found. A common approximation is to neglect m_2 , being much smaller than m_1 , hence the motion of the mass particle m_1 is not influenced by any force and a reference frame centered in it can be but an inertial one. Equation (2.9) possesses integrals of motion that greatly simplify the mathematical treatment of the problem, treated hereafter. Detailed mathematical proofs of the following conservation laws and of the basic principles underlying the Kepler problem can be found at Curtis [11].

2.2.1 Conservation of energy

The law of energy conservation might be simply obtained multiplying the equation of relative motion by the velocity vector $\dot{\mathbf{r}}$.

$$\ddot{\mathbf{r}} \cdot \dot{\mathbf{r}} = \mu_{2b} \frac{\mathbf{r} \cdot \dot{\mathbf{r}}}{r^3} \quad (2.10)$$

After some mathematical manipulation:

$$\frac{d}{dt} \left(\frac{\|\dot{\mathbf{r}}\|^2}{2} - \frac{\mu_{2b}}{r} \right) = 0 \quad (2.11)$$

The quantity between brackets is constant along the orbit, and it is known once the initial conditions have been provided. It's the sum of a kinetic energy and what is the two-body problem potential energy per unit mass. The specific mechanical energy reads:

$$\mathcal{E} = \frac{\|\dot{\mathbf{r}}\|^2}{2} - \frac{\mu_{2b}}{r} \quad (2.12)$$

where the constant of integration has been set to zero, resulting in a infinite potential energy reference; $\lim_{r \rightarrow \infty} \mathcal{E}_p = 0$.

2.2.2 Conservation of angular momentum

The angular momentum is obtained by cross-multiplying the motion equation by \mathbf{r} .

$$\mathbf{r} \wedge \dot{\mathbf{r}} = -\mu_{2b} \frac{\mathbf{r} \wedge \mathbf{r}}{r^3} \quad (2.13)$$

If the specific angular momentum is defined as $\mathbf{h} = \mathbf{r} \wedge \mathbf{v}$, equation (2.13) implies:

$$\frac{d\mathbf{h}}{dt} = 0 \quad (2.14)$$

The main and probably most important consequence is that the orbits of both mass particles must lie on a plane perpendicular to the specific angular momentum direction.

2.2.3 The trajectory

The only possible paths available for the relative two-body motion pertains to the family of curves known as *conic sections*. This nomenclature derives from the geometrical idea of crosscutting a nappe² with a plane, the angle by which the plane cuts across the 2 facing cones determines the shape of the curve, e.g. an ellipse, a parabola or a hyperbola. Cross-multiplying the equation of motion with the specific angular momentum vector and manipulating the results yields:

$$\frac{d}{dt} \left(\frac{\dot{\mathbf{r}} \wedge \mathbf{h}}{\mu_{2b}} - \frac{\mathbf{r}}{r} \right) = \frac{d\mathbf{e}}{dt} = 0 \quad (2.15)$$

The adimensional integration constant of Equation (2.15) is the eccentricity vector \mathbf{e} , defining the apse line. Projecting this equation on \mathbf{h} it's easy to verify that the eccentricity vector lies on the plane of motion. To obtain a scalar equation a multiplication by \mathbf{r} is performed.

$$r = \frac{h^2}{\mu_{2b}} \frac{1}{1 + e \cos \theta} \quad (2.16)$$

² One of the two pieces of a double cone (i.e., two cones placed apex to apex).

where θ is the angle between the eccentricity vector \mathbf{e} and the particle mass position vector \mathbf{r} , such that $\mathbf{r} \cdot \mathbf{e} = r e \cos \theta$. θ is commonly known as *true anomaly*. In the reference frame adopted the main body lies at one of the conic section foci.

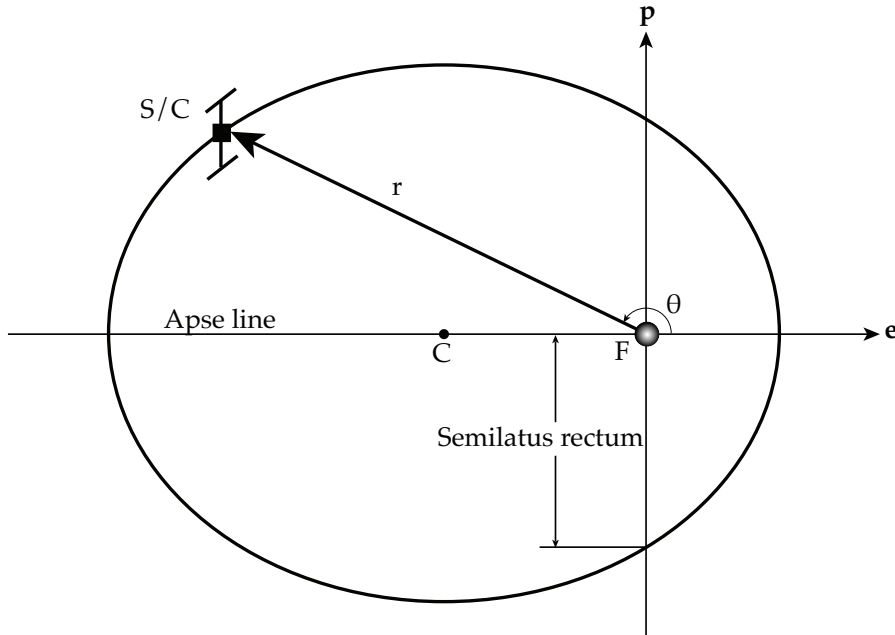


Figure 2.3: Elliptical orbit and its perifocal frame in the Kepler problem

2.2.4 Kepler's laws

From observations evidence and data-fitting Kepler was able to give a mathematical explanation of the planetary motion, without really requiring a model. The three laws are the outcome of his research and are merely a description, to which Newton gave at last a physical and mathematical proof. Kepler's three laws are stated here with a short demonstration.

1. *The orbit of each planet is an ellipse, with the Sun at a focus.*

The law explains itself considering the orbits the masses must follow are conic sections.

2. *The line joining the planet to the Sun sweeps out equal areas in equal times.*

The aerial velocity is a constant for the two-body problem,

$$\frac{dA}{dt} = \frac{h}{2} \quad (2.17)$$

3. *The square of the period of a planet is proportional to the cube of its mean distance from the Sun.*

The lapse of time required by the mass particle to complete a revolution around its focus is the orbital period T . Using the second law for the entire closed orbit and manipulating the results, the period formula reads:

$$\frac{T^2}{a^3} = \frac{4\pi^2}{\mu_2 b} = \text{const.} \quad (2.18)$$

2.2.5 Orbit in three dimensions

An important feature of the Kepler problem is the bidimensionality. To define an orbit in the plane requires two parameters: the eccentricity and the angular momentum. Other parameters can be obtained from these two. Furthermore, to locate a point on the orbit requires a third parameter, that is the true anomaly, which leads to the time since closest passage.

In this regard the *perifocal frame* is the most intuitive frame describing the problem. The tern unit vectors forming this frame are aligned with the eccentricity vector $\hat{\mathbf{e}}$ (x), the semilatus rectum $\hat{\mathbf{q}}$ (y) and the relative angular momentum $\hat{\mathbf{h}}$ (z)³. The semilatus rectum stems from orthogonality condition with respect to $\hat{\mathbf{e}}$ and $\hat{\mathbf{h}}$. Position and velocity vectors in the perifocal frame can be easily evaluated by inspection of figure 2.3 and differentiation:

$$\mathbf{r} = \frac{h^2}{\mu} \frac{1}{1 + e \cos \theta} (\cos \theta \hat{\mathbf{e}} + \sin \theta \hat{\mathbf{q}}) \quad (2.19)$$

$$\mathbf{v} = \frac{\mu}{h} [-\sin \theta \hat{\mathbf{e}} + (e + \cos \theta) \hat{\mathbf{q}}] \quad (2.20)$$

In order to describe the orbit in three dimensions, the orbital plane orientation must be determined with respect to some other reference plane. The geocentric equatorial plane at epoch January 1, 2000 represents the standard in this work. The orthogonal XYZ tern that defines the three-dimensional space is defined by the unit vectors \mathbf{I} , \mathbf{J} and \mathbf{K} . The X axis is aligned as the intersection line between the equator and the ecliptic, commonly known as vernal equinox line, γ . The Z axis is aligned with the North Pole direction. Finally the Y unit vector comes from the orthogonality between X and Z. Describing the orientation of an orbit in three dimensions requires three additional parameters, called the Euler angles, which are illustrated in Figure 2.4.

First, the intersection of the orbital plane with the equatorial plane is located. This line is called the *node line*. The point on the node line where the orbit passes above the equatorial plane from below it is called the *ascending node*. The node line vector \mathbf{N} extends outward from the origin through the ascending node. At the other end of the node line, where the orbit dives below the equatorial plane, is the descending node. The angle between the positive

³ Hats are used to indicate unit vectors.

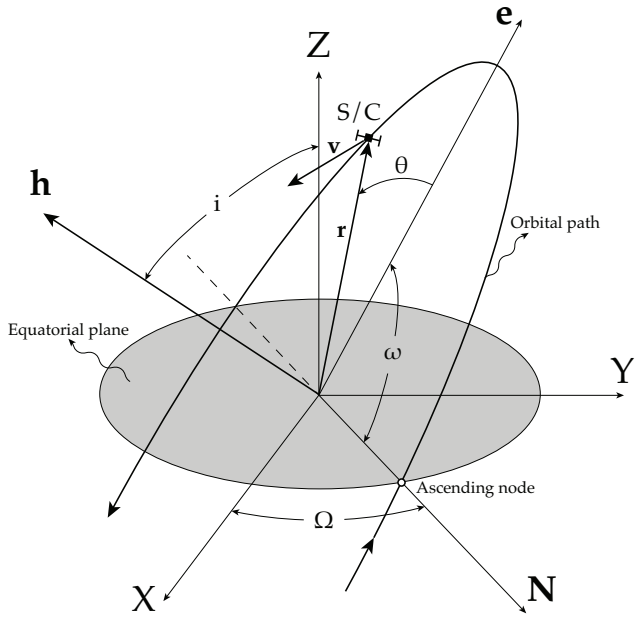


Figure 2.4: Geocentric equatorial and perifocal frame references with orbital parameters and Euler angles

X axis and the node line is the first Euler angle Ω , the *right ascension of the ascending node*.

The dihedral angle between the orbital plane and the equatorial plane is the *inclination* i , measured according to the right-hand rule, that is, counterclockwise around the node line vector from the equator to the orbit. The inclination is also the angle between the positive Z axis and the normal to the plane of the orbit, \mathbf{h} .

It remains to locate the point of closest passage of the orbit. The periapsis lies at the intersection of the eccentricity vector with the orbital path. The third Euler angle ω , the *argument of perigee*, is the angle between the node line vector and the eccentricity vector, measured in the plane of the orbit. In summary, the six orbital elements are:

- | | |
|---|---|
| 1. specific relative angular momentum, \mathbf{h}
2. inclination i
3. right ascension of the ascension node, Ω | 4. eccentricity, e
5. argument of perigee, ω
6. true anomaly, θ |
|---|---|

The transformation from geocentric equatorial to perifocal frame is accomplished by a sequence of simple Eulerian rotation about the main axis, illustrated in Figure 2.5. The first rotation, about the Z axis through Ω , transforms the X axis into the node line. The second rotation is about the node line through the inclination angle i . The new XY plane is then parallel to the orbital plane. The last rotation, around \hat{h} and through ω , rotates the X' axis so as it becomes coincident with the periapsis line. The transformation is hence complete and can be formulated analytically by means of the rotation matrices:

$$\mathcal{R}(\Omega) = \begin{bmatrix} \cos \Omega & \sin \Omega & 0 \\ -\sin \Omega & \cos \Omega & 0 \\ 0 & 0 & 1 \end{bmatrix} \quad \mathcal{R}(i) = \begin{bmatrix} 0 & 0 & 1 \\ \cos i & \sin i & 0 \\ -\sin i & \cos i & 0 \end{bmatrix}$$

$$\mathcal{R}(\omega) = \begin{bmatrix} \cos \omega & \sin \omega & 0 \\ -\sin \omega & \cos \omega & 0 \\ 0 & 0 & 1 \end{bmatrix}$$

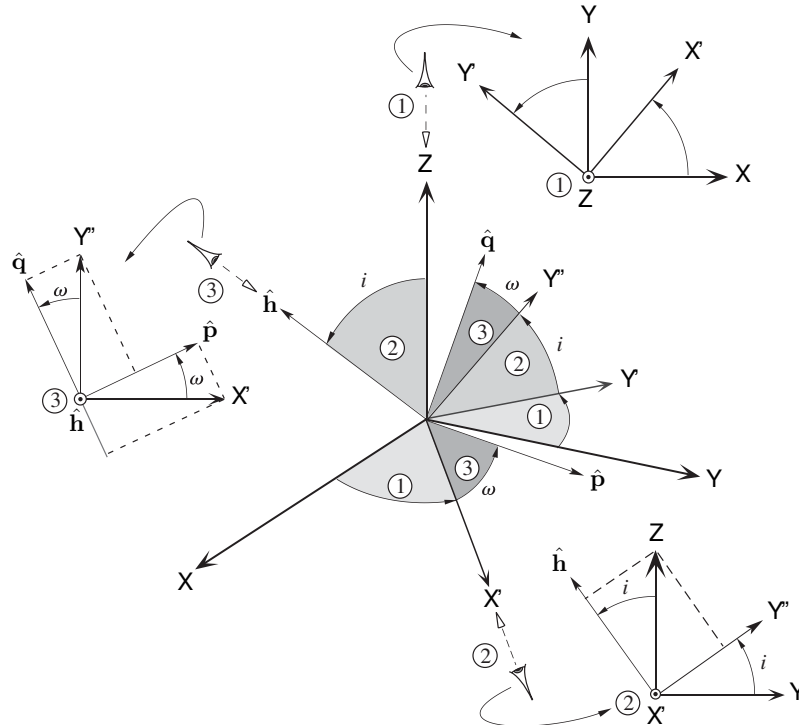


Figure 2.5: Sequence of three rotations transforming I, J, K into $\hat{e}, \hat{q}, \hat{h}$. The 'eye' viewing down an axis sees the illustrated rotation about that axis. This image is courtesy of Curtis [11]

The result of the rotations sequence is just the product of the transformation matrices for each rotation in the correct order:

$$\begin{aligned}\mathcal{R}_{\text{TOT}} &= \mathcal{R}(\omega)\mathcal{R}(i)\mathcal{R}(\Omega) \\ &= \begin{bmatrix} c_\Omega c_\omega - s_\Omega s_\omega c_i & s_\Omega c_\omega + c_\Omega s_\omega c_i & s_i s_\omega \\ -c_\Omega s_\omega - s_\Omega c_\omega c_i & -s_\Omega s_\omega + c_\Omega c_\omega c_i & s_i c_\omega \\ s_\Omega s_i & -c_\Omega s_i & c_i \end{bmatrix}\end{aligned}$$

where for notation simplicity c and s stand for cos and sin, respectively.

The transformation from perifocal to geocentric equatorial components is accomplished now thanks to the transpose of this matrix. Let \mathbf{y}_{eq} and \mathbf{y}_{per} be vectors expressed in the geocentric equatorial and perifocal frame, respectively. Then:

$$\mathbf{y}_{\text{eq}} = \mathcal{R}_{\text{TOT}}^T \mathbf{y}_{\text{per}} \quad (2.21)$$

where the orthogonality property for rotation matrices has been used.

2.3 THE RESTRICTED THREE-BODY PROBLEM

This section aims at giving the mathematical formulation and a physical explanation on the restricted three-body problem. This model is a better approximation of the real dynamics and plays, in this thesis, the role of simplified reference model. In the case of $n = 3$ the system of equations (2.2) may be written as:

$$\ddot{\mathbf{R}}_1 = Gm_2 \frac{\mathbf{R}_2 - \mathbf{R}_1}{\|\mathbf{R}_2 - \mathbf{R}_1\|^3} + Gm_3 \frac{\mathbf{R}_3 - \mathbf{R}_1}{\|\mathbf{R}_3 - \mathbf{R}_1\|^3} \quad (2.22a)$$

$$\ddot{\mathbf{R}}_2 = Gm_1 \frac{\mathbf{R}_1 - \mathbf{R}_2}{\|\mathbf{R}_1 - \mathbf{R}_2\|^3} + Gm_3 \frac{\mathbf{R}_3 - \mathbf{R}_2}{\|\mathbf{R}_3 - \mathbf{R}_2\|^3} \quad (2.22b)$$

$$\ddot{\mathbf{R}}_3 = Gm_1 \frac{\mathbf{R}_1 - \mathbf{R}_3}{\|\mathbf{R}_1 - \mathbf{R}_3\|^3} + Gm_2 \frac{\mathbf{R}_2 - \mathbf{R}_3}{\|\mathbf{R}_2 - \mathbf{R}_3\|^3} \quad (2.22c)$$

Equations (2.22) describe the general problem with a set of 18 first order differential equations.

The restricted hypothesis requires the mass of the third body to be much smaller than the masses of the primaries, $m_3 \ll (m_2 \leq m_1)$. This means the cluster formed by the primaries actually moves according to Kepler's laws and m_3 does not influence their motion. The main consequence is that the barycenter of the system coincides with the m_1, m_2 pair's and it moves obviously in an inertial fashion; it serves therefore for a very convenient reference frame centre. Hereafter the motion of the primaries will be treated as a known

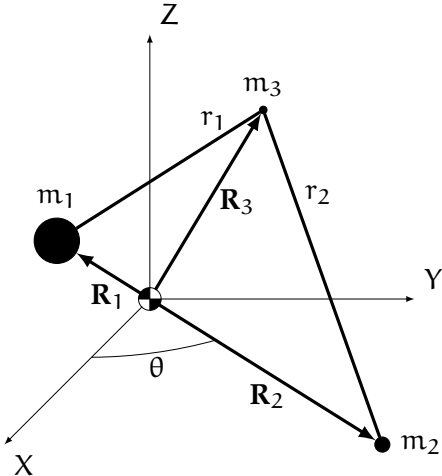


Figure 2.6: Geometry of the three-body problem in an inertial reference frame, XYZ , centred at the primaries barycenter

function of time, $\mathbf{R}_1 = \mathbf{R}_1(t)$ and $\mathbf{R}_2 = \mathbf{R}_2(t)$. This does not mean that the problem is incoherent, as is the case of the bicircular four-body problem. In fact, if the specified functions respect Newton gravitational equations (i. e., ephemeris data), then the problem is still coherent. The third mass particle moves in the gravitational vectorial field created by the primaries. Note that, if initially m_3 has no position and velocity components out of the primaries motion plane, it can but orbit in the same plane.

The dynamics for the third mass particle reads:

$$\ddot{\mathbf{R}} = Gm_1 \frac{\mathbf{R}_1 - \mathbf{R}}{\|\mathbf{R}_1 - \mathbf{R}\|^3} + Gm_2 \frac{\mathbf{R}_2 - \mathbf{R}}{\|\mathbf{R}_2 - \mathbf{R}\|^3} \quad (2.23)$$

where the subscript 3 referred to the third body has been dropped to simplify the notation.

Another approximation is introduced at this point to simplify the mathematical treatment of the dynamics: the primaries are revolving in circular orbits on the plane (X, Y) at constant angular speed, ω_2 . The resulting problem is called *circular restricted three-body problem* or CRTBP. Figure 2.6 delineates the geometry of the problem. Defining a and b the orbital radii of the primary and secondary body, respectively, and the angle between the X reference axis and the vector from the origin to the smaller primary m_2 as $\theta = \omega_2(t - t_0)$, the circular motion yields $\mathbf{R}_1 = -a(\cos \theta, \sin \theta, 0)^T$ and $\mathbf{R}_2 = b(\cos \theta, \sin \theta, 0)^T$. The explicit dynamics of $\mathbf{R} = (X, Y, Z)^T \in \mathbb{R}^3$:

$$\ddot{X} = -G \left(m_1 \frac{X + a \cos \theta}{r_1^3} + m_2 \frac{X - b \cos \theta}{r_2^3} \right) \quad (2.24a)$$

$$\ddot{Y} = -G \left(m_1 \frac{Y + a \sin \theta}{r_1^3} + m_2 \frac{Y - b \sin \theta}{r_2^3} \right) \quad (2.24b)$$

$$\ddot{Z} = -G \left(m_1 \frac{Z}{r_1^3} + m_2 \frac{Z}{r_2^3} \right) \quad (2.24c)$$

where

$$r_1 = \sqrt{(X + a \cos \theta)^2 + (Y + a \sin \theta)^2 + Z^2} \quad (2.25a)$$

$$r_2 = \sqrt{(X - b \cos \theta)^2 + (Y - b \sin \theta)^2 + Z^2} \quad (2.25b)$$

The dynamics written in the sidereal inertial frame gives birth to a nonautonomous set of differential equations whose closed-form solution has not been found yet.

2.3.1 Equations in the synodic frame

The differential system (2.24) describing the motion of a third particle subjected to the gravitational attraction of two primary bodies can be expressed in a more convenient way, which transforms the set of equations in an autonomous set. The basic idea is to find a reference frame that results in a time-independent force function. Euler first proposed the synodic frame of reference, this reference is again centered at the primaries' barycenter but it is rotating so as to maintain the primary bodies at a fixed position in space. For the assumptions made so far the synodic frame rotates at the very same primaries angular speed, ω_2 . If the axis are the ones shown in Figure 2.7 the transformation matrix may be straightforwardly written as:

$$\mathcal{T} = \begin{bmatrix} \cos \theta & -\sin \theta & 0 \\ \sin \theta & \cos \theta & 0 \\ 0 & 0 & 1 \end{bmatrix} \quad (2.26)$$

Let the third body position vector with respect to the synodic frame be $\hat{\rho}$, the rotation simply yields $\mathbf{R} = \mathcal{T}\hat{\rho}$. It's easy to see that $\hat{\rho}_1 = (-a, 0, 0)^T$, $\hat{\rho}_2 = (b, 0, 0)^T$ and $\hat{\rho} = (\hat{x}, \hat{y}, \hat{z})^T$. By a simple inspection of the geometry and considering barycentric properties, the positions of the primaries might be expressed as function of the masses and the distance between them.

$$a = \frac{m_2}{M} l \quad b = \frac{m_1}{M} l \quad (2.27)$$

where M is the sum of their masses, $M = m_1 + m_2$, and l is their mutual distance, $l = a + b$. From Equation (2.23) the dynamics in the synodic reference becomes:

$$\ddot{\rho} + 2\mathcal{T}^T \dot{\mathcal{T}}^T \dot{\rho} + \mathcal{T}^T \ddot{\mathcal{T}} \hat{\rho} = -G \left(m_1 \frac{\hat{\rho} - \hat{\rho}_1}{\|\hat{\rho} - \hat{\rho}_1\|^3} + m_2 \frac{\hat{\rho} - \hat{\rho}_2}{\|\hat{\rho} - \hat{\rho}_2\|^3} \right) \quad (2.28)$$

where the properties of a rotation cosine angle matrix have been used, namely the orthonormality and the invariance with respect to the vectorial norm. The derivative of the rotation matrix \mathcal{T} are:

$$\dot{\mathcal{T}} = \begin{bmatrix} -\omega_2 \sin \theta & -\omega_2 \cos \theta & 0 \\ \omega_2 \cos \theta & -\omega_2 \sin \theta & 0 \\ 0 & 0 & 0 \end{bmatrix} \quad \ddot{\mathcal{T}} = \begin{bmatrix} -\omega_2^2 \cos \theta & \omega_2^2 \sin \theta & 0 \\ -\omega_2^2 \sin \theta & -\omega_2^2 \cos \theta & 0 \\ 0 & 0 & 0 \end{bmatrix} \quad (2.29)$$

Developing the calculations equation (2.28) can be explicitly written per components:

$$\ddot{x} - 2\omega_2 \dot{y} = \omega_2^2 \hat{x} - G \left(m_1 \frac{\hat{x} + a}{\hat{\rho}_1^3} + m_2 \frac{\hat{x} - b}{\hat{\rho}_2^3} \right) \quad (2.30a)$$

$$\ddot{y} + 2\omega_2 \dot{x} = \omega_2^2 \hat{y} - G \hat{y} \left(\frac{m_1}{\hat{\rho}_1^3} + \frac{m_2}{\hat{\rho}_2^3} \right) \quad (2.30b)$$

$$\ddot{z} = -G \hat{z} \left(\frac{m_1}{\hat{\rho}_1^3} + \frac{m_2}{\hat{\rho}_2^3} \right) \quad (2.30c)$$

where $\hat{\rho}_1$ and $\hat{\rho}_2$ are the norm of the distances between the third mass and the primaries.

$$\hat{\rho}_1 = \sqrt{(\hat{x} + a)^2 + \hat{y}^2 + \hat{z}^2} \quad (2.31a)$$

$$\hat{\rho}_2 = \sqrt{(\hat{x} - b)^2 + \hat{y}^2 + \hat{z}^2} \quad (2.31b)$$

Note that the differential equations now do not depend directly on time and the set is hence autonomous. Furthermore, the physical parameters that govern equations (2.30) are not mutually independent. It is shown in Szebehely [44] that, by a proper adimensionalisation, the restricted problem depends on only one parameter. *The adimensionalisation is such that the distance between the primaries, the angular speed and the sum of their masses is set to a unity value.* The choice of the dimensionless quantities is:

$$\rho = \frac{\hat{\rho}}{a + b} \quad \tau = \omega_2 t \quad \mu = \frac{m_2}{m_1 + m_2} \quad (2.32)$$

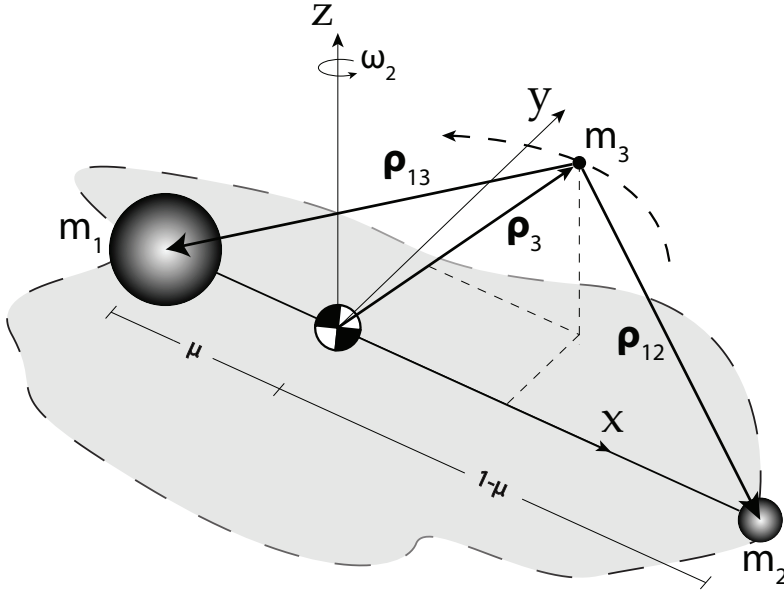


Figure 2.7: Synodic reference frame for the CRTBP

With this choice the positions of the primaries are simply $\rho_1 = (-\mu, 0, 0)^T$ and $\rho_2 = (1 - \mu, 0, 0)^T$ and the adimensional equations become:

$$\ddot{x} - 2\dot{y} = \Omega_{/x}^{(3b)} \quad (2.33a)$$

$$\ddot{y} + 2\dot{x} = \Omega_{/y}^{(3b)} \quad (2.33b)$$

$$\ddot{z} = \Omega_{/z}^{(3b)} \quad (2.33c)$$

where the three-body potential function can be expressed as:

$$\Omega^{(3b)} = \frac{1}{2}(x^2 + y^2) + \frac{1-\mu}{\rho_1} + \frac{\mu}{\rho_2} + \frac{1}{2}\mu(1-\mu) \quad (2.34)$$

The constant term has been added to provide a minimum value to the potential function, independently of the value μ . Terms ρ_1 and ρ_2 are the scalar distances between the third mass and the primaries.

$$\rho_1 = \sqrt{(x + \mu)^2 + y^2 + z^2} \quad (2.35a)$$

$$\rho_2 = \sqrt{(x - 1 + \mu)^2 + y^2 + z^2} \quad (2.35b)$$

The dimensionless equations (2.33) depend clearly only on the mass parameter, μ .

The CRTBP written in this form possesses a first integral of motion, called *Jacobi integral* and named after its discoverer, Jacobi (1836). It can be easily

obtained by manipulating the equations of motion. After multiplying each component by the corresponding velocity and summing:

$$\ddot{x}\dot{x} - 2\dot{y}\dot{x} + \dot{y}\dot{y} + 2\dot{x}\dot{y} + \ddot{z}\dot{z} = \frac{\partial\Omega^{(3b)}}{\partial x}\dot{x} + \frac{\partial\Omega^{(3b)}}{\partial y}\dot{y} + \frac{\partial\Omega^{(3b)}}{\partial z}\dot{z} \quad (2.36)$$

Since the potential function in the synodic frame does not depend directly on time, the right-hand side of Equation (2.36) is the total time derivative of Ω . The left-hand side might be written as the time derivative of the square speed. Performing an integration:

$$C = J(x, y, \dot{x}, \dot{y}, \dot{z}) = 2\Omega^{(3b)}(x, y, z) - (\dot{x}^2 + \dot{y}^2 + \dot{z}^2) \quad (2.37)$$

According to the formalism in [33] and [46], the Jacobi integral represents a five-dimensional manifold for the particle state in the six-dimensional phase space. It reduces therefore the possible motion to the hypersurface:

$$J^{-1}(C) = \{(x, y, \dot{x}, \dot{y}, \dot{z}) \in \mathbb{R}^6 \mid J - C = 0\} \quad (2.38)$$

where $C = J(\mathbf{x}_0)$ is the Jacobi constant associated with the initial condition $\mathbf{x}_0 = (x_0, y_0, \dot{x}_0, \dot{y}_0, \dot{z}_0)^T$. Moreover, thanks to the semi-definite positiveness of the kinetic term, it must be $2\Omega \geq J$, where the equality is valid only when the kinetic energy is zero. The Jacobi integral can be hence used to establish some allowed and forbidden regions for the motion of the third particle once initial conditions are specified. These regions are bounded by the *Hill's surfaces*, on which the velocity of the mass particle is identical null. The zero-velocity surfaces are defined in the configuration space by

$$\Omega^{-1}(C) = \{(x, y, \dot{x}) \in \mathbb{R}^3 \mid 2\Omega^{(3b)}(x, y, z) - C = 0\} \quad (2.39)$$

The Jacobi integral is directly related to the total energy E of the third body

$$J = -2E \quad (2.40)$$

which states that a high value for the Jacobi constant means a low energy at disposal. It's intuitive to think that, as the Jacobi constant decreases, the third body starts possessing enough energy to escape the gravitational attraction of the primaries.

2.3.2 Lagrangian points

Any set of numbers $(x, y, z, \dot{x}, \dot{y}, \dot{z})^T$ satisfying the Jacobi equation $C = 2\Omega^{(3b)}(x, y, z) - (\dot{x}^2 + \dot{y}^2 + \dot{z}^2)$ represents a possible motion for a given value of the constant C^4 . The six-dimensional manifold

$$G(x, y, z, \dot{x}, \dot{y}, \dot{z}) = C - 2\Omega(x, y, z) + (\dot{x}^2 + \dot{y}^2 + \dot{z}^2) = 0 \quad (2.41)$$

possesses singularities at points where partial derivatives of the manifold are zero.

$$G_{/x} = 0 \quad G_{/y} = 0 \quad G_{/z} = 0 \quad (2.42a)$$

$$G_{/\dot{x}} = \dot{x} = 0 \quad G_{/\dot{y}} = \dot{y} = 0 \quad G_{/\dot{z}} = \dot{z} = 0 \quad (2.42b)$$

The last three conditions entail the singularities reside on the surface of zero velocity, where $C = 2\Omega(x, y, z)$. The manifold singularities are then those points where

$$\Omega_{/x} = 0 \quad \Omega_{/y} = 0 \quad \Omega_{/z} = 0 \quad C = 2\Omega \quad (2.43)$$

It is important to note that the singularities of the manifold do not correspond to the singularities of the equations of motion, located instead at both primaries and infinitely away from the origin. What is more, the singularities of the manifold of the states of motion, when input in the dynamics, give rise to a null acceleration field, $\ddot{x} = \ddot{y} = \ddot{z} = 0$. It can be demonstrated by simple inspection, that in these points all the successive time derivatives of the components are zero. If the third particle is placed at an equilibrium point with zero velocity, it will stay there. For this reason the singularities of the manifold are equilibrium points for the third body dynamics and are often called *stationary points*, *libration points* or *Lagrangian points*. These special points are widely known in literature and have been studied thoroughly for their interesting dynamical and phase space portrait (see Section 1.3). A tool to determine the position of the Lagrangian points, addressed as L_i , will be presented. The conditions expressed by Equations (2.43) in expanded form are:

$$\Omega_{/x} = x - \frac{(1-\mu)(x+\mu)}{\rho_1^3} - \frac{\mu(x-1+\mu)}{\rho_2^3} = f(x, y, z) = 0 \quad (2.44a)$$

$$\Omega_{/y} = y(1 - \frac{1-\mu}{\rho_1^3} - \frac{\mu}{\rho_2^3}) = y \cdot g(x, y, z) = 0 \quad (2.44b)$$

$$\Omega_{/z} = -z(\frac{1-\mu}{\rho_1^3} + \frac{\mu}{\rho_2^3}) = z \cdot h(x, y, z) = 0 \quad (2.44c)$$

⁴ The superscript 3b is dropped beneath this point to simplify the notation.

From the last equation, either z or $h(x, y, z)$ has to be zero, but being both ρ_{12} and ρ_2 a product of a normalisation, they will always be positive and the function $h(x, y, z)$ possesses zeros only at infinity. The main consequence is that *the Lagrangian points must lie in the x-y synodic plane*, namely at $z = 0$. The second equation has a dual solution, $g(x, y, 0) = 0$ and $y = 0$. In the first case it's straightforward to verify that the solution evinces two points forming equilateral triangles with the primaries, consequently called the *equilateral or triangular libration points*.

$$g(x, y, 0) = 0 \implies \rho_1 = \rho_2 = 1 \quad (2.45)$$

These values satisfy both Equations (2.44a) and (2.44b). The analytical position of these points might be evaluated looking for which values of (x, y) the distance between the mass particle and the primaries is equal to one, directly from the definition of ρ_1 and ρ_2 . The results are:

$$L_4 : \left(\frac{1}{2} - \mu, \frac{\sqrt{3}}{2}, 0 \right)^T \quad L_5 : \left(\frac{1}{2} - \mu, -\frac{\sqrt{3}}{2}, 0 \right)^T \quad (2.46)$$

The case of $y = 0$ and $z = 0$ results in the *collinear libration points*, which lie in the line connecting the primaries in the synodic reference frame. Computation of the abscissas of the collinear points requires the solution of (2.44a), that may be more conveniently written as a quintic equation.

$$\begin{aligned} f(x, 0, 0) &= x(x + \mu)(x - 1 + \mu)|x + \mu||x - 1 + \mu| \\ &\quad - (1 - \mu)(x - 1 + \mu)|x - 1 + \mu| - \mu(x + \mu)|x + \mu| = 0 \end{aligned} \quad (2.47)$$

In Figure 2.8 the quintic polynomial corresponding to $\mu = 0.4$ is plotted. It's evident the function possesses only three real roots. The second libration point L_2 is located rightmost, near the lighter primary; the first Lagrangian point L_1 falls in-between the primaries, left of m_2 ; and the third stationary point L_3 stays left of the more massive primary, in the leftmost part. In the depicted case, the roots are well separated because of the high value of the mass parameter. As the mass parameter decreases towards values compatible with common primaries choice, $L_3 \rightarrow -1$ and both $L_{1,2}$ show a tendency to move towards and eventually to merge at $x = 1$. For the case of equally massive primaries, situation that could emerge in the study of stars formation for instance, the libration points set themselves in a symmetry condition with the first one at the frame centre and the other two symmetrically at $x = \pm 1.19840614455492$. The limits of the Lagrangian points are:

$$\begin{aligned} 0 &\leq x_{L_1} \leq 1 \\ 1 &\leq x_{L_2} \leq 1.271623175401214 \\ -1.19840614455492 &\leq x_{L_3} \leq -1 \end{aligned} \quad (2.48)$$

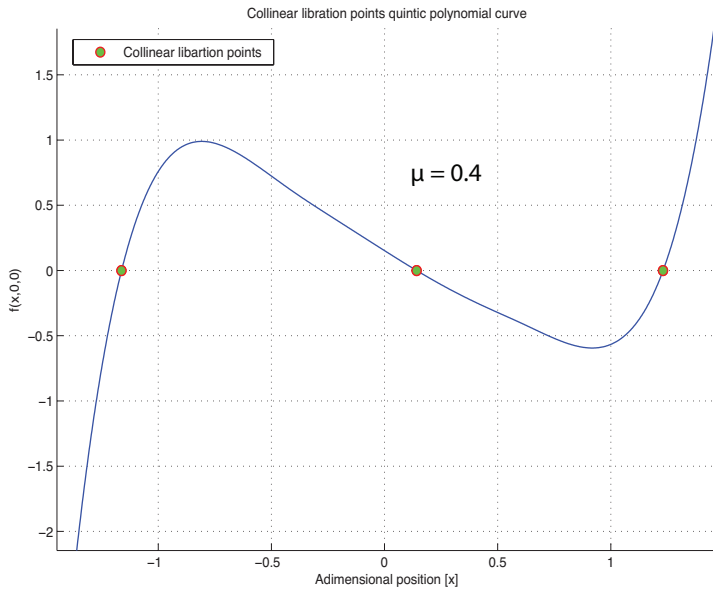


Figure 2.8: Quintic polynomial for the evaluation of the collinear libration points, $f(x, 0, 0)$

The limiting cases correspond to the two-body problem $\mu = 0$, and to the symmetric choice for the primaries $\mu = 0.5$, respectively. In Table 2.1 some interesting primaries choices are listed, together with their mass parameters μ and the location of the collinear points.

Table 2.1: Main gravitational systems mass parameters and adimensional position of the collinear points

System	μ	Collinear points		
		L_1	L_2	L_3
Sun-Jupiter	9.5388118e-04	0.932365449	1.06883066	-1.00039745044
Sun-Earth	3.0034806e-06	0.990026593	1.010034116	-1.00000125145
Earth-Moon	0.012150586	0.836915126	1.155682165	-1.0050626458

THE PLANAR CIRCULAR RESTRICTED THREE-BODY PROBLEM When the third mass particle is constrained to a planar motion at $z = 0$, the PCRTBP is formulated. The equations read:

$$\ddot{x} - 2\dot{y} = \Omega_{/x} \quad (2.49a)$$

$$\dot{y} + 2\dot{x} = \Omega_{/y} \quad (2.49b)$$

where the three-body potential is

$$\Omega = \frac{1}{2}(x^2 + y^2) + \frac{1-\mu}{\rho_1} + \frac{\mu}{\rho_2} + \frac{1}{2}\mu(1-\mu) \quad (2.50)$$

Terms ρ_1 and ρ_2 are now

$$\rho_1 = \sqrt{(x + \mu)^2 + y^2} \quad (2.51a)$$

$$\rho_2 = \sqrt{(x - 1 + \mu)^2 + y^2} \quad (2.51b)$$

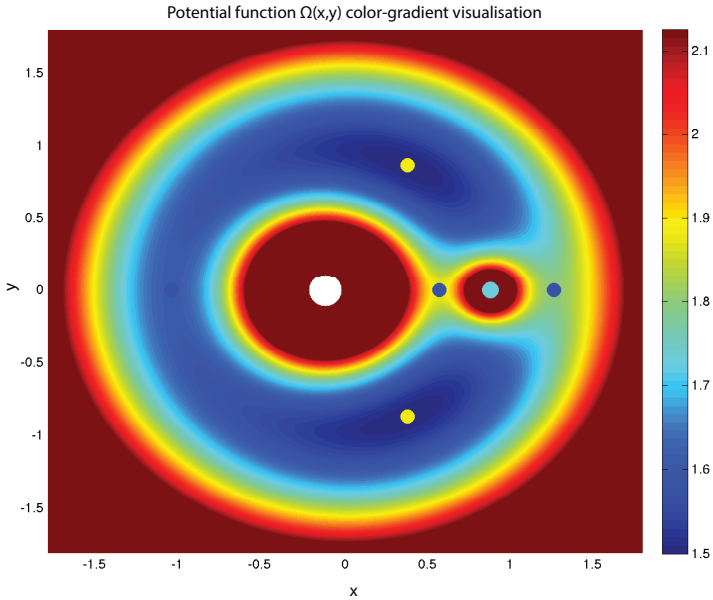


Figure 2.9: Color-gradient visualisation of the potential function Ω , for $z = 0$

The qualitative properties of motion are maintained as well as the Lagrangian points, defined exactly in the plane where the primaries revolve. The Jacobian integral represents now a three-dimensional manifold within the four-dimensional phase space of the third mass state. Once the initial conditions are given, it can be used to establish regions of possible motion and the Hill's surfaces.

$$C = J(x, y, \dot{x}, \dot{y}) = 2\Omega(x, y) - (\dot{x}^2 + \dot{y}^2) \quad (2.52)$$

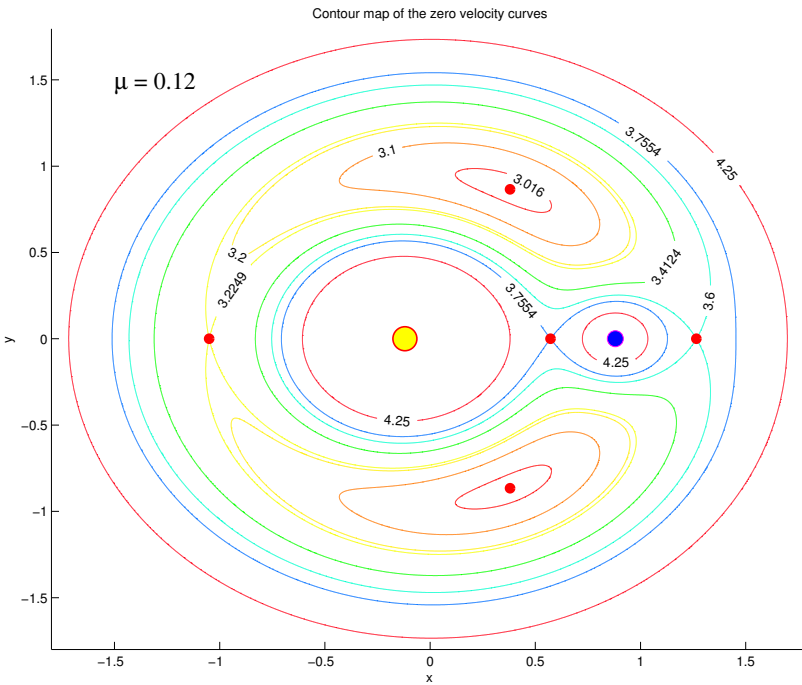


Figure 2.10: Contour map of $J = 2\Omega$, and zero-velocity curves for $\mu = 0.12$ at several interesting discrete values of the Jacobi constant, C

Figure 2.9 shows how the function $\Omega(x, y)$ varies along the adimensional synodic coordinates by means of a color-gradient visualisation. From a critical observation some important properties can be desummed:

- (i) $\Omega(x, y)$ is symmetric with respect to the x -axis, e. g. $\Omega(x, y) = \Omega(x, -y)$.
- (ii) The absolute minima of the function $\Omega(x, y)$ occur at the equilateral libration points, but is right-unbounded.

$$\Omega(x, y) \in [1.5, \infty)$$

- (iii) The minima of $\Omega(x, 0)$ occurs at the collinear points.
- (iv) The values of Ω at the libration points are ordered as follows

$$1.5 = \Omega(L_{4,5}) \leq \Omega(L_3) \leq \Omega(L_2) \leq \Omega(L_1) \leq 2.125$$

Figure 2.10 shows zero-velocity curves for special values of the Jacobi constant in the PCRTBP. The lines of the contours refer to the actual value of C . Four ranges of the values of the Jacobi constant are readily distinguishable, with four distinct types of curves of zero velocity, corresponding to four different types of areas of possible motion. Indicating $C(L_i) = C_i, i = 1, \dots, 5$, the regions of motion are separated by different values of the Jacobian constant.

- (a) For large values of the Jacobi constant $C > C_1$, the third mass particle can either orbit inside a closed *oval* region around one of the primary or orbit far away from them, outside an oval with comprehends both primaries. There is no communication path between these areas.
- (b) When the value of the Jacobian constant lies between C_2 and C_1 , that is $C_2 \leq C \leq C_1$, particle exchange between the neighbourhood of the two primaries becomes possible, but the third body still remains either outside the large oval or within the *dumbbell-shaped* area comprising the primaries. The first available communication point occurs at L_1 , when $C = C_1$. As the Jacobian constant decreases the communication tunnel gets wider and wider, until the two zero-velocity curves collapses at L_2 , for $C = C_2$.
- (c) The next phase occurs for values of the Jacobian constant satisfying $C_3 \leq C \leq C_2$. The allowed region of motion opens up forming *horseshoe-shaped* zero velocity curves, firstly at the second Lagrangian point L_2 . The communication tunnel occurs near the primary with smaller mass and widens until the Jacobian constant is equal to C_3 .
- (d) For values of the Jacobian constant between C_3 and the value at the equilateral libration points, $3 \leq C \leq C_3$, the *tadpole-shaped* forbidden regions surrounding both L_4 and L_5 shrink as $C \rightarrow 3$, until motion is possible everywhere provided that the energy of the third particle is large enough to sustain it (i.e., $E = -1.5$).

2.3.3 Motion near the equilibrium points

Massless objects placed at the five equilibrium points are stationary, in the sense that they are relatively still with respect to the synodic frame. Not only are these equilibrium points solutions of the equations of motion, but near these points other families of solutions exist. These orbits are remarkably important and have been object of thorough studies on space mission design in the past decades. In the framework of the RTBP these trajectories offer interesting possibilities from the point of view of space exploration. Provided they are stable, an observation platform could be practically inserted into Sun orbit and station-keeping would be very low. The mission SOHO by NASA for example, is exploiting a Halo orbit around L_1 in the Earth-Sun system as a nominal station orbit.

If a dynamical system is in a state of equilibrium, from a mathematical perspective it will remain in the same state as time goes towards infinity. However, a real system might be subjected to external non-accounted disturbances. It is then of considerable practical interest to establish the system response to these disturbances. *Stability* of the dynamical system is concerned with such behaviour. In a very intuitive manner, if the motion after a disturbance remains

bounded or in the neighbourhood of the equilibrium state after it is disturbed, it exhibits stable properties.

The stability of the Lagrangian points is hence of paramount interest. If $\mathbf{x} = (x, y, z, \dot{x}, \dot{y}, \dot{z})^T$, the differential system (2.33) can be put in the more familiar state-space form (2.5).

$$\begin{aligned}\dot{x}_1 &= x_4 & \dot{x}_4 &= 2x_5 + \Omega_{/x_1} \\ \dot{x}_2 &= x_5 & \dot{x}_5 &= 2x_4 + \Omega_{/x_2} \\ \dot{x}_3 &= x_6 & \dot{x}_6 &= \Omega_{/x_3}\end{aligned}\quad \rightarrow \quad \dot{\mathbf{x}} = \mathbf{f}(\mathbf{x}) \quad (2.53)$$

The libration points are fixed points of the autonomous RTBP vector field described by (2.53). Let $\mathbf{L}_i = (l_i^{(x)}, l_i^{(y)}, 0, 0, 0, 0)^T$, $i = 1, \dots, 5$, be the vector representing the i -th libration point, then

$$\mathbf{f}(\mathbf{L}_i) = \mathbf{0} \quad \forall i = 1, \dots, 5 \quad (2.54)$$

The dynamics of the particle under the influence of the RTBP vector field is chaotic in nature, stemming from the non-linear terms in the partial spatial derivatives of the potential function, $\Omega_{/x_i}$. To inquire the stability properties of an equilibrium point of a chaotic differential system, concept of stability for non-linear dynamical systems shall first be introduced. As discussed in [44], the definition Lyapunov provided furnishes a strong mathematical tool to evaluate stability.

The equilibrium solution \mathbf{L} , for $t \geq t_0$, of the dynamical system (2.53) is stable according to Lyapunov if, given any $\varepsilon > 0$, there exists a $\delta(\varepsilon) > 0$ such that any solution $\varphi(t)$ satisfying

$$\|\varphi(t_0) - \mathbf{L}\| < \delta \quad (2.55)$$

satisfies

$$\|\varphi(t) - \mathbf{L}\| < \varepsilon \quad t > t_0 \quad (2.56)$$

Formally, the solution is asymptotically stable if

$$\lim_{t \rightarrow \infty} \mathbf{x} = \mathbf{L} \quad (2.57)$$

This definition provides a solid and proved mathematical formulation for the concept of stability. However, due to the chaotic nature, it is rather complicated to establish directly and precisely the stability regions of a non-linear dynamical system. An infinitesimally small change of initial condition might lead to

large variations of the temporal response, even not affecting its stability. This behaviour demands a lot of inspections for all possible configurations and sets of initial conditions.

On the other hand, it is rather straightforward to analyse stability properties of the linear dynamical system

$$\dot{\mathbf{x}} = \mathcal{A}\mathbf{x} \quad \mathcal{A} = \left[\frac{\partial \mathbf{f}}{\partial \mathbf{x}} \right]_{\mathbf{x}=\mathbf{x}_0} \quad (2.58)$$

where \mathcal{A} is the constant matrix, by inspecting the spectrum of matrix \mathcal{A} . Matrix \mathcal{A} is the Jacobian of the vector field, evaluated at the initial state. From basic knowledge of state-space and frequency-domain analysis it is known that the roots of the characteristic polynomial of the dynamical system are the sole responsible for its stability. Let $s \in \mathbb{C}^1$ be a complex number, then the characteristic polynomial can be calculated from the determinant:

$$|s\mathcal{I} - \mathcal{A}| = 0 \quad (2.59)$$

It is evident that the roots of this polynomial coincides with the eigenfrequencies of the dynamical system, when solution of the form $\mathbf{x} = e^{\mathcal{A}t}\mathbf{x}_0 = \sum_{i=1}^6 c_i e^{s_i t}$ is attained. In particular it is proved (see Friedland [15]) that:

- 1 If the real parts of all the characteristic roots are strictly negative, then the equilibrium point is asymptotically stable

$$\operatorname{Re}(s_i) < 0 \quad \forall i \quad \rightarrow \quad \text{asymptotic stability}$$

- 2 If any eigenvalue possesses strictly positive real part, the equilibrium point is unstable.

$$\exists i \mid \operatorname{Re}(s_i) > 0 \quad \rightarrow \quad \text{instability}$$

- 3 If all the characteristic roots have nonpositive real parts, but one or more has a zero real part or equivalently is pure imaginary, the stability depends on the multiplicity of this eigenvalue. In details, if it is a simple root the equilibrium point is simply stable, otherwise if the root is multiple the equilibrium point is unstable.

$$\exists i \mid \operatorname{Re}(s_i) = 0 \quad \wedge \quad \begin{cases} s_i \text{ is a simple root} & \rightarrow \quad \text{simple stability} \\ s_i \text{ is a multiple root} & \rightarrow \quad \text{instability} \end{cases}$$

From the qualitative point of view an equilibrium point is termed:

- *hyperbolic*, if no one of the eigenvalues has zero real part;

- *node*, if all the characteristic roots are real and of concordant sign; in particular, the node is stable (unstable) if the eigenvalues are all negative (positive);
- *saddle point*, if both eigenvalues with positive and negative real parts exist;
- *center or vortex*, if the characteristic roots are all pure imaginary;
- *focus or spiral point*, if it is related to a couple of conjugate complex eigenvalues; the sign of their real part determines again the stability.

Thanks to theorems pertaining to the dynamical system theory and under certain conditions, stability of a nonlinear dynamical system may be assessed using the results obtained from the stability investigation of the equivalent linearised system. For example, *Hartman-Grobman theorem* states that the behaviour of a dynamical system near a hyperbolic equilibrium point is qualitatively the same as the behaviour of its linearisation near this equilibrium point, provided that no eigenvalue of the linearisation has zero real part. In this case stability of the linearised system provides a sufficient condition to the asymptotical stability of the non-linear one. Similar condition holds for its counterpart, when instability from real part eigenvalues is found. For pure-imaginary eigenvalues, so-called critical cases result and investigation of the stability of the non-linear system requires a much deeper insight to its dynamics and cannot be established a priori based in its linearised system. In Meyer et al. [32] stability properties of the n-body problem is deeply investigated under the perspective of the Hamiltonian system theory and the results of *KAM (Kolmogorov-Arnold-Moser) theorem* are presented. Briefly, under certain conditions (i. e., small and smooth perturbations and sufficiently irrational map winding number) a small perturbation of a conservative dynamical system might result in a lasting quasi-periodic orbit. The KAM theorem partly resolves the *small-divisor* problem (see Jorba and Masdemont [28]) that arises in the perturbation theory of classical mechanics.

The mapping theory guarantees that the linearised equations still possess fundamental information, as far as the stability is concerned. Since stability is implicitly defined for an equilibrium point, it is convenient to study the motion in its neighbourhood by means of a coordinate transformation, which shifts the center of the new reference at the equilibrium point itself. The transformation affects only the position in the synodic plane, and it is simply achieved by:

$$x = l_i^{(x)} + \xi \quad y = l_i^{(y)} + \eta \quad (2.60)$$

The linearisation is carried out expanding the potential in power series, by means of a simple Taylor series truncated at the second order around the equilibrium point. The expansion yields:

$$\Omega(\xi, \eta, z) = \Omega^0 + \overbrace{\Omega_{/x}^0 \xi + \Omega_{/y}^0 \eta + \Omega_{/z}^0 z}^{=0} + \frac{1}{2} \Omega_{/xx}^0 \xi^2 + \frac{1}{2} \Omega_{/yy}^0 \eta^2 + \frac{1}{2} \Omega_{/zz}^0 z^2 + \Omega_{/xy}^0 \xi \eta + \Omega_{/xz}^0 \xi z + \Omega_{/yz}^0 \eta z + \mathcal{O}(3) \quad (2.61)$$

where⁵ $\Omega^0 = \Omega(l_i^{(x)}, l_i^{(y)}, 0)$. Substituting into the differential Eq. (2.33) and applying the coordinate shift, the system becomes:

$$\ddot{\xi} - 2\dot{\eta} = \Omega_{/xx}^0 \xi + \Omega_{/xy}^0 \eta + \Omega_{/xz}^0 z + \mathcal{O}(2) \quad (2.62a)$$

$$\ddot{\eta} + 2\dot{\xi} = \Omega_{/xy}^0 \xi + \Omega_{/yy}^0 \eta + \Omega_{/yz}^0 z + \mathcal{O}(2) \quad (2.62b)$$

$$\ddot{z} = \Omega_{/xz}^0 \xi + \Omega_{/yz}^0 \eta + \Omega_{/zz}^0 z + \mathcal{O}(2) \quad (2.62c)$$

The complete characterisation of the linearised dynamical system requires the knowledge of the potential function quadratic expansion at the libration points. From the results of section 2.3.2 it is quite forward to derive:

$$\begin{aligned} \Omega_{/xx} &= f_{/x} = 1 + (1 - \mu) \frac{2(x + \mu)^2 - (y^2 + z^2)}{\rho_1^5} \\ &\quad + \mu \frac{2(x - 1 + \mu)^2 - (y^2 + z^2)}{\rho_2^5} \end{aligned} \quad (2.63a)$$

$$\Omega_{/yy} = g + yg_{/y} = 1 - \frac{1 - \mu}{\rho_1^3} - \frac{\mu}{\rho_2^3} + 3y^2 \left(\frac{1 - \mu}{\rho_1^5} + \frac{\mu}{\rho_2^5} \right) \quad (2.63b)$$

$$\Omega_{/zz} = -\frac{1 - \mu}{\rho_1^3} - \frac{\mu}{\rho_2^3} - zg_{/z} \quad (2.63c)$$

$$\Omega_{/xy} = f_{/y} = yg_{/x} = 3y \left[\frac{(1 - \mu)(x + \mu)}{\rho_1^5} + \frac{\mu(x - 1 + \mu)}{\rho_2^5} \right] \quad (2.63d)$$

$$\Omega_{/xz} = zg_{/x} \quad (2.63e)$$

$$\Omega_{/yz} = zg_{/y} \quad (2.63f)$$

Equilibrium points lie on the synodic plane, equations (2.63e) and (2.63f) directly imply that $\Omega_{/xz} = \Omega_{/yz} = 0$. The linearised dynamics of the RTBP along the z direction is hence decoupled from the in-plane dynamics. This allows to solve and analyse the two distinct dynamics separately. Moreover, it is clear from (2.63c) that the linearised z dynamics is always at least simply stable, or

⁵ The evaluation of the potential derivatives is performed after the derivation.

periodic, because $\Omega_{/zz} < 0$ for every mass parameter selection. In literature, the square of its oscillation frequency is often referred as c_2 , i.e.,

$$c_2 = \frac{1-\mu}{\rho_1^3} + \frac{\mu}{\rho_2^3} \quad (2.64)$$

It remains to study the in-plane dynamics. The characteristic polynomial can be found by assuming a proper complex exponential planar motion and by looking for the only non-trivial solution.

$$\begin{vmatrix} s^2 - \Omega_{/xx}^0 & -2s - \Omega_{/xy}^0 \\ 2s - \Omega_{/xy}^0 & s^2 - \Omega_{/yy}^0 \end{vmatrix} = s^4 + (4 - \Omega_{/xx}^0 - \Omega_{/yy}^0)s^2 + \Omega_{/xx}^0 \Omega_{/yy}^0 - (\Omega_{/xy}^0)^2 = 0 \quad (2.65)$$

At this point the sign of the second derivatives of the potential determines the phase space around the equilibrium points. Equilateral points and collinear points shall be treated separately, since the potential behaves in a different fashion in these points, as clear from figure 2.9.

EQUILATERAL POINTS The coordinates of the triangular Lagrangian points are given by equation (2.46).

$$\Omega_{/xx}(L_{4,5}) = \frac{3}{4} \quad (2.66a)$$

$$\Omega_{/yy}(L_{4,5}) = \frac{9}{4} \quad (2.66b)$$

$$\Omega_{/xy}(L_{4,5}) = \pm \frac{3\sqrt{3}}{2} \left(\frac{1}{2} - \mu \right) \quad (2.66c)$$

According to these values the characteristic polynomial reads

$$s^4 + s^2 + \frac{27}{4}\mu(1-\mu) = 0 \quad \rightarrow \quad s = \pm \sqrt{\frac{1}{2}(-1 \pm \sqrt{1-27\mu(1-\mu)})} \quad (2.67)$$

It is easy to show that the domain of the characteristic roots depends on the discriminant sign. There is a threshold for the mass parameter, $\mu = 0.038520896504551$, up to which the equilateral points are stable. Beyond that value, the dynamics becomes unstable, first for a double zero eigenvalue and then because of a positive real part. It's interesting to note that, within the solar system, every possible RTBP, but the pair Pluto-Charon, features stable equilateral points. For this reason they are not of major interest, since the unstable manifolds of the gravitational field cannot be exploited. Regarding the primary objective of the present work, the stability of the linearised field in the

neighbourhood of the triangular points, translates into stability of the real n -body problem flow. In this framework refinement of orbits poses no apparent challenges.

COLLINEAR POINTS The coordinates of the collinear Lagrangian points are given by equation (2.47). The expansion of the potential function around them can be written as function of the sole parameter c_2 .

$$\Omega_{/xx}(L_{1,2,3}) = 1 + 2c_2 > 0 \quad (2.68a)$$

$$\Omega_{/yy}(L_{1,2,3}) = 1 - c_2 < 0 \quad (2.68b)$$

$$\Omega_{/xy}(L_{1,2,3}) = 0 \quad (2.68c)$$

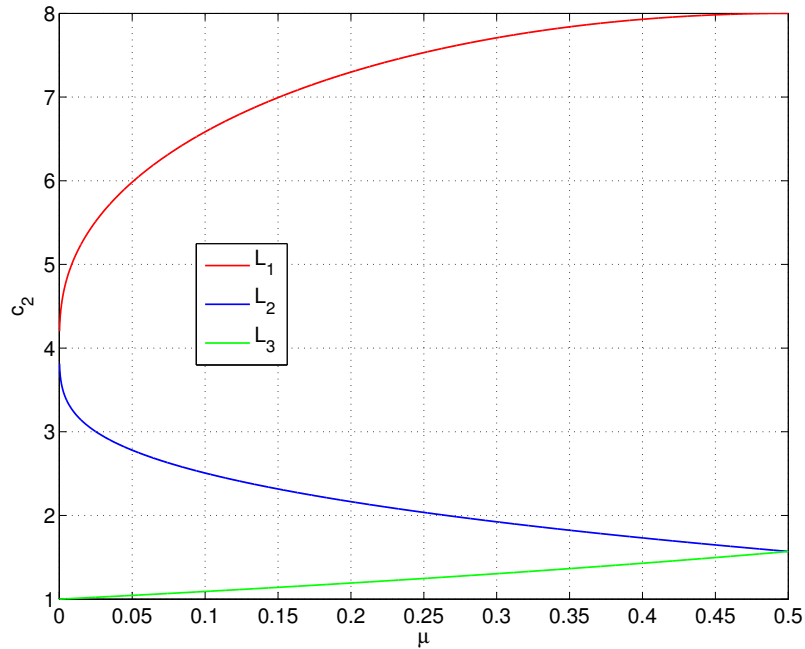


Figure 2.11: Parameter c_2

It's proved that the parameter c_2 is always a positive number greater or equal than one, one being a limiting case for the third libration point and the value occurring at both equilateral points. Figure 2.11 shows the trend of this parameter as function of μ , for each of the collinear points. Accordingly, the characteristic polynomial yields:

$$s^4 + 2\beta_1 s^2 - \beta_2^2 = 0 \quad \rightarrow \quad \begin{cases} s_{1,2} = \pm \sqrt{-\beta_1 + \sqrt{\beta_1^2 + \beta_2^2}} \in \mathbb{R} \\ s_{3,4} = \pm \sqrt{-\beta_1 - \sqrt{\beta_1^2 + \beta_2^2}} \in i\mathbb{R} \end{cases} \quad (2.69)$$

where

$$\begin{aligned}\beta_1 &= \frac{1}{2}(4 - \Omega_{/xx}^0 - \Omega_{/yy}^0) = 2 - c_2 \\ \beta_2^2 &= -\Omega_{/xx}^0 \Omega_{/yy}^0 = 2c_2^2 - c_2 - 1\end{aligned}\quad (2.70)$$

The linearised vector field at the collinear points exhibits a behaviour of the kind *center x center x saddle* for every μ , these equilibrium points are hence unstable. Related to their centre-like nature, the motion of the third body is periodic or quasi-periodic; instead, according to their saddle-like nature, all the collinear points are classified as unstable. The linearised dynamical system about the collinear liberation points takes then the form

$$\ddot{\xi} - 2\dot{\eta} - (1 + 2c_2)\xi = 0 \quad (2.71a)$$

$$\dot{\eta} + 2\dot{\xi} + (c_2 - 1)\eta = 0 \quad (2.71b)$$

$$\ddot{z} + c_2 z = 0 \quad (2.71c)$$

After some trigonometrical calculation the solution of the linearised vector field yields:

$$\xi(t) = A_1 e^{s_1 t} + A_2 e^{-s_1 t} + A_x \cos(\lambda t + \varphi) \quad (2.72a)$$

$$\eta(t) = \alpha_1(A_1 e^{s_1 t} - A_2 e^{-s_1 t}) - k A_x \sin(\lambda t + \varphi) \quad (2.72b)$$

$$z(t) = A_z \cos(\sqrt{c_2}t + \psi) \quad (2.72c)$$

where $A_1, A_2, A_x, A_z, \phi, \psi$ are constants to be determined from the initial conditions; and the other are known parameters function of the eigenvalues of the system.

$$s_{3,4} = \pm i\lambda \quad \alpha_1 = \frac{s_1^2 - 1 - 2c_2}{2s_1} \quad k = \frac{\lambda^2 + 1 + 2c_2}{2\lambda}$$

It is clear that stable solution can be sought by requiring the saddle part to be null, or equivalently $A_1 = A_2 = 0$. In this case, the linearised problem features periodic solutions close to the equilibrium points, characterised however by infinitesimal amplitudes.

The orbits related to the sole linear oscillators, in-plane and parallel to the z direction, are called the *Lyapunov orbits*, planar and vertical, respectively. The family of out-of-plane Lyapunov solutions ($x = y = 0$) is harmonic at frequency $\sqrt{c_2}$. On the other hand, the family of Lyapunov solutions tangent to the synodic plane ($z = 0$) is periodic at frequency λ . Examples of planar Lyapunov orbits for the Earth-Moon $L_{1,2}$ cases are sown in Figure 2.12. Other

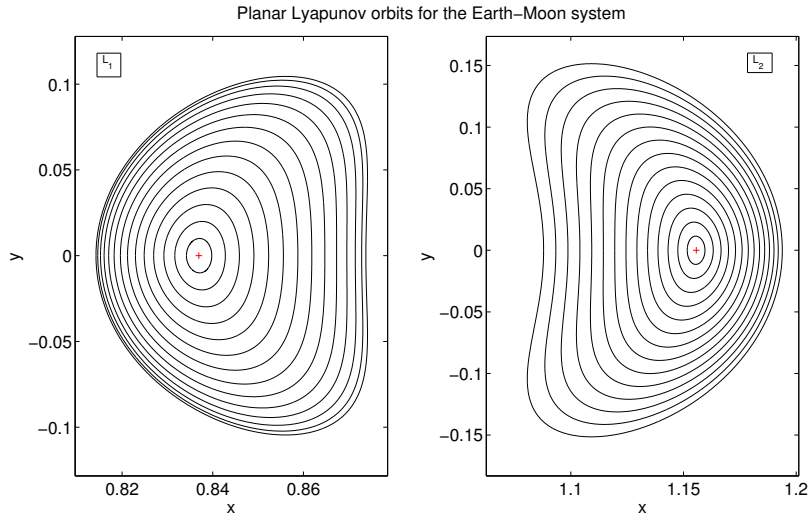


Figure 2.12: Planar Lyapunov orbits family for the Earth-Moon system around the first (left) and second (right) Lagrangian point

interesting solutions are the two-dimensional invariant tori related to the *Lissajous orbits*, obtained as product of the two linear oscillations.

Space mission design usually involves Lyapunov orbits with prescribed wider amplitude and governed by the complete dynamics of the problem. The computation of these orbits must account for the non-linear term that arise in the real restricted problem. These, in a way more real solutions, are obtained through a numerical approach, based on *perturbation techniques*, in order to correct the analytic initial estimates, and on *continuation techniques*, in order to expand the infinitesimal orbits. An example of solution that directly stems from the non-linear terms of the dynamical system is the family of *Halo orbits*. Halo orbits are periodic orbits which bifurcate from the planar Lyapunov orbits when the in-plane and out of plane frequencies are equal. This is a 1:1 resonance that appears as a consequence of the nonlinear terms of the equations and, hence, these 1-D invariant tori have to be searched as series expansion with a single frequency. In details, once the out-of-plane A_z amplitude overcomes a limit value, the frequency of the in-plane oscillatory motion achieves the value of the frequency of the one out of the plane, and three-dimensional halo orbits emerge. Figure 2.13 represents a family of Halo orbits of the L_1 Sun-Jupiter system, calculated via high-order differential corrections (Topputo [46]).

In order to describe the dynamics in a relatively big neighbourhood of the collinear points and to find these families of periodic and quasi-periodic orbits around the fixed points, two numerical approaches are mainly used. The first method is also called reduction to the centre manifold. This process is done by properly expanding the nonlinear terms and uncoupling (up to a high order)

the hyperbolic directions from the elliptic ones. The restriction to the invariant manifold tangent to these elliptic directions is a two degrees of freedom Hamiltonian system with an elliptic equilibrium point at the origin. For a complete treatment of this method the reader is remanded to [28].

The second is the famous *Lindstedt-Poincaré method*, used to compute accurately some of the solutions of the center manifold. The numerical procedure developed by the *Barcelona Group* can be found in Masdemont and Mondelo [31]. This process is based on finding a parametric family of trigonometric expansions that satisfy the equations of motion, up to a sufficiently high order. The advantage of the Lindstedt-Poincaré method is that it produces explicit formulae for the solutions in the initial coordinates, so that single compact parametric expressions for all the trajectories might be obtained, whose parameters are the amplitudes for each frequency. The main disadvantage is that a bifurcation cannot be contained in such expressions.

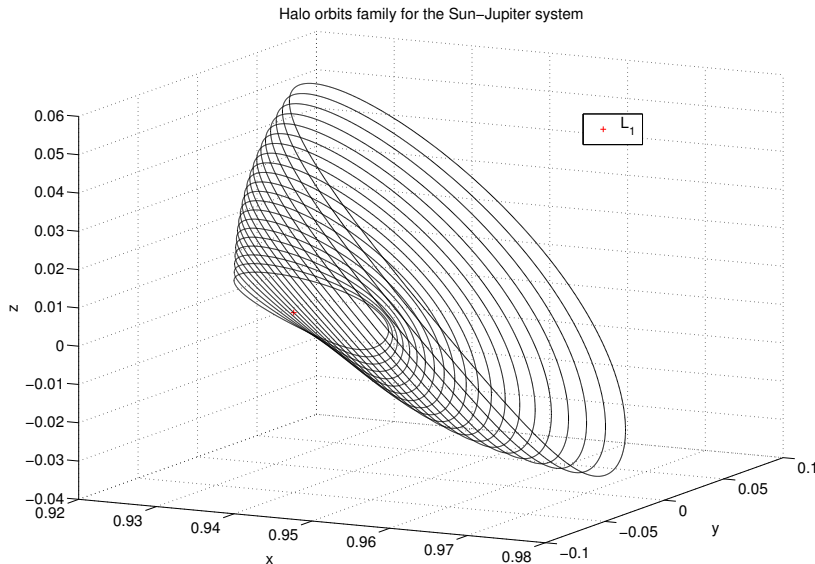


Figure 2.13: Halo orbits family around the first collinear point L_1 of the Sun-Jupiter gravitational system

The potential function has been expanded by means of Taylor series and terms up to the second order have been retained. According to Richardson [36], Legendre polynomial are used to retain high-order terms.

$$\frac{1}{\sqrt{(x-a)^2 + y^2 + z^2}} = \frac{1}{a} \sum_{n=0}^{\infty} \left(\frac{\rho}{a}\right)^n P_n\left(\frac{x}{\rho}\right) \quad (2.73)$$

where $\rho^2 = x^2 + y^2 + z^2$ and P_n is the Legendre polynomial of order n that can be express through Rodrigues' formula:

$$P_n(y) = \frac{1}{2^n n!} \frac{d^n}{dy^n} [(x^2 - 1)^n] \quad (2.74)$$

The linearised equation hence read:

$$\ddot{\xi} - 2\dot{\eta} - (1 + 2c_2)\xi = \frac{\partial}{\partial x} \sum_{n \geq 3} c_n(\mu) \rho^n P_n\left(\frac{x}{\rho}\right) \quad (2.75a)$$

$$\ddot{\eta} + 2\dot{\xi} + (c_2 - 1)\eta = \frac{\partial}{\partial y} \sum_{n \geq 3} c_n(\mu) \rho^n P_n\left(\frac{x}{\rho}\right) \quad (2.75b)$$

$$\ddot{z} + c_2 z = \frac{\partial}{\partial z} \sum_{n \geq 3} c_n(\mu) \rho^n P_n\left(\frac{x}{\rho}\right) \quad (2.75c)$$

The solution of the linear periodic part of these equations remains unvaried, same as (2.72). These linear solutions are already Lissajous trajectories. Following the procedure in Gómez et al. [19], when the nonlinear terms (in Legendre polynomials form) are considered, the complete solution is sought as formal series in powers of the amplitudes A_x and A_z of the type:

$$\begin{Bmatrix} \xi \\ \eta \\ z \end{Bmatrix} = \sum_{i,j=1}^{\infty} \left(\sum_{|k| \leq i, |m| \leq j} \begin{Bmatrix} \xi \\ \eta \\ z \end{Bmatrix}_{ijkm} \begin{Bmatrix} \cos \\ -\sin \\ \cos \end{Bmatrix}_{(k\vartheta_1 + m\vartheta_2)} \right) A_x^i A_z^j$$

where $\vartheta_1 = \omega t + \varphi$ and $\vartheta_2 = vt + \psi$. Due to the presence of nonlinear terms, the frequencies ω and v cannot be kept equal to λ and $\sqrt{c_2}$, and they must be expanded in powers of the amplitudes too.

$$\omega = \lambda + \sum_{i,j=1}^{\infty} \omega_{ij} A_x^i A_z^j \quad v = \sqrt{c_2} + \sum_{i,j=1}^{\infty} v_{ij} A_x^i A_z^j$$

The goal is to compute the coefficients ξ_{ijkm} , η_{ijkm} , z_{ijkm} , ω_{ijkm} and v_{ijkm} recurrently up to a finite order $N = i + j$. Inserting the linear solution in the equations of motion, a remainder for each equation is obtained, which is a series in A_x and A_z beginning with terms of order $i + j = 2$. In order to get the coefficients of order two, this known order 2 terms must be equated to the unknown order 2 terms of the left hand side of the equations. The general step is similar. It assumes that the solution has been computed up to a certain order $n - 1$. Then, it is substituted in the right hand side of the RTBP equations, producing terms of order n in A_x and A_z . This known n -order terms must be equated with the unknown terms of order n of the left hand side.

3

EQUATIONS OF MOTION IN THE ROTO-PULSATING FRAME

In this chapter the equations of the n -body problem will be derived using a Lagrangian formalism. This choice directly follows from the simplicity of the problem statement in the Lagrangian Mechanics framework, as well for the readiness of being formalised and implemented in a programming code. On the other hand, the Hamiltonian formalism, although it may give a better understanding of the phase space portrait of the dynamical problem, tends to weaken the physical meaning of the terms involved, making it harder to understand what might be neglected during computations and what instead represents a large source of perturbation for the problem at hand¹. The set of differential equations governing the particle motion are written as perturbation of the well-known restricted three-body problem, in this way a better insight of each term will be given and explained. Moreover, this model is easily ascribable to simpler gravitational models, such as the RTBP or the two-body problem, by simply deleting proper terms from the equation. The cardinal motivation underlying this choice is that, mainly three-body orbits are to be corrected into the real ephemeris dynamics. Hence, dealing with a differential system which eventually resembles the one describing the RTBP and that possesses common features, makes the refinement procedure more efficient and helps better understanding the corrections generated in the refined orbits. Dynamical substitutes of libration points and quasi-periodic orbits about them are better described into the bargain in a framework which still somehow embeds the dynamical properties which allowed these solutions to exist.

In the last part of the chapter, a Fourier analysis of the motion equation coefficients is performed, in order to get some precious information on the phase space portrait and harmonic content of the real ephemeris model.

¹ Citing W. R. Hamilton: *Lagrange has perhaps done more than any other to give extent and harmony to such deductive researches by showing that the most varied consequences... may be derived from one radical formula, the beauty of the method so suiting the dignity of the results as to make his great work a kind of scientific poem.*

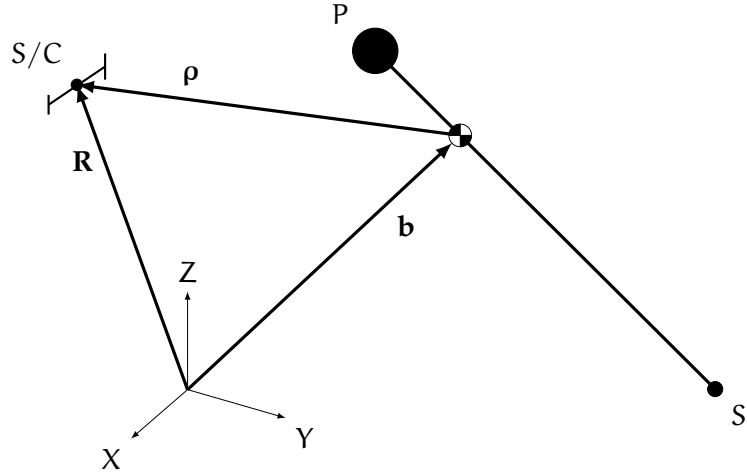


Figure 3.1: Transformation geometry of the three-body problem in an inertial reference frame, XYZ

3.1 CHANGE OF COORDINATES AND LAGRANGIAN FORMULATION

The complete characterisation of the dynamics happens through a rotation of the n-body problem equations of motion. The transformation between the solar system barycentric reference frame, hereafter addressed as SSB for simplicity, and the non-inertial reference is

$$\mathbf{R} = \mathbf{b} + k\mathcal{C}\rho \quad (3.1)$$

where:

$$\mathbf{b}(t) = \frac{m_p \mathbf{R}_p + m_s \mathbf{R}_s}{m_p + m_s} \quad k = k(t) \quad \mathcal{C} = \mathcal{C}(t)$$

The subscripts P and S refers to the primary and secondary body, respectively. The transformation is composed by two parts, and the geometry of the problem is illustrated in Figure 3.1. The first is a translation of the frame centre from the solar system barycenter to the primaries centre of mass \mathbf{b} . The second is a rotation by means of the cosine angle matrix \mathcal{C} , and a scaling by means of the time-dependent factor $k(t)$. The rotation is such that the primaries chosen are always aligned with the x-axis of the new frame. However, general orbits won't stay on a fixed position along the axis but will rather oscillate according to their elliptical motion. For this reason the scaling factor k , chosen as the punctual distance between the primaries, adjusts their positions so as to be fixed in time with respect to the new frame of reference. As a result, the reference the equations have been trasposed to, rotates in a nonuniform fashion and pulsates in order to guarantee some convenient features, suggested mainly from the RTBP.

In this thesis the new reference frame will be addressed as *roto-pulsating reference frame*. Note that the roto-pulsating frame is in complete accordance with the synodic reference introduced by Euler to simplify the RTBP. It's straightforward to demonstrate that the positions of the primaries in the new frame will be fixed and formally equivalent to the one used in the RTBP. Moreover, the adimensional velocity of such bodies in the non-inertial frame is by definition null.

$$\rho_P = (-\mu, 0, 0)^T \quad \rho_S = (1 - \mu, 0, 0)^T \quad (3.2)$$

$$\dot{\rho}_P = 0 \quad \dot{\rho}_S = 0 \quad (3.3)$$

Before starting the computation of the Lagrangian of the dynamical system, it'll be rather useful to properly define k and \mathcal{C} and to evaluate their time derivatives. Vectors indicated with small letters represent relative vectors of the less massive body with respect to the main primary.

$$[\mathbf{i}]_{\text{relative}} = [\mathbf{I}]_S - [\mathbf{I}]_P \quad \Rightarrow \quad \begin{cases} \mathbf{r} = \mathbf{R}_S - \mathbf{R}_P \\ \mathbf{v} = \mathbf{V}_S - \mathbf{V}_P \\ \mathbf{a} = \mathbf{A}_S - \mathbf{A}_P \\ \mathbf{j} = \mathbf{J}_S - \mathbf{J}_P \\ \mathbf{s} = \mathbf{S}_S - \mathbf{S}_P \end{cases}$$

where \mathbf{J} and \mathbf{S} are the jerk, or overacceleration, and the snap, fourth time-derivative of the position vector \mathbf{R} , respectively. With this notation

$$k = \|\mathbf{r}\| \quad (3.4a)$$

$$\dot{k} = \frac{\mathbf{r} \cdot \mathbf{v}}{k} \quad (3.4b)$$

$$\ddot{k} = \frac{k(v^2 + \mathbf{r} \cdot \mathbf{a}) - \dot{k}(\mathbf{r} \cdot \mathbf{v})}{k^2} \quad (3.4c)$$

Another useful parameter in the definition of the roto-pulsating frame is the relative angular momentum per unit mass of the primaries, $\mathbf{h} = \mathbf{r} \wedge \mathbf{v}$. Indeed it determines a direction that is punctually normal to the plane formed by the relative position and velocity vectors.

$$h = \|\mathbf{r} \wedge \mathbf{v}\| \quad (3.5a)$$

$$\dot{h} = \frac{(\mathbf{r} \wedge \mathbf{v}) \cdot (\mathbf{r} \wedge \mathbf{a})}{h} \quad (3.5b)$$

$$\ddot{h} = \frac{h\{(\mathbf{r} \wedge \mathbf{a})^2 + (\mathbf{r} \wedge \mathbf{v}) \cdot [\mathbf{v} \wedge \mathbf{a} + \mathbf{r} \wedge \mathbf{j}]\} - \dot{h}(\mathbf{r} \wedge \mathbf{v}) \cdot (\mathbf{r} \wedge \mathbf{a})}{h^2} \quad (3.5c)$$

The unit vectors $\mathbf{e}_i \in \mathbb{R}^3$, $i = 1, 2, 3$, forming the columns of the cosine angle matrix \mathcal{C} are defined such that the x -axis is aligned with the punctual relative distance between the primaries. The z -axis must be orthogonal to the plane containing the relative position and velocity, that is it must be parallel to \mathbf{h} . The y -axis comes as the result of a right-hand orthogonal tern, that is, the y -axis is the binormal of x and z .

$$\begin{aligned}\mathcal{C} &= [\mathbf{e}_i] & \mathbf{e}_1 &= \frac{\mathbf{r}}{k} \\ & & \mathbf{e}_2 &= \mathbf{e}_3 \wedge \mathbf{e}_1 \\ & & \mathbf{e}_3 &= \frac{\mathbf{r} \wedge \mathbf{v}}{h}\end{aligned}\tag{3.6}$$

$$\begin{aligned}\dot{\mathcal{C}} &= [\mathbf{e}_i] & \dot{\mathbf{e}}_1 &= \frac{k\mathbf{v} - \dot{k}\mathbf{r}}{k^2} \\ & & \dot{\mathbf{e}}_2 &= \mathbf{e}_3 \wedge \mathbf{e}_1 + \mathbf{e}_3 \wedge \dot{\mathbf{e}}_1 \\ & & \dot{\mathbf{e}}_3 &= \frac{h(\mathbf{r} \wedge \mathbf{a}) - \dot{h}(\mathbf{r} \wedge \mathbf{v})}{h^2}\end{aligned}\tag{3.7}$$

$$\begin{aligned}\ddot{\mathcal{C}} &= [\mathbf{e}_i] & \ddot{\mathbf{e}}_1 &= \frac{(2\dot{k}^2 - k\ddot{k})\mathbf{r} - 2k\dot{k}\mathbf{v} + k^2\mathbf{a}}{k^3} \\ & & \ddot{\mathbf{e}}_2 &= \ddot{\mathbf{e}}_3 \wedge \mathbf{e}_1 + 2\dot{\mathbf{e}}_3 \wedge \dot{\mathbf{e}}_1 + \mathbf{e}_3 \wedge \ddot{\mathbf{e}}_1 \\ & & \ddot{\mathbf{e}}_3 &= \frac{h^2(\mathbf{v} \wedge \mathbf{a} + \mathbf{r} \wedge \mathbf{j}) - 2\dot{h}h(\mathbf{r} \wedge \mathbf{a}) + (2\dot{h}^2 - h\ddot{h})(\mathbf{r} \wedge \mathbf{v})}{h^3}\end{aligned}\tag{3.8}$$

Let \mathbf{R} be the position of the massless body in the real solar system, with respect to the SSB reference frame. The Lagrangian of the dynamical system is:

$$\mathcal{L}(\mathbf{R}, \dot{\mathbf{R}}, t) = T - V = \frac{1}{2}\dot{\mathbf{R}} \cdot \dot{\mathbf{R}} + \sum_{j \in S} \frac{Gm_j}{\|\mathbf{R} - \mathbf{R}_j\|}\tag{3.9}$$

where G is the universal constant of gravitation, S is the set of all celestial bodies included in the real solar system model, except for the spacecraft itself, and m_j their masses.

For practical reasons it's better to apply the transformation directly on the Lagrangian, rather than on the differential equations stemming from it. However, before applying the transformation, a reference for the time adimensionnalisation shall be specified in such a way that the adimensionalised state vector have components which are at least numerically commensurate. Were the order of magnitude be too separate, the numerical integration to be performed later might suffer from numerical errors or even loose its convergence properties.

The problem of time adimensionalisation will be treated first in general, that is supposing the reference time to be itself a function of time. Later on in the thesis, a much simpler choice will be adopted that will lead to avoid the evaluation of some computationally expensive terms (i.e., the snap of the celestial bodies). The general case will not impede the simplification of some assumptions ‘*a posteriori*’, whereas the opposite is not generally true. The most intuitive function that might represent an adimensional time is the angular velocity of primary and secondary with respect to their centre of mass. Let $\omega \in \mathbb{R}^3$ be the relative angular velocity, $\omega(t) = \|\omega\|$ its euclidean norm and $\tau \in \mathbb{R}^1$ the adimensional time; the time transformation is then:

$$\tau = \omega \cdot (t - t_0) \quad (3.10)$$

The need of computing time derivatives will arise, in such cases the differentiation chain rule shall be exploited to evaluate derivatives in the adimensional variable.

$$\frac{d\sim}{dt} = \dot{\tau} \frac{d\sim}{d\tau} \quad \frac{d^2\sim}{dt^2} = \dot{\tau}^2 \frac{d^2\sim}{d\tau^2} + \ddot{\tau} \frac{d\sim}{d\tau} \quad (3.11)$$

where $\dot{\tau} = \dot{\omega}(t - t_0) + \omega$ and $\ddot{\tau} = \ddot{\omega}(t - t_0) + 2\dot{\omega}$, by simple differentiation of (3.10).

The kinetic energy in the Lagrangian requires the knowledge of the velocity of the spacecraft with respect to the roto-pulsating frame of reference. This is achieved deriving Equation (3.1).

$$\dot{\mathbf{R}} = \dot{\mathbf{b}} + \dot{k}\mathcal{C}\rho + k\dot{\mathcal{C}}\rho + k\mathcal{C}\dot{\rho} \quad (3.12)$$

By means of the chain rule (3.11) and after substitution, the new kinetic and potential energies (functions of the adimensional position, velocity and time), are calculated. The kinetic energy yields:

$$\begin{aligned} T &= \frac{\dot{\tau}^2}{2} (\mathbf{b}' + k'\mathcal{C}\rho + k\mathcal{C}'\rho + k\mathcal{C}\rho')^\top (\mathbf{b}' + k'\mathcal{C}\rho + k\mathcal{C}'\rho + k\mathcal{C}\rho') \\ &= \frac{\dot{\tau}^2}{2} (\mathbf{b}'^\top \mathbf{b}' + k'^2 \rho^\top \rho + k^2 \rho^\top \mathcal{C}'^\top \mathcal{C}' \rho + k^2 \rho'^\top \rho' + 2k' \mathbf{b}'^\top \mathcal{C}\rho \\ &\quad + 2k \mathbf{b}'^\top \mathcal{C}' \rho + 2k \mathbf{b}'^\top \mathcal{C}\rho' + 2kk' \rho^\top \mathcal{C}^\top \mathcal{C}' \rho + 2kk' \rho^\top \rho' \\ &\quad + 2k^2 \rho^\top \mathcal{C}'^\top \mathcal{C}\rho') \end{aligned} \quad (3.13)$$

where primes denote differentiation with respect to τ , and using the orthogonality property of a rotation matrix, $\mathcal{C}^\top \mathcal{C} = \mathcal{I}$, \mathcal{I} being the identity matrix. The potential energy yields:

$$V = - \sum_{j \in S} \frac{\mu_j}{k \|\mathcal{C}(\rho - \rho_j)\|} = \frac{\mu_p + \mu_s}{k} \Omega \quad (3.14)$$

where Ω is the auxiliary potential for the n -body problem at hand, μ_P and μ_S are the mass parameters of the primary and the secondary body, respectively, $\mu_{P,S} = Gm_{P,S}$.

$$\Omega = - \left(\frac{1-\mu}{\|\boldsymbol{\rho} - \boldsymbol{\rho}_P\|} + \frac{\mu}{\|\boldsymbol{\rho} - \boldsymbol{\rho}_S\|} + \sum_{j \in S^*} \frac{\hat{\mu}_j}{\|\boldsymbol{\rho} - \boldsymbol{\rho}_j\|} \right) \quad (3.15)$$

To obtain this result the contributions of the primaries have been separated and highlighted, leaving the other celestial bodies in the collection S^* ; their mass parameters are expressed in a convenient form, $\hat{\mu}_j = m_j / (m_S + m_P)$; and the property that the projection of a vector through an orthonormal matrix is invariant with respect to the euclidean norm operator, has been used. Finally, the Lagrangian of the system can be written as:

$$\mathcal{L}(\boldsymbol{\rho}, \boldsymbol{\rho}', \tau) = T(\boldsymbol{\rho}, \boldsymbol{\rho}', \tau) + \frac{\mu_P + \mu_S}{k} \Omega(\boldsymbol{\rho}, \tau, \{\mu\}_j) \quad (3.16)$$

By means of the Lagrangian formalism and the theorems in the Lagrangian Mechanics, the equations of motion can be written only developing derivatives of complicated terms.

$$\frac{d}{d\tau} \left(\frac{\partial \mathcal{L}}{\partial \boldsymbol{\rho}'^\top} \right) - \frac{\partial \mathcal{L}}{\partial \boldsymbol{\rho}^\top} = \mathbf{Q} = 0 \quad (3.17)$$

The generalised component of the active forces, \mathbf{Q} , is identically zero because there is no other external forces except from the gravitational attraction (i.e., perturbations are neglected in this formulation). The partial derivative needed will be evaluated by terms in the following.

$$\frac{\partial \mathcal{L}}{\partial \boldsymbol{\rho}'^\top} = \frac{\partial T}{\partial \boldsymbol{\rho}'^\top} = \dot{\tau}^2 (k^2 \boldsymbol{\rho}' + k \mathcal{C}^\top \mathbf{b}' + kk' \boldsymbol{\rho} + k^2 \mathcal{C}^\top \mathcal{C}' \boldsymbol{\rho}) \quad (3.18)$$

$$\begin{aligned} \frac{d}{d\tau} \left(\frac{\partial \mathcal{L}}{\partial \boldsymbol{\rho}'^\top} \right) &= \frac{d}{d\tau} \left(\frac{\partial T}{\partial \boldsymbol{\rho}'^\top} \right) = 2\ddot{\tau} (k^2 \boldsymbol{\rho}' + k \mathcal{C}^\top \mathbf{b}' + kk' \boldsymbol{\rho} + k^2 \mathcal{C}^\top \mathcal{C}' \boldsymbol{\rho}) \\ &\quad + \dot{\tau}^2 (2kk' \boldsymbol{\rho}' + k^2 \boldsymbol{\rho}'' + k' \mathcal{C}^\top \mathbf{b}' + k \mathcal{C}'^\top \mathbf{b}' + k \mathcal{C}^\top \mathbf{b}'' \\ &\quad + k'^2 \boldsymbol{\rho} + kk'' \boldsymbol{\rho} + kk' \boldsymbol{\rho}' + 2kk' \mathcal{C}^\top \mathcal{C}' \boldsymbol{\rho} + k^2 \mathcal{C}'^\top \mathcal{C}' \boldsymbol{\rho} \\ &\quad + k^2 \mathcal{C}^\top \mathcal{C}'' \boldsymbol{\rho} + k^2 \mathcal{C}^\top \mathcal{C}' \boldsymbol{\rho}') \end{aligned} \quad (3.19)$$

$$\begin{aligned} \frac{\partial \mathcal{L}}{\partial \boldsymbol{\rho}^\top} &= \dot{\tau}^2 [k'^2 \boldsymbol{\rho} + k^2 \mathcal{C}'^\top \mathcal{C}' \boldsymbol{\rho} + k' \mathcal{C}^\top \mathbf{b}' + k \mathcal{C}'^\top \mathbf{b}' + kk' \underbrace{(\mathcal{C}^\top \mathcal{C}' + \mathcal{C}'^\top \mathcal{C})}_{=\frac{d}{d\tau}(\mathcal{C}^\top \mathcal{C})=0}] \\ &\quad + kk' \boldsymbol{\rho}' + k^2 \mathcal{C}'^\top \mathcal{C}' \boldsymbol{\rho}' + \frac{\mu_P + \mu_S}{k} \nabla \Omega \end{aligned} \quad (3.20)$$

$$\nabla \Omega = \frac{\partial \Omega}{\partial \rho^T} = (1 - \mu) \frac{\rho - \rho_P}{\|\rho - \rho_P\|^3} + \mu \frac{\rho - \rho_S}{\|\rho - \rho_S\|^3} + \sum_{j \in S^*} \hat{\mu}_j \frac{\rho - \rho_j}{\|\rho - \rho_j\|^3} \quad (3.21)$$

Summing and simplifying:

$$\begin{aligned} \rho'' + 2 \left(\frac{\ddot{\tau}}{\dot{\tau}^2} + \frac{k'}{k} + C^T C' \right) \rho' + \left[2 \frac{\ddot{\tau}}{\dot{\tau}^2} \left(\frac{k'}{k} + C^T C' \right) + \frac{k''}{k} \right. \\ \left. + 2 \frac{k'}{k} C^T C' + C^T C'' \right] \rho + 2 \frac{\ddot{\tau}}{\dot{\tau}^2} \frac{1}{k} C^T b' + \frac{1}{k} C^T b'' = \frac{\mu_P + \mu_S}{\dot{\tau}^2 k^3} \nabla \Omega \end{aligned} \quad (3.22)$$

Equations (3.22) represents a system of second order non-linear ODE that can be solved to find the trajectory of the mass particle if the coefficients are known. It is argued that the knowledge of the state of all the celestial bodies at a given epoch, including the primaries, comes from a numerical set, namely the ephemeris. This data respect the n-body gravitational dynamics and the problem is therefore coherent. Hence, the coefficients of the equations are known as function of the real time and nothing can be assumed on how they vary with respect to an arbitrarily chosen adimensional time. For this reason the differentiation chain rule (3.11) shall be used again to express the derivative of the coefficients in terms of real time functions. The mathematical steps result in:

$$\begin{aligned} \rho'' = -\frac{2}{\dot{\tau}} \left[\left(\frac{\ddot{\tau}}{\dot{\tau}} + \frac{\dot{k}}{k} \right) \mathcal{I} + C^T \dot{C} \right] \rho' - \frac{1}{\dot{\tau}^2} \left\{ \left[\left(\frac{\ddot{\tau}}{\dot{\tau} k} + \frac{\ddot{k}}{k} \right) \mathcal{I} + \left(\frac{\ddot{\tau}}{\dot{\tau}} + 2 \frac{\dot{k}}{k} \right) C^T \dot{C} \right. \right. \\ \left. \left. + C^T \ddot{C} \right] \rho + \frac{1}{k} \left(\frac{\ddot{\tau}}{\dot{\tau}} C^T b + C^T \ddot{b} \right) \right\} + \frac{\mu_P + \mu_S}{\dot{\tau}^2 k^3} \left[(1 - \mu) \frac{\rho - \rho_P}{\|\rho - \rho_P\|^3} \right. \\ \left. + \mu \frac{\rho - \rho_S}{\|\rho - \rho_S\|^3} + \sum_{j \in S^*} \hat{\mu}_j \frac{\rho - \rho_j}{\|\rho - \rho_j\|^3} \right] \end{aligned} \quad (3.23)$$

The system of second order differential equations (3.23) governs the dynamics of a massless particle in the real solar system gravitational model. Once initial conditions are provided, the solution exists and is unique for the differential calculus theorem. It can be put in the mathematically convenient state space form, obtaining the following first order differential equation:

$$\mathbf{x}' = \mathbf{f}(\tau, \mathbf{x}) \quad (3.24)$$

where

$$\mathbf{x} = \begin{pmatrix} \rho \\ \rho' \end{pmatrix} \quad \mathbf{f}(\tau, \mathbf{x}) = \begin{pmatrix} \rho' \\ \rho''(3.23) \end{pmatrix}$$

Looking at the coefficients of the equation in detail would give a great insight on the dynamics of the system, and provides the instruments to make some assumptions and simplifications. Note that the coefficients of ρ and ρ' depend mainly on:

1. the matrices $\mathcal{C}^T \dot{\mathcal{C}}$ and $\mathcal{C}^T \ddot{\mathcal{C}}$;
2. the ratios $\frac{k}{\tau}$ and $\frac{\dot{k}}{k}$;
3. the ratio $\frac{\ddot{\tau}}{\tau}$.

PROPERTIES OF $\mathcal{C}^T \dot{\mathcal{C}}$ Since \mathcal{C} is a cosine angle matrix, then it is orthonormal.

$$\frac{d}{dt}(\mathcal{C}^T \mathcal{C}) = \dot{\mathcal{C}}^T \mathcal{C} + \mathcal{C}^T \dot{\mathcal{C}} = 0 \Rightarrow \dot{\mathcal{C}}^T \mathcal{C} = -(\dot{\mathcal{C}}^T \mathcal{C})^T \quad (3.25)$$

The matrix $\mathcal{C}^T \dot{\mathcal{C}}$ is *skew-symmetric* so that $\mathbf{e}_i \cdot \dot{\mathbf{e}}_j = -\mathbf{e}_j \cdot \dot{\mathbf{e}}_i$.

$$\mathcal{C}^T \dot{\mathcal{C}} = \begin{bmatrix} \mathbf{e}_1^T \\ \mathbf{e}_2^T \\ \mathbf{e}_3^T \end{bmatrix} \begin{bmatrix} \dot{\mathbf{e}}_1 & \dot{\mathbf{e}}_2 & \dot{\mathbf{e}}_3 \end{bmatrix} = \begin{bmatrix} 0 & -\mathbf{e}_2 \cdot \dot{\mathbf{e}}_1 & -\mathbf{e}_3 \cdot \dot{\mathbf{e}}_1 \\ \mathbf{e}_2 \cdot \dot{\mathbf{e}}_1 & 0 & -\mathbf{e}_3 \cdot \dot{\mathbf{e}}_2 \\ \mathbf{e}_3 \cdot \dot{\mathbf{e}}_1 & \mathbf{e}_3 \cdot \dot{\mathbf{e}}_2 & 0 \end{bmatrix}$$

$$\begin{aligned} \mathbf{e}_2 \cdot \dot{\mathbf{e}}_1 &= \frac{h}{k^2} \\ \mathbf{e}_3 \cdot \dot{\mathbf{e}}_1 &= 0 \\ \mathbf{e}_3 \cdot \dot{\mathbf{e}}_2 &= \frac{k}{h} \mathbf{a} \cdot \mathbf{e}_3 \end{aligned}$$

The mathematical steps necessary to calculate the scalar products are quite cumbersome. The reader is remanded to Appendix A to see the rigorous evaluation of these terms. Finally:

$$\boxed{\mathcal{C}^T \dot{\mathcal{C}} = \begin{bmatrix} 0 & -\frac{h}{k^2} & 0 \\ \frac{h}{k^2} & 0 & -\frac{k}{h^2} \mathbf{a} \cdot (\mathbf{r} \wedge \mathbf{v}) \\ 0 & \frac{k}{h^2} \mathbf{a} \cdot (\mathbf{r} \wedge \mathbf{v}) & 0 \end{bmatrix}} \quad (3.26)$$

PROPERTIES OF $\mathcal{C}^T \ddot{\mathcal{C}}$

$$\begin{aligned} \mathcal{C}^T \ddot{\mathcal{C}} &= \frac{d}{dt}(\mathcal{C}^T \dot{\mathcal{C}}) - \dot{\mathcal{C}}^T \dot{\mathcal{C}} & \mathcal{C}^T \ddot{\mathcal{C}} + \ddot{\mathcal{C}}^T \mathcal{C} = -2\dot{\mathcal{C}}^T \dot{\mathcal{C}} \\ \ddot{\mathcal{C}}^T \mathcal{C} &= \frac{d}{dt}(\dot{\mathcal{C}}^T \mathcal{C}) - \dot{\mathcal{C}}^T \dot{\mathcal{C}} & \Rightarrow \mathcal{C}^T \ddot{\mathcal{C}} - \ddot{\mathcal{C}}^T \mathcal{C} = 2 \frac{d}{dt}(\mathcal{C}^T \dot{\mathcal{C}}) \end{aligned} \quad (3.27)$$

Clearly $\dot{\mathcal{C}}^T \ddot{\mathcal{C}}$ is the sum of the skew-symmetric matrix $\frac{d}{dt}(\mathcal{C}^T \dot{\mathcal{C}})$ and the symmetric matrix $\dot{\mathcal{C}}^T \dot{\mathcal{C}}$. Let's evaluate the components of the square velocity cosine angle matrix.

$$\dot{\mathcal{C}}^T \dot{\mathcal{C}} = \begin{bmatrix} \dot{\mathbf{e}}_1^T \\ \dot{\mathbf{e}}_2^T \\ \dot{\mathbf{e}}_3^T \end{bmatrix} \begin{bmatrix} \dot{\mathbf{e}}_1 & \dot{\mathbf{e}}_2 & \dot{\mathbf{e}}_3 \end{bmatrix} = \begin{bmatrix} \dot{\mathbf{e}}_1 \cdot \dot{\mathbf{e}}_1 & & \\ \dot{\mathbf{e}}_2 \cdot \dot{\mathbf{e}}_1 & \dot{\mathbf{e}}_2 \cdot \dot{\mathbf{e}}_2 & \\ \dot{\mathbf{e}}_3 \cdot \dot{\mathbf{e}}_1 & \dot{\mathbf{e}}_3 \cdot \dot{\mathbf{e}}_2 & \dot{\mathbf{e}}_3 \cdot \dot{\mathbf{e}}_3 \end{bmatrix}$$

$$\begin{aligned} \dot{\mathbf{e}}_1 \cdot \dot{\mathbf{e}}_1 &= \left(\frac{h}{k^2} \right)^2 & \dot{\mathbf{e}}_2 \cdot \dot{\mathbf{e}}_1 &= 0 \\ \dot{\mathbf{e}}_2 \cdot \dot{\mathbf{e}}_2 &= \dot{\mathbf{e}}_1^2 + \dot{\mathbf{e}}_3^2 & \dot{\mathbf{e}}_3 \cdot \dot{\mathbf{e}}_1 &= -\frac{1}{k} \mathbf{a} \cdot \mathbf{e}_3 \\ \dot{\mathbf{e}}_3 \cdot \dot{\mathbf{e}}_3 &= \frac{\|(\mathbf{r} \wedge \mathbf{v}) \wedge (\mathbf{r} \wedge \mathbf{a})\|^2}{h^4} & \dot{\mathbf{e}}_3 \cdot \dot{\mathbf{e}}_2 &= 0 \end{aligned}$$

Again, the mathematical steps necessary to calculate the scalar products are quite cumbersome. The reader is remanded to Appendix A to see the rigorous evaluation of these terms.

$$\boxed{\begin{aligned} \mathcal{C}^T \ddot{\mathcal{C}} &= \frac{d}{dt} \begin{bmatrix} 0 & -\frac{h}{k^2} & 0 \\ \frac{h}{k^2} & 0 & -\frac{k}{h} \mathbf{a} \cdot \mathbf{e}_3 \\ 0 & \frac{k}{h} \mathbf{a} \cdot \mathbf{e}_3 & 0 \end{bmatrix} \\ &- \begin{bmatrix} \left(\frac{h}{k^2} \right)^2 & 0 & -\frac{1}{k} \mathbf{a} \cdot \mathbf{e}_3 \\ 0 & \left(\frac{h}{k^2} \right)^2 + \frac{\|(\mathbf{r} \wedge \mathbf{v}) \wedge (\mathbf{r} \wedge \mathbf{a})\|^2}{h^4} & 0 \\ -\frac{1}{k} \mathbf{a} \cdot \mathbf{e}_3 & 0 & \frac{\|(\mathbf{r} \wedge \mathbf{v}) \wedge (\mathbf{r} \wedge \mathbf{a})\|^2}{h^4} \end{bmatrix} \end{aligned}} \quad (3.28)$$

Some interesting properties are deduced:

$$\mathbf{e}_i \cdot \ddot{\mathbf{e}}_i = -\dot{\mathbf{e}}_i \cdot \dot{\mathbf{e}}_i \quad \forall i \quad \mathbf{e}_i \cdot \ddot{\mathbf{e}}_j = \begin{cases} -\mathbf{e}_j \cdot \ddot{\mathbf{e}}_i & i = (1) \quad j = (2) \\ \mathbf{e}_j \cdot \ddot{\mathbf{e}}_i = \dot{\mathbf{e}}_j \cdot \dot{\mathbf{e}}_i & i = 1 \quad j = 3 \end{cases}$$

To complete the derivation of $\dot{\mathcal{C}}^T \ddot{\mathcal{C}}$, the time derivative of $\dot{\mathcal{C}}^T \dot{\mathcal{C}}$ is needed:

$$\begin{aligned} \frac{d}{dt} \left(\frac{h}{k^2} \right) &= \frac{\dot{h}k - 2\dot{k}h}{k^3} \\ \frac{d}{dt} \left(\frac{k}{h} \mathbf{a} \cdot \mathbf{e}_3 \right) &= \left(\frac{\dot{k}h - 2k\dot{h}}{h^2} \mathbf{a} + \frac{k}{h} \mathbf{j} \right) \cdot \mathbf{e}_3 \end{aligned}$$

Note that the need to evaluate the relative overacceleration, known in mechanics as jerk \mathbf{j} , arises in order to completely define the coefficients of the equations of motion. This quantity is directly derived from the Newton Universal Gravitation Formula, equation (2.2), by time differentiation.

$$\mathbf{J} = \sum_{j \in S} \frac{\mu_j}{\|\mathbf{R}_j - \mathbf{R}\|^5} [\|\mathbf{R}_j - \mathbf{R}\|^2 (\mathbf{V}_j - \mathbf{V}) - 3[(\mathbf{R}_j - \mathbf{R}) \cdot (\mathbf{V}_j - \mathbf{V})](\mathbf{R}_j - \mathbf{R})] \quad (3.29)$$

THE RATIO $\frac{\ddot{\tau}}{\dot{\tau}}$ The adimensional time τ , along with its first and second time derivatives, are important parameters that influence the coefficients of the motion equations. With the choice made at the beginning of this chapter the ratio reads:

$$\frac{\ddot{\tau}}{\dot{\tau}} = \frac{\ddot{\omega}(t - t_0) + 2\dot{\omega}}{\dot{\omega}(t - t_0) + \omega} \quad (3.30)$$

From some simple considerations on three-dimensional rotations (see Stuelpnagel [42] for a detailed treatment), the angular velocity can be calculated solely from the knowledge of the cosine matrix. In particular, the angular velocity is the one at which the new vector triad, roto-pulsating reference, rotates with respect to the solar system barycentric frame, an inertial one for the assumptions made so far. For the case at hand, since the new triad is aligned with the primaries direction, it represents also the relative angular velocity between the primary and secondary bodies. Differentiating the orthogonality relation, valid for every well-defined direction cosine matrix, yields:

$$\frac{d}{dt}(\mathcal{C}\mathcal{C}^T) = \dot{\mathcal{C}}\mathcal{C}^T + \mathcal{C}\dot{\mathcal{C}}^T = 0 \quad (3.31)$$

It's evident that the matrix $\dot{\mathcal{C}}\mathcal{C}^T$ is skew-symmetric, hence three parameters are enough to completely determine it. The components of the angular velocity vector can be expressed in terms of these parameters.

$$\boldsymbol{\omega}_X = \dot{\mathcal{C}}\mathcal{C}^T = \begin{bmatrix} 0 & -\omega_3 & \omega_2 \\ \omega_3 & 0 & -\omega_1 \\ -\omega_2 & \omega_1 & 0 \end{bmatrix} \quad (3.32)$$

The symbol $(\cdot)_X$ is here used to indicate a skew symmetric tensor, whose components are expressed with respect to the initial reference frame. The notation reminds the fact that a skew symmetric matrix can be used for computing the

components of the cross product between two vectors. Another interesting property, directly stemming from (3.31), is that ω_X serves also as state transition matrix for the dynamics of the direction cosine matrix, that is $\dot{\mathcal{C}} = \omega_X \mathcal{C}$.

In this thesis the matrix ω_X has been calculated numerically, since it does not seem to have any particular simplified analytical form. The successive time derivatives are calculated as follows:

$$\ddot{\omega}_X = \ddot{\mathcal{C}}\mathcal{C}^T + \dot{\mathcal{C}}\dot{\mathcal{C}}^T \quad \ddot{\omega}_X = \frac{d\ddot{\mathcal{C}}}{dt}\mathcal{C}^T + 2\ddot{\mathcal{C}}\dot{\mathcal{C}}^T + \dot{\mathcal{C}}\ddot{\mathcal{C}}^T$$

As for the angular velocity, the angular acceleration $\dot{\omega}$ and the angular jerk $\ddot{\omega}$ are evaluated from the corresponding skew symmetric tensor. The adimensionalisation function then results from an euclidean norm, so as its derivatives.

$$\omega = \|\omega\| \tag{3.33}$$

$$\dot{\omega} = \frac{\omega \cdot \dot{\omega}}{\omega} \tag{3.34}$$

$$\ddot{\omega} = \frac{\omega(\|\dot{\omega}\|^2 + \omega \cdot \ddot{\omega}) + \dot{\omega}(\omega \cdot \dot{\omega})}{\omega^2} \tag{3.35}$$

In these relations the third time derivative of the direction cosine matrix appears. Reminding that the second time-derivative of one term of this tensor depends directly on the relative jerk, (3.28), it's quite straightforward to expect the third time-derivative to depend on the relative snap, $s(t)$. Proceeding in this way, not only the mathematical steps necessary to complete the adimensionalisation are unwieldy, and for this reason liable to errors; but also the numerical computation greatly suffers in term of efficiency and speed. Another probable source of error is the order of magnitude of such terms, that can be significantly smaller than the acceleration terms and can be dangerously near the epsilon-machine. The results of such calculations are given without proof.

$$\begin{aligned} \ddot{k} &= \frac{1}{k^3} [k^2(3\mathbf{v} \cdot \mathbf{a} + \mathbf{r} \cdot \mathbf{j}) + (2\dot{k}^2 - k\ddot{k})\mathbf{r} \cdot \mathbf{v} - 2k\dot{k}(\mathbf{v}^2 + \mathbf{r} \cdot \mathbf{a})] \\ \ddot{h} &= \frac{1}{h^3} \{ [3h^2(\mathbf{r} \wedge \mathbf{a}) - 2h\dot{h}(\mathbf{r} \wedge \mathbf{v})] \cdot [(\mathbf{v} \wedge \mathbf{a}) + (\mathbf{r} \wedge \mathbf{j})] + h^2(\mathbf{r} \wedge \mathbf{v}) \cdot [2(\mathbf{v} \wedge \mathbf{j}) \\ &\quad + (\mathbf{r} \wedge \mathbf{s})] + (2\dot{h}^2 - 2h\ddot{h})[(\mathbf{r} \wedge \mathbf{v}) \cdot (\mathbf{r} \wedge \mathbf{a})] - 2h\dot{h}(\mathbf{r} \wedge \mathbf{a})^2 \} \end{aligned}$$

The snap of the k-th body yields:

$$\begin{aligned} \mathbf{s}_k = \sum_{j \in S} \frac{\mu_j}{\|\mathbf{R}_j - \mathbf{R}_k\|^7} & \left(-6\|\mathbf{R}_j - \mathbf{R}_k\|^2 [(\mathbf{R}_j - \mathbf{R}_k) \cdot (\mathbf{V}_j - \mathbf{V}_k)] (\mathbf{V}_j - \mathbf{V}_k) \right. \\ & + 3\{5[(\mathbf{R}_j - \mathbf{R}_k) \cdot (\mathbf{V}_j - \mathbf{V}_k)]^2 - \|\mathbf{R}_j - \mathbf{R}_k\|^2 [(\mathbf{V}_j - \mathbf{V}_k)^2 \right. \\ & \left. \left. - (\mathbf{R}_j - \mathbf{R}_k) \cdot (\mathbf{A}_j - \mathbf{A}_k)]\}(\mathbf{R}_j - \mathbf{R}_k) + \|\mathbf{R}_j - \mathbf{R}_k\|^4 (\mathbf{A}_j - \mathbf{A}_k) \right) \end{aligned} \quad (3.36)$$

The columns of the $\ddot{\mathcal{C}} = [\ddot{\mathbf{e}}_i]$ result in:

$$\begin{aligned} \ddot{\mathbf{e}}_1 &= \frac{1}{k^4} [(6kk\ddot{k} - k^2\ddot{k} - 6k^3)\mathbf{r} + 3k(2\dot{k}^2 - k\ddot{k})\mathbf{v} - 3k^2\dot{k}\mathbf{a} + k^3\mathbf{j}] \\ \ddot{\mathbf{e}}_2 &= \ddot{\mathbf{e}}_3 \wedge \mathbf{e}_1 + 3\ddot{\mathbf{e}}_3 \wedge \dot{\mathbf{e}}_1 + 3\dot{\mathbf{e}}_3 \wedge \ddot{\mathbf{e}}_1 + \mathbf{e}_3 \wedge \ddot{\mathbf{e}}_1 \\ \ddot{\mathbf{e}}_3 &= \frac{1}{h^4} [-3h^2\dot{h}(\mathbf{v} \wedge \mathbf{a} + \mathbf{r} \wedge \mathbf{j}) + 3h(2\dot{h}^2 - h\ddot{h})(\mathbf{r} \wedge \mathbf{a}) \\ &+ (6h\dot{h}\ddot{h} - h^2\ddot{h} - 6h^3)(\mathbf{r} \wedge \mathbf{v}) + h^3(2\mathbf{v} \wedge \mathbf{j} + \mathbf{r} \wedge \mathbf{s})] \end{aligned}$$

3.2 COEFFICIENTS FOR THE EQUATIONS OF MOTION

At this point all the needed elements to well-define Equation (3.23) are known, either numerically or analytically. This equation might be written per components, to emphasise its strong similarity with the Equation (2.33), describing the dynamics of the much simpler restricted three-body problem. Let's look at each scalar component of the vectorial equation (3.23), namely along directions x, y, z , respectively.

$$x'' = b_1 + b_4x' + b_5y' + b_7x + b_9y + b_8z + b_{13}\Omega_x \quad (3.37a)$$

$$y'' = b_2 - b_5x' + b_4y' + b_6z' - b_9x + b_{10}y + b_{11}z + b_{13}\Omega_y \quad (3.37b)$$

$$z'' = b_3 - b_6y' + b_4z' + b_8x - b_{11}y + b_{12}z + b_{13}\Omega_z \quad (3.37c)$$

where:

$$\begin{aligned} b_1 &= -\frac{1}{k\dot{\tau}^2} \left(\frac{\ddot{\tau}}{\dot{\tau}} \dot{\mathbf{b}} + \ddot{\mathbf{b}} \right) \cdot \mathbf{e}_1 & b_2 &= -\frac{1}{k\dot{\tau}^2} \left(\frac{\ddot{\tau}}{\dot{\tau}} \dot{\mathbf{b}} + \ddot{\mathbf{b}} \right) \cdot \mathbf{e}_2 \\ b_3 &= -\frac{1}{k\dot{\tau}^2} \left(\frac{\ddot{\tau}}{\dot{\tau}} \dot{\mathbf{b}} + \ddot{\mathbf{b}} \right) \cdot \mathbf{e}_3 & b_4 &= -\frac{2}{\dot{\tau}} \left(\frac{\ddot{\tau}}{\dot{\tau}} + \frac{\dot{k}}{k} \right) \\ b_5 &= \frac{2}{\dot{\tau}} \mathbf{e}_2 \cdot \dot{\mathbf{e}}_1 & b_6 &= \frac{2}{\dot{\tau}} \mathbf{e}_3 \cdot \dot{\mathbf{e}}_2 \\ b_7 &= -\frac{1}{\dot{\tau}^2} \left[\left(\frac{\ddot{\tau}}{\dot{\tau}} \frac{\dot{k}}{k} + \frac{\dot{k}}{k} \right) - \dot{\mathbf{e}}_1 \cdot \dot{\mathbf{e}}_1 \right] & b_8 &= \frac{1}{\dot{\tau}^2} \dot{\mathbf{e}}_1 \cdot \dot{\mathbf{e}}_3 \end{aligned}$$

$$\begin{aligned} b_9 &= \frac{1}{\dot{\tau}^2} \left[\left(\frac{\ddot{\tau}}{\dot{\tau}} + 2 \frac{\dot{k}}{k} \right) \mathbf{e}_2 \cdot \dot{\mathbf{e}}_1 + \mathbf{e}_2 \cdot \ddot{\mathbf{e}}_1 \right] & b_{10} &= -\frac{1}{\dot{\tau}^2} \left[\left(\frac{\ddot{\tau}}{\dot{\tau}} \frac{k}{\dot{k}} + \frac{\ddot{k}}{k} \right) - \dot{\mathbf{e}}_2 \cdot \dot{\mathbf{e}}_2 \right] \\ b_{11} &= \frac{1}{\dot{\tau}^2} \left[\left(\frac{\ddot{\tau}}{\dot{\tau}} + 2 \frac{\dot{k}}{k} \right) \mathbf{e}_3 \cdot \dot{\mathbf{e}}_2 + \mathbf{e}_3 \cdot \ddot{\mathbf{e}}_2 \right] & b_{12} &= -\frac{1}{\dot{\tau}^2} \left[\left(\frac{\ddot{\tau}}{\dot{\tau}} \frac{k}{\dot{k}} + \frac{\ddot{k}}{k} \right) - \dot{\mathbf{e}}_3 \cdot \dot{\mathbf{e}}_3 \right] \\ b_{13} &= \frac{\mu_s + \mu_p}{k^3 \dot{\tau}^2} \end{aligned}$$

where $\Omega_{x,y,z}$ are the components of the gradient of the auxiliary potential of the real n-body problem, Equation (3.21).

If a constant time reference is chosen for the adimensionalisation, the equations of motion greatly simplify. An example would be, for instance, choosing ω such that the average primaries revolution period is 2π . In this case the function reduces to the mean motion of the primaries, n . The equations yield:

$$\tau = n \cdot (t - t_0) \quad n = \frac{2\pi}{T} = \sqrt{\frac{G(m_p + m_s)}{\bar{a}^3}} \quad (3.38)$$

where \bar{a} is the mean distance between the primaries for a long time interval, a period of 400 years will suffice. It should be remarked that the mean distance between primaries is not exactly the semi-major axis of the ellipse described by their orbits, the eccentricity modifies it by a factor $\sqrt{1 - e^2}$. This small error won't anyway affect the generality of the problem because it's limited to the time adimensionalisation, for which a very general and arbitrary function may be chosen without affecting the real dynamics of the particle investigated. According to Gómez [22], a problem of coherence might appear². This incoherence derives from the arbitrary selection of the adimensional time, that is not compatible with the RTBP. In this thesis no such issue has been encountered. This should not surprise, since the adimensionalisation must not change the dynamical properties of the system nor its response, and merely serves as a comparative tool and numerical trick that allows a reduction to a simpler and perhaps more familiar form of the mathematical problem. Thanks to this assumption the time derivatives of τ become:

$$\dot{\tau} = n \quad \ddot{\tau} = 0$$

² The general adimensionalisation of time has been treated generally, convinced that a fundamental coherence problem could have arose when adimensionalising with respect to a quantity whose actual physical importance loses significance outside the Kepler problem. Successively, in the integration steps it became clear such an issue would not arise and would not pose any threat to the generality of the dynamical problem at hand.

Equation (3.23), and therefore its coefficients, assumes a much more convenient form.

$$\begin{aligned}\rho'' = & -\frac{2}{n} \left(\frac{\dot{k}}{k} \mathcal{J} + \mathcal{C}^T \dot{\mathcal{C}} \right) \rho' - \frac{1}{n^2} \left[\left(\frac{\ddot{k}}{k} \mathcal{J} + 2 \frac{\dot{k}}{k} \mathcal{C}^T \dot{\mathcal{C}} + \mathcal{C}^T \ddot{\mathcal{C}} \right) \rho \right. \\ & \left. + \frac{1}{k} \mathcal{C}^T \ddot{\mathbf{b}} \right] + \frac{\mu_P + \mu_S}{n^2 k^3} \left[(1 - \mu) \frac{\rho - \rho_P}{\|\rho - \rho_P\|^3} + \mu \frac{\rho - \rho_S}{\|\rho - \rho_S\|^3} \right. \\ & \left. + \sum_{j \in S^*} \hat{\mu}_j \frac{\rho - \rho_j}{\|\rho - \rho_j\|^3} \right]\end{aligned}\quad (3.39)$$

and the coefficients of the equivalent component equations (3.37) read:

$$\begin{aligned}b_1 &= -\frac{\ddot{\mathbf{b}} \cdot \mathbf{e}_1}{kn^2} & b_2 &= -\frac{\ddot{\mathbf{b}} \cdot \mathbf{e}_2}{kn^2} & b_3 &= -\frac{\ddot{\mathbf{b}} \cdot \mathbf{e}_3}{kn^2} \\ b_4 &= -\frac{2}{n} \frac{\dot{k}}{k} & b_5 &= \frac{2}{n} \mathbf{e}_2 \cdot \dot{\mathbf{e}}_1 & b_6 &= \frac{2}{n} \mathbf{e}_3 \cdot \dot{\mathbf{e}}_2 \\ b_7 &= -\frac{1}{n^2} \left(\frac{\ddot{k}}{k} - \dot{\mathbf{e}}_1 \cdot \dot{\mathbf{e}}_1 \right) & b_8 &= \frac{1}{n^2} \dot{\mathbf{e}}_1 \cdot \dot{\mathbf{e}}_3 \\ b_9 &= \frac{1}{n^2} \left(2 \frac{\dot{k}}{k} \mathbf{e}_2 \cdot \dot{\mathbf{e}}_1 + \mathbf{e}_2 \cdot \ddot{\mathbf{e}}_1 \right) & b_{10} &= -\frac{1}{n^2} \left(\frac{\ddot{k}}{k} - \dot{\mathbf{e}}_2 \cdot \dot{\mathbf{e}}_2 \right) \\ b_{11} &= \frac{1}{n^2} \left(2 \frac{\dot{k}}{k} \mathbf{e}_3 \cdot \dot{\mathbf{e}}_2 + \mathbf{e}_3 \cdot \ddot{\mathbf{e}}_2 \right) & b_{12} &= -\frac{1}{n^2} \left(\frac{\ddot{k}}{k} - \dot{\mathbf{e}}_3 \cdot \dot{\mathbf{e}}_3 \right) & b_{13} &= \frac{\mu_S + \mu_P}{k^3 n^2}\end{aligned}$$

These are the equations used throughout this thesis for numerical integration and techniques.

3.3 FOURIER ANALYSIS OF THE MOTION EQUATIONS' COEFFICIENTS

This section is devoted to the results of a Fourier analysis applied to the time-dependent functions in Eq. (3.37): the motion coefficients b_i , $i = 1, \dots, 13$, and the coordinates of some bodies in the solar system. Please refer to Chapter B in the Appendix for an introduction to Fourier analysis. The case of constant adimensional time is considered. In particular, three main synodic systems are studied: Earth-Moon, Sun-Earth and Sun-Jupiter. Lastly, the scalar components of the Sun and Mercury position vectors will be analysed as well, by means of the Fourier transform.

The objective is to assess some useful information on the harmonic content of the dynamics. In this regard, it is expected to find several peaks in the Fourier transform that correspond first to the roto-pulsating main frequency, and secondly to the largest perturbations which affects the synodic dynamics, e.g. the Sun for the Earth-Moon case and Jupiter for the Sun-Earth case.

The coefficients of motion are calculated numerically for a long time interval by means of the relations shown in the previous section, and the planets'

positions are extrapolated from the ephemeris through the method explained in Chapter 4. As for any Fourier procedure, the most relevant parameters to be specified are the size, T_0 , of the sampling interval, and the number, N , of equally spaced sampling points within such interval. These parameters define the Nyquist critical frequency, $f_N = \frac{N}{2T_0}$, that fixes the window within which the frequencies (true or aliased) will be found. The minimum number of samples has been chosen such that the Fourier analysis can detect frequencies at least equal to $1, \frac{N_{\min}}{2T_0} = 1$. Moreover, the sampling period T_0 should be large enough to allow for both being able to resolve a minimum frequency, proportional to $\frac{1}{T_0}$, and at the same time to let the solar system completely exhaust its dynamics. A period larger than 250 years suffice the purpose³. What is more, the number of samples chosen has been selected as a power of two; due to requirements of the Fast Fourier Transform (commonly known as FFT) algorithm in Matlab®, used to carry out the transforms in a fast and efficient way.

As far as the Earth-Moon system is concerned, the coefficients span an interval of 359.1 years with $N = 2^{18}$ samples, which results in a time rate of 12 hours; on the other hand, the Sun- systems coefficients are sampled with $N = 2^{19}$ with a time rate of 12 hours, providing a totality of roughly 718.2 years. The positions of the planets are calculated with the same sampling strategy for the Sun- systems motion coefficients.

Finally, in order to reduce the leakage, the functions to be transformed are truncated by means of a Hanning window function of order 2:

$$H_{T_0}(t) = \frac{2}{3} \left(1 - \cos \frac{2\pi t}{T_0}\right)^2 \quad (3.40)$$

Tables 3.1, 3.2 and 3.3 provide the values for frequencies and amplitudes where known perturbations occur, for the Earth-Moon, Sun-Earth and Sun-Jupiter case, respectively. The responsible for the peaks in the Fourier transform have been identified univocally and with scarce effort. To each system 3 figures are dedicated: the first two figures display 12 of the coefficients of motion, while the remaining one is a zoom on the smallest harmonics. In this image the peaks are highlighted. Since the harmonic content of these coefficients is in general very rich, all the figures have been given a double y-axis with different scale in order to allow for a more readily comprehension and comparison.

As expected, the majority of the perturbative contributions appear in the Fourier transform of some coefficients. Note, however, that not all the coefficients feel the same perturbative effects. For example, considering the Earth-Moon case, coefficients b_1 , b_3 and b_5 show a completely different harmonic trend. This effect is even more stressed in the position components of Mercury.

³ Note that Pluto has an orbital period of roughly 247 years.

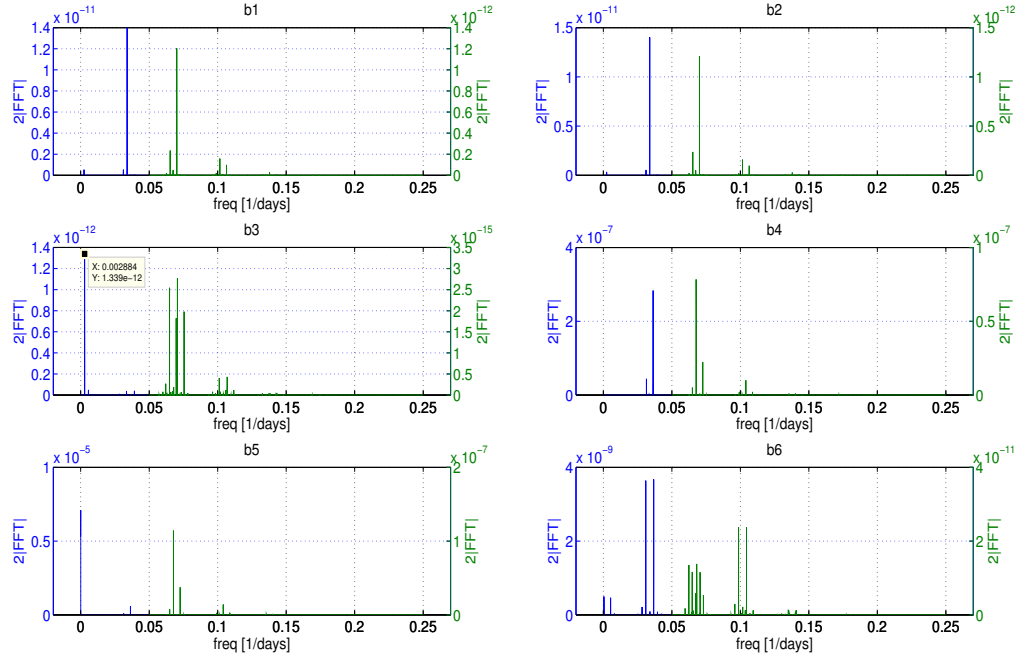


Figure 3.2: Norm of Fourier transform of the motion equation ($b_i, i = 1, \dots, 6$) coefficients for the Earth-Moon case

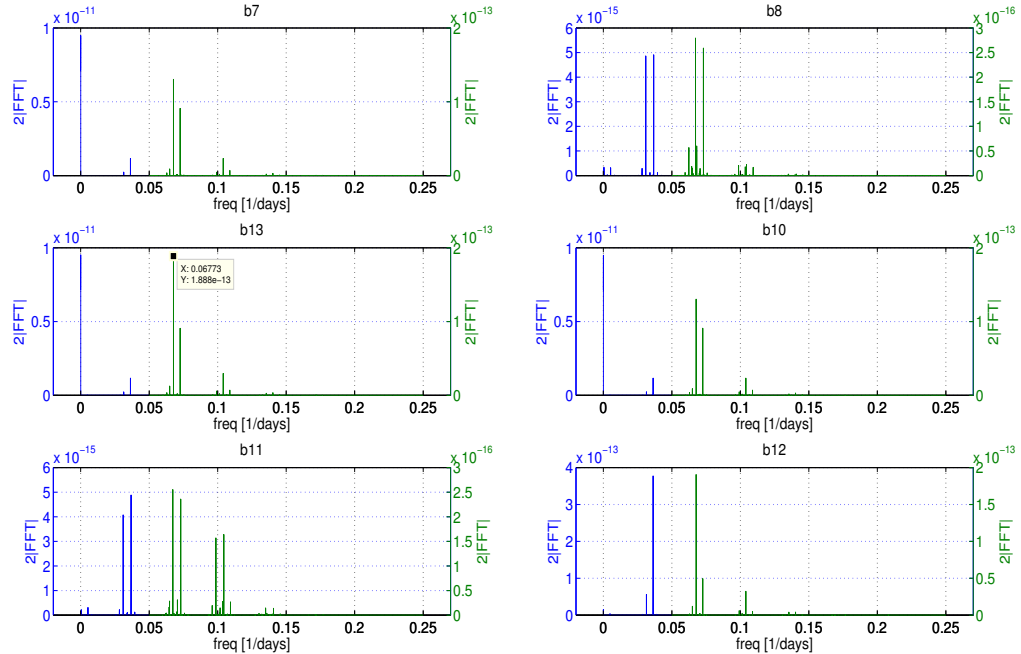


Figure 3.3: Norm of Fourier transform of the motion equation ($b_i, i = 7, \dots, 13$ excluding b_9) coefficients for the Earth-Moon case

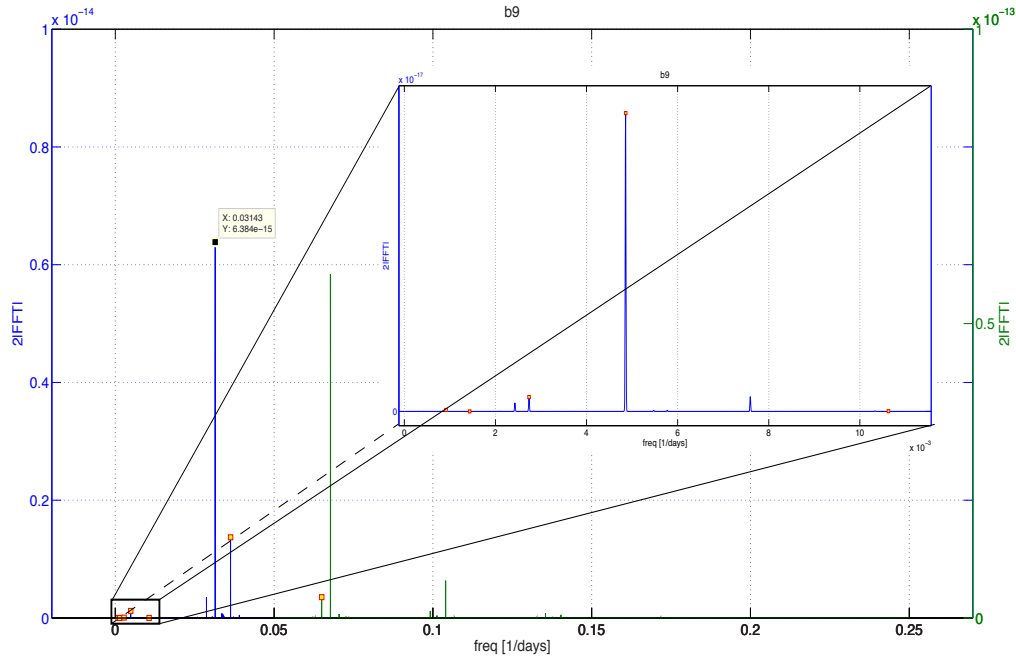


Figure 3.4: Norm of Fourier transform of the motion equation coefficients b_9 for the Earth-Moon case

Table 3.1: Earth-Moon

Frequency [$\frac{1}{\text{days}}$]	Amplitude []	Celestial body
0.031433345286143	6.384211216030891e-15	Sun
0.00143433711499874	1.22632140863049e-21	Jupiter
0.0106278276659215	1.10362980806164e-19	Mars
0.000915534328722601	5.85307939512853e-19	Earth
0.00273897353342845	5.83598723519726e-18	Venus
0.00485996139496914	1.20955568679729e-16	Mercury
0.0362933066811118	1.37056514267241e-15	Moon
0.0649876784338259	3.53829308430899e-15	Titan

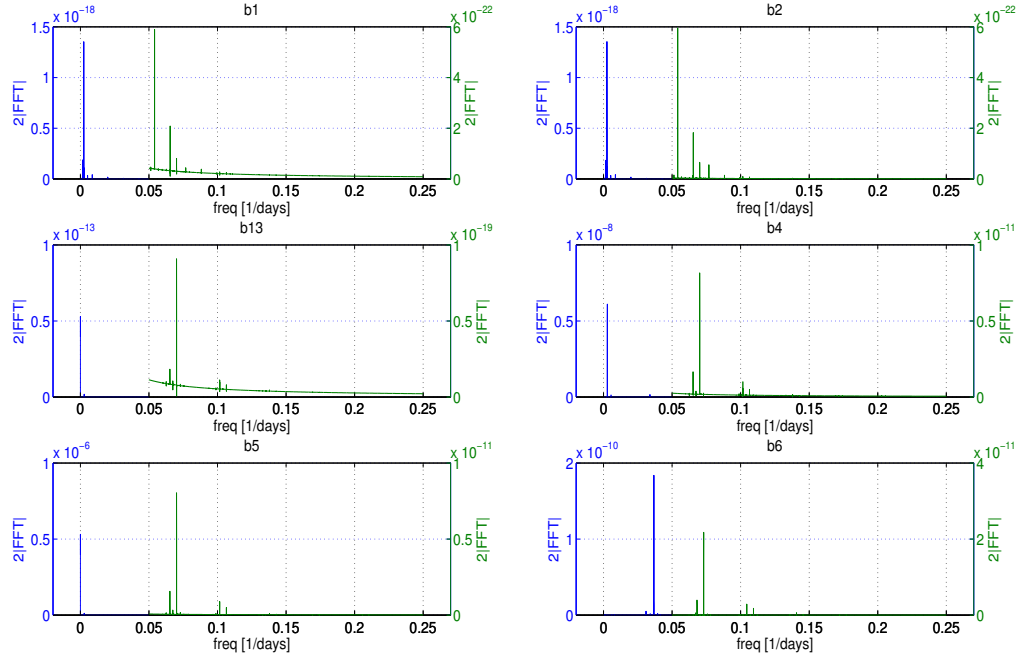


Figure 3.5: Norm of Fourier transform of the motion equation ($b_i, i = 1, \dots, 6, 13$ excluding b_3) coefficients for the Sun-Earth case

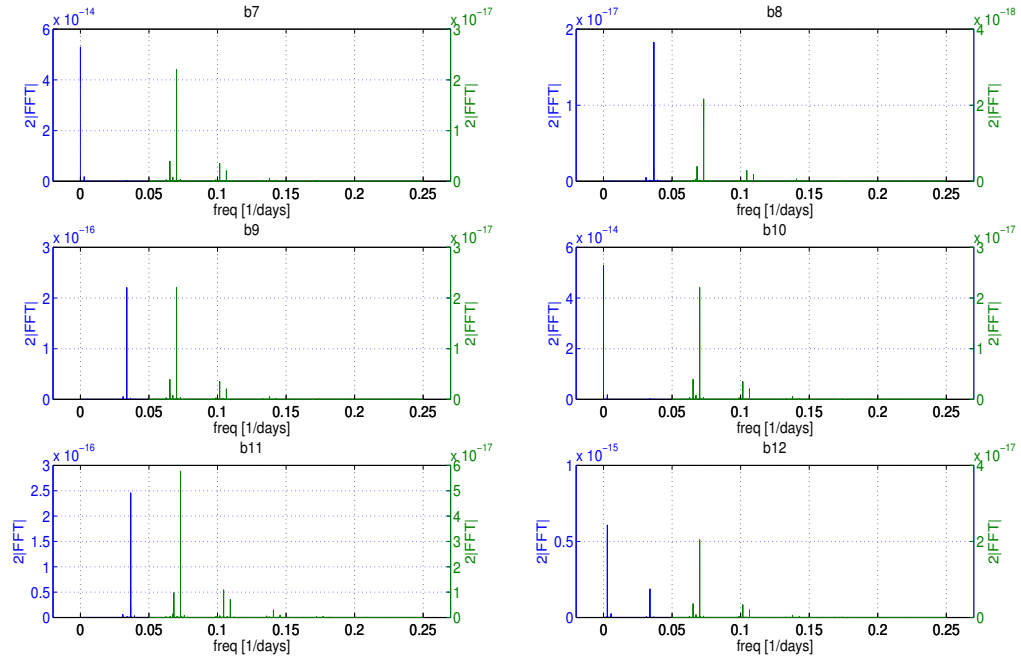


Figure 3.6: Norm of Fourier transform of the motion equation ($b_i, i = 7, \dots, 12$) coefficients for the Sun-Earth case

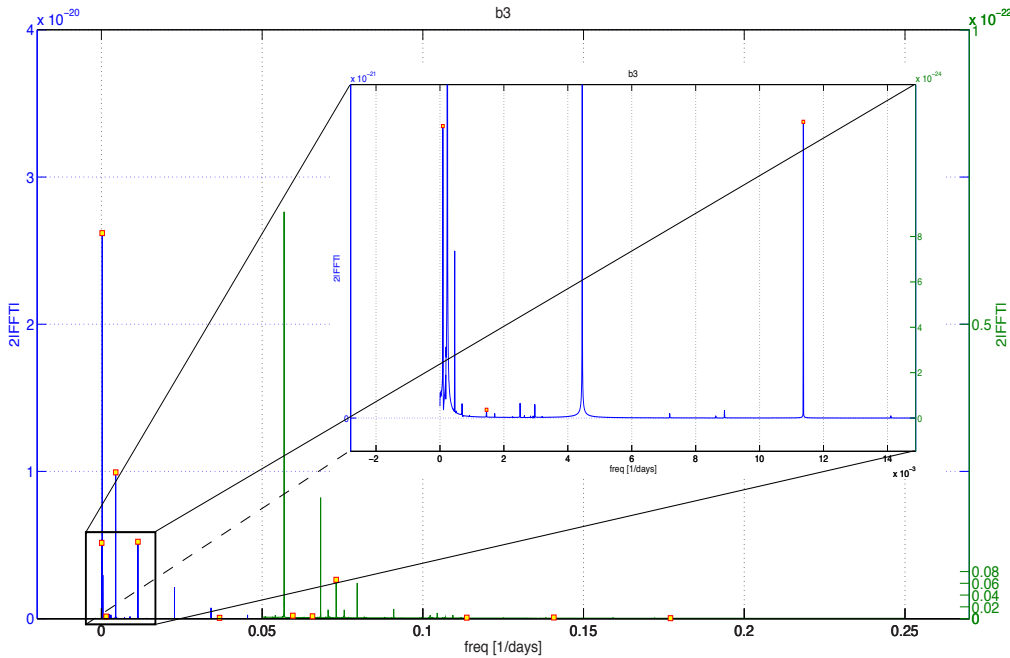


Figure 3.7: Norm of Fourier transform of the motion equation coefficients b_3 for the Sun-Earth case

Table 3.2: Sun-Earth

Frequency [$\frac{1}{\text{days}}$]	Amplitude []	Celestial body
0.177052219590071	7.32793078806584e-26	Saturn
0.113670782740718	1.66915982935052e-25	Jupiter
0.140766680781100	1.99422711488481e-25	Mars
0.0656740786517283	4.06299327643241e-25	Venus
0.0595705397435751	4.98245736370823e-25	Mercury
0.0730402871715056	6.60255000200197e-24	Moon
0.0367471189388998	5.50145646597360e-23	Callisto
0.00145721991432157	1.45580075579785e-22	Titan
9.15530836222978e-05	5.14743145492597e-21	Oberon
0.0113678412164353	5.22275852100833e-21	Titania
0.00445176869113423	9.93488270346316e-21	Ganymede
0.000232697420873340	2.61881409265997e-20	Triton

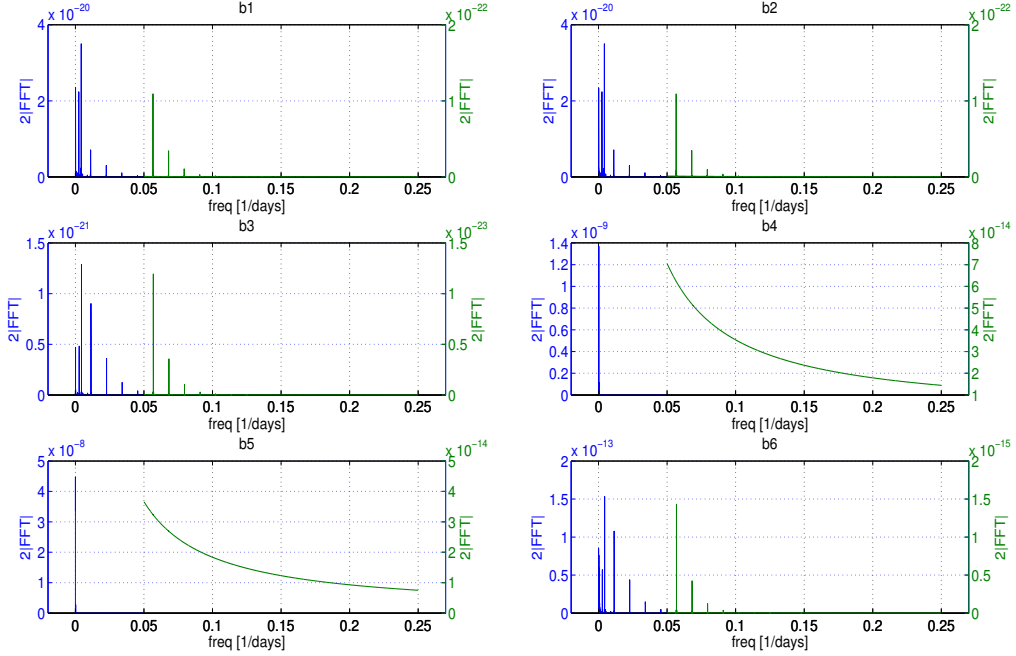


Figure 3.8: Norm of Fourier transform of the motion equation ($b_i, i = 1, \dots, 6$) coefficients for the Sun-Jupiter case

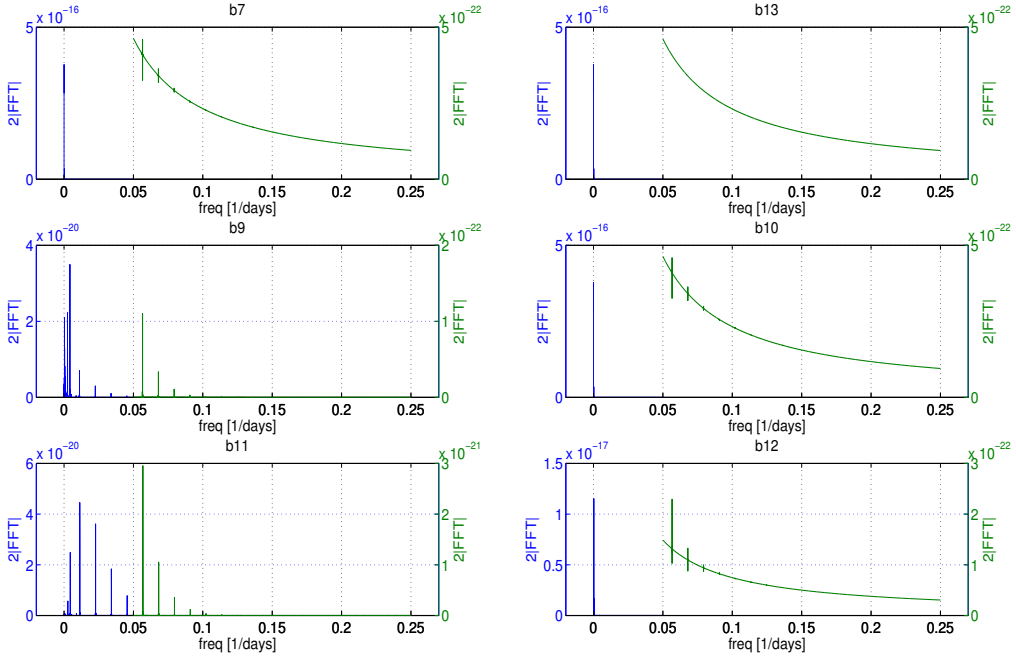


Figure 3.9: Norm of Fourier transform of the motion equation ($b_i, i = 7, \dots, 13$ excluding b_8) coefficients for the Sun-Jupiter case

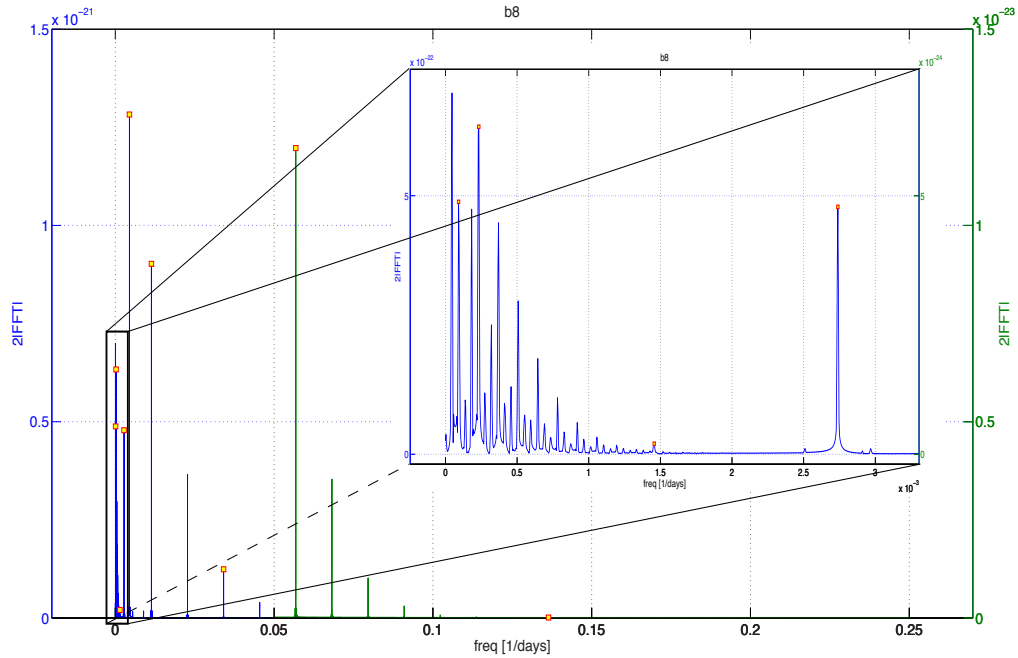


Figure 3.10: Norm of Fourier transform of the motion equation coefficients b_8 for the Sun-Jupiter case

Table 3.3: Sun-Jupiter

Frequency [$\frac{1}{\text{days}}$]	Amplitude []	Celestial body
0.136410279885406	1.20415331995905e-26	Saturn
0.0568392060821765	1.19722955622913e-23	Jupiter
0.00145721991432157	2.05525357673021e-23	Mars
0.0341035236493059	1.24042063770490e-22	Earth
0.00273896308503374	4.78359321188790e-22	Venus
9.15530836222978e-05	4.88163572189429e-22	Mercury
0.000232697420873340	6.33277098190491e-22	Moon
0.0113678412164353	9.02354691209728e-22	Callisto
0.00445176869113423	1.28260684220962e-21	Ganymede

As far as the Earth-Moon system is concerned the perturbation with highest Fourier transform magnitude has period of 32 days roughly; this contribution is conjectured to be caused by the Sun.

One unexpected, but quite reassuring, result is that some coefficients (see Figures 3.10 and 3.7 for example) exhibit contributions due to celestial bodies orbiting with period between 3.5 and 5.5 years. Such orbital period range is characteristic of the many main-belt asteroids, between the orbits of Jupiter and Mars. It is quite extraordinary that, relatively small celestial objects (if compared to planets) may yet have a minimum influence on the dynamics of the roto-pulsating system. One could argue that these small celestial bodies are not contemplated in the model used so far. However, these contributions might be introduced by to the planets states, calculated very precisely and comprehensively by JPL.

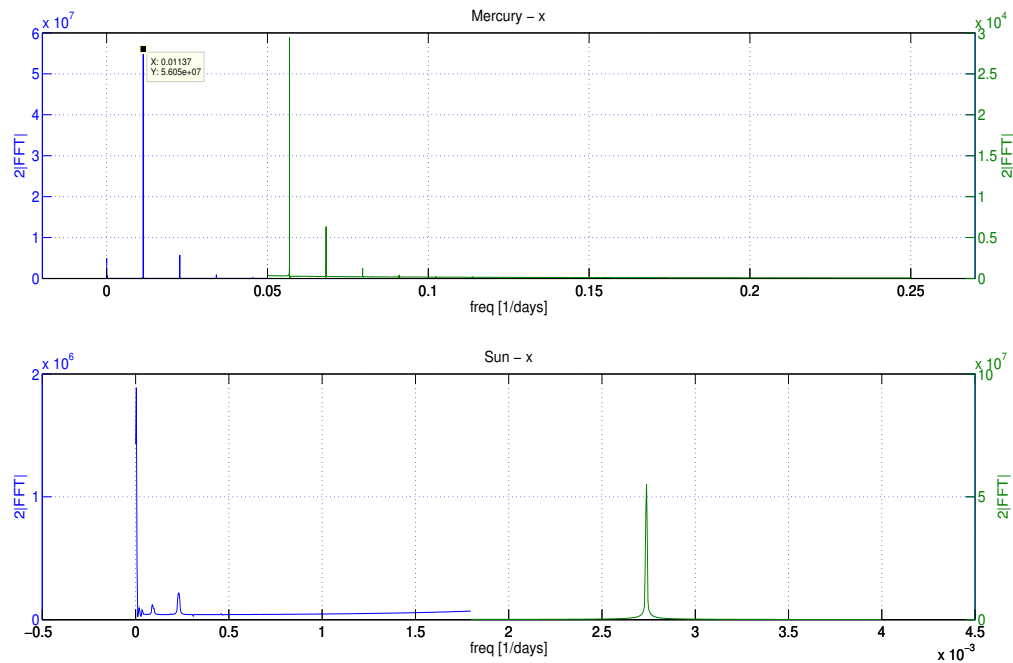


Figure 3.11: Norm of Fourier transform of the x components of the Sun (bottom) and Mercury (top). The positions are expressed in Kilometres and are written in the inertial frame of reference, centred at SSB

Lastly, Figure 3.11 displays the x position components, written in the SSB reference frame, of Mercury and the Sun. As far as the Sun is concerned, it is clear that its orbit about the solar system barycenter is strongly perturbed by Jupiter ‘in primis’ and, after that, by Saturn, Neptune (clearly visible on the left) and by the Earth (the green peak on the right). Indeed, the orbit of the Sun has been demonstrated in other researches to be wobbled mainly because of these perturbers. On the other hand, the harmonic portrait of Mercury is of course dominated by its own orbital period, highlighted in the top-most subfigure;

anyway other smaller contributions are evident, mainly due to Jupiter and the Moon. The highest contribution in the reduced green-scale occurs at 17 days and it could be ascribable to Callisto, which possesses the same orbital period around Jupiter. However, due to their huge relative distance, the cause of this effect is not taken as sure in this thesis.

4

INTEGRATION AND VALIDATION

In this chapter the integration strategy is presented, both in terms of selection of numerical model and of computational efficiency. The choice of the adimensionalisation factors for the SSB trajectory and the type of solver used are discussed highlighting advantages and trade-offs of the numerical schemes available. The JPL¹ ephemeris model is briefly addressed as source for the celestial bodies states. *HORIZONS*, a web tool built and constantly being updated by the JPL, serves as benchmark for the validation of the integrations that are carried out in this work, both in the solar system barycenter and in the roto-pulsating frame of reference.

4.1 INTEGRATION SCHEME

The topic of numerical integration is vast and well treated in literature, not to mention its rapid development with the increase of machines computational power. Here, a brief introduction to numerical integration techniques for ordinary differential equations is addressed, special attention will be given to the methods concerning the most with Astrodynamics.

Initial value problems for initial condition propagation, both forward and backward in time, occupy perhaps the most important place. Classical methods that guarantee high accuracy, vast stability region and satisfactory efficiency for this problem are the linear multi-step methods. On the other hand, Astrodynamics often deals with two-point boundary value problems, whose solution is sought here by means of shooting techniques.

Numerical schemes can be classified into two large categories: *single-step methods* and *multi-step methods*. In the first case a typical step is determined solely from the value of an adjacent node, whereas in the multi-step case the

¹ The Jet Propulsion Laboratory, or JPL, is a federally funded research and development centre and NASA field centre located in La Cañada Flintridge, California, United States. JPL is managed by the nearby California Institute of Technology (Caltech) for the National Aeronautics and Space Administration. The laboratory's primary function is the construction and operation of robotic planetary spacecraft, though it also conducts Earth-orbit and astronomy missions. It is also responsible for operating NASA's Deep Space Network.

computation of the actual solution requires the knowledge of the function at several nodes.

Another important classification splits the numerical integrators into *implicit methods* and *explicit methods*. Explicit methods calculate the state of a system at a later time from the state of the system at the current time, while implicit methods find a solution by solving an equation involving both the current state of the system and the later one. Mathematically, if $x(t)$ is the current system state and $x(t + \Delta t)$ is the state at the later time, with Δt a small time step, then, the equation to be solved is explicit or implicit in the unknown $x(t + \Delta t)$.

$$\begin{array}{ll} x(t + \Delta t) = f(x(t)) & \text{explicit method} \\ g(x(t), x(t + \Delta t)) = 0 & \text{implicit method} \end{array}$$

The initial value problem for which a numerical solution is sought, has the form of (3.24), that can be stated scalarly as:

$$\begin{aligned} \dot{x} &= f(t, x) \quad t \in [t_i, t_f] \\ x(t_i) &= x_0 \end{aligned} \tag{4.1}$$

The techniques presented below can be easily extended for set of differential equations; however, for the sake of simplicity, the equations will be developed in the one-dimensional case. Numerical methods for solving (4.1) will generally find an approximate solution for $x(t)$ at a discrete set of nodes $t_i = t_0 < t_1 \dots < t_N = t_f$. Again for simplicity, the analysis will be restricted to the evenly h-spaced time interval, such that

$$t_k = t_0 + kh \quad k = 0, 1, \dots, N$$

The approximate solution will be indicated as $\eta(t)$. Notations for the approximate solution at the node points is $\eta(t_k) = \eta_k$. To obtain an approximate solution at points in the interval $[t_i, t_f]$ other than those selected in the nodal splitting process, some form of interpolation must be used (i. e., cubic spline).

The central concepts in the analysis of any numerical method for differential equations, are *convergence*, *order*, and *stability*. These properties won't be thoroughly analysed in this work, detailed proof will be omitted and simple results will instead be stated. Briefly, convergence deals with the tendency of the approximate solution towards the exact solution as the time step goes to zero. The order of the method depends on the local truncation error (the error committed by one step) behaviour as h tends to zero. Finally the stability focuses on the consequences of perturbations in the method starting values.

4.1.1 Multi-step methods

According to Stoer and Bulirsch [40], in a multistep method for the solution of the initial value problem (4.1), one computes an approximate value η_{j+r} of $x(t_{j+r})$ from $r \geq 2$, given approximate values η_k of $x(t_k)$ at equidistant points. In general, a multistep method, as well as a single step one, might be written in the following form:

$$\eta_{j+r} + a_{r-1}\eta_{j+r-1} + \cdots + a_0\eta_j = hF(t_j; \eta_{j+r}, \eta_{j+r-1}, \dots, \eta_j; h; f) \quad j = 0, 1, \dots \quad (4.2)$$

A multistep method as (4.2) is called an *r-step method*. Note that the function F can depend linearly on its variables, one then speaks of a linear r-step method. This class entails the majority of the methods that are actually used in numerical computation and codes.

In order to initiate such methods, it is of course necessary that r starting values $\eta_0, \eta_1, \dots, \eta_{r-1}$ be at disposal. Any of these initial values define a unique sequence $\eta_j, j \geq 0$, that approximates the ordinary differential equation solution in the equidistant nodes specified by h . The seed values for the multistep method can be obtained by means of other numerical methods, e.g. appropriate one-step methods. It's important to underline that, if one wants to preserve the global order of the multistep method, the starting values must be computed with the aid of a method possessing at least equal truncation error behaviour; were not this the case, the order of the whole technique, combination of the two methods, might be reduced.

From simple calculus theory an integration of Equation (4.1) in a definite time interval yields:

$$x(t_{p+k}) - x(t_{p-j}) = \int_{t_{p-j}}^{t_{p+k}} f(t, x(t)) dt \quad (4.3)$$

The trick is to replace the integrand function by a suitable interpolating polynomial $P_q(t)$ such that:

1. $\deg(P_q) \leq q$
2. $P_q(t_k) = f(t_k, x_k) \quad k = p, p-1, \dots, p-q$

A common choice is the use of the Lagrange interpolation polynomials, that might be analytically expressed by the formula:

$$P_q(t) = \sum_{i=0}^q f(t_{p-i}, x_{p-i}) L_i(t) \quad L_i(t) = \prod_{\substack{l=0 \\ l \neq i}}^q \frac{t - t_{p-l}}{t_{p-i} - t_{p-l}} \quad (4.4)$$

The definite integral becomes:

$$x(t_{p+k}) - x(t_{p-j}) \approx \sum_{i=0}^q f(t_{p-i}, x_{p-i}) \int_{t_{p-j}}^{t_{p+k}} L_i(t) dt$$

Replacing the x_i by the approximate values η_i and dropping the inequality sign (the global truncation error is supposed to be null at this stage):

$$\eta(t_{p+k}) = \eta(t_{p-j}) + h \sum_{i=0}^q \beta_{qi} f_{p-i} \quad f_l = f(t_l, \eta_l) \quad (4.5)$$

where the multistep method coefficients β_{qi} can be readily calculated.

$$\beta_{qi} = \frac{1}{h} \int_{t_{p-j}}^{t_{p+k}} L_i(t) dt = \int_{-j}^k \prod_{\substack{l=0 \\ l \neq i}}^q \frac{s+l}{l-i} ds \quad i = 0, 1, \dots, q \quad (4.6)$$

The result has been achieved by means of the substitution $x = t_0 + (p+s)h$ and remembering that the time step h is constant. At this point different values for k, j and q result in different multistep methods. Among the most commonly used are the *Adams-Bashforth method* and the *Adams-Moulton method*.

ADAMS-BASHFORTH METHOD The Adams-Bashforth method of order q is obtained when the values $k = 1$ and $j = 0$ are used.

$$\eta_{p+1} = \eta_p + h \sum_{i=0}^q \beta_{qi} f_{p-i} \quad (4.7a)$$

$$\beta_{qi} = \int_0^1 \prod_{\substack{l=0 \\ l \neq i}}^q \frac{s+l}{l-i} ds \quad i = 0, 1, \dots, q \quad (4.7b)$$

This is an explicit method since Equation (4.7a) can be directly solved to find the solution value at the next node, η_{p+1} . Table 4.1 shows some numerical values of β_{qi} . It can be demonstrated that this method is of order $r = q + 1$, so that the local truncation error, T , decades as

$$\lim_{h \rightarrow 0} T_{p+1}(t) = O(h^{q+2})$$

Table 4.1: Adams-Bashforth coefficients

β_{qi}	i				
	0	1	2	3	4
β_{0i}	1				
$2\beta_{1i}$	3	-1			
$12\beta_{2i}$	23	-16	5		
$24\beta_{3i}$	55	-59	37	-9	
$720\beta_{4i}$	1901	-2774	2616	-1274	251

ADAMS-MOULTON METHOD The Adams-Moulton method of order q is obtained when the values $k = 0$ and $j = 1$ are used.

$$\eta_{p+1} = \eta_p + h \sum_{i=0}^q \beta_{qi} f_{p+1-i} \quad (4.8a)$$

$$\beta_{qi} = \int_{-1}^0 \prod_{\substack{l=0 \\ l \neq i}}^q \frac{s+l}{l-i} ds \quad i = 0, 1, \dots, q \quad (4.8b)$$

Table 4.2 shows some numerical values of β_{qi} . It can be demonstrated that this method is of order $r+1 = q+1$, so that the local truncation error decays as

$$\lim_{h \rightarrow 0} T_{p+1}(t) = O(h^{q+2})$$

It's clear at this point that the Admas-Moulton method is implicit, Equation (4.8a) represents indeed a nonlinear constraint for η_{p+1} . An iterative method shall be exploited in order to find numerically the solution, for which an initial guess must be provided. A possible iterative scheme that accomplishes the task suggests itself quite naturally:

$$\eta_{p+1}^{(n+1)} = \eta_p + h [\beta_{q0} f(t_{p+1}, \eta_{p+1}^{(n)}) + \sum_{i=1}^q \beta_{qi} f_{p+1-i}] \quad (4.9)$$

For given $\eta_p, \eta_{p-1}, \dots, \eta_{p+1-q}$ a good initial guess $\eta_{p+1}^{(0)}$ for the proposed iteration can be found with the aid of another explicit method, e.g. the Adams-Bashforth method.

For this reason, one also calls explicit methods like the Adams-Bashforth method *predictor methods*, and implicit methods like the Adams-Moulton method *corrector methods*; through the iteration (4.9) one then corrects η_{p+1} .

Table 4.2: Adams-Moulton coefficients

β_{qi}	i				
	0	1	2	3	4
β_{0i}	1				
$2\beta_{1i}$	1	1			
$12\beta_{2i}$	5	8	-1		
$24\beta_{3i}$	9	19	-5	1	
$720\beta_{4i}$	251	646	-264	106	-19

In this work the propagation of initial conditions, that is the solution of initial value problems, has been accomplished with the aid of the Matlab® suite *ode113* (see Shampine and Reichelt [37]). This function implements a variable order, adaptive step Adams-Bashforth-Moulton method in a PECE mode (predict, evaluate, correct, evaluate). The ABM method uses the explicit Adams-Bashforth method to predict the approximate value of the solution at the next nodes, and the implicit Adams-Mouton method to correct these values. The variable order and the adaptive step assure the respect of the tolerances the user selects and improves the efficiency of the code. The seed values needed to initialise the method are automatically calculated by means of a proper order Runge-Kutta method, briefly addressed in Section 4.1.2. Its order is chosen as to maintain the truncation error tendency of the whole numerical scheme.

4.1.2 Runge-Kutta methods

The Runge-Kutta method is a very popular one-step method that evaluates the force function $f(t, x)$ at several, shrewdly chosen, points in order to calculate the approximate solution x_{k+1} from the sole knowledge of the adjacent node value x_k . To avoid the need for higher-order derivatives, as in the well-known Taylor methods, the Runge-Kutta methods evaluate $f(t, x)$ at more points, while attempting to retain the accuracy of the Taylor expansion series (see Süli and Mayers [43]). The methods obtained are fairly easy to program.

Let s be the order of the numerical scheme and t_k the actual time among an equidistant set of nodes $t_k = t_0 + kh$, separated by the constant span h . The s -order Runge-Kutta method can be formulated as follows:

$$z_i = x_k + h \sum_{j=1}^{i-1} \beta_{ij} f(t_k + \alpha_j h, z_j) \quad i = 1, \dots, s \quad (4.10a)$$

Table 4.3: Butcher table

0					
α_2	β_{21}				
α_3	β_{31}	β_{32}			
\vdots	\vdots	\ddots			
α_s	β_{s1}	β_{s2}	\dots	$\beta_{s,s-1}$	
	c_1	c_2	\dots	c_{s-1}	c_s

Table 4.4: Butcher table for a 4th order RK

0					
0.5	0.5				
0.5	0	0.5			
1	0	0	1		
	1/6	1/3	1/3	1/6	

$$x_{k+1} = x_k + h \sum_{j=1}^s c_j f(t_n + \alpha_j h, z_j) \quad (4.10b)$$

The constants β_{ij} , α_j and c_j are determined so that when the true solution $x(t)$ is substituted in the approximate equation (4.10b) the truncation error will satisfy:

$$T_{k+1}(x) = O(h^{s+1})$$

A typical form to present the required coefficients is the *Butcher table*, Table 4.3. The coefficients of a 4th order Runge-Kutta method are shown in Table 4.4. In order to find the equations for the constants, a common approach is to use Taylor expansions retaining the error on the calculations. Another possibility is to use higher order RK scheme to estimate the local error in the lower order scheme, procedure exploited in the *Fehlberg methods*.

The Matlab® suite *ode45* uses a Runge-Kutta-Fehlberg of this kind, the function is integrated with a 4-th order RK method and the error is checked with a 5-th order's. The adaptive step is implemented so as to satisfy the required tolerances. The function *ode78*, courtesy of Govorukhin V. N., applies the same strategy with RK methods of order 7 ad 8, respectively.

4.2 THE JPL EPHEMERIS MODEL

Ephemeris, the greek word that means diary or calendar, is a highly accurate record of the states of the main celestial bodies with significant mass of the solar system, that is the Sun, the planets, proto- and dwarfplanets, natural satellites and minor bodies such as asteroids and comets. These state vectors come from precise observations at several sites on Earth, observations from artificial satellites, and from an accurate time-integration which takes into account a large variety of phenomena that can affect the dynamical model.

Ephemeris data provided by the Jet Propulsion Laboratory are at present the standard reference for high-precision planetary, stellar and lunar coordinates used in high-fidelity simulations and in actual space missions design. There exists a large variety of JPL ephemeris and they are classified by type, accuracy and time span. In the course of the years, observations accuracy and numerical analysis have become better and better along with the compelling request and need for accurate positions and velocity in order to obtain low-cost, low-energy trajectories for space missions. The latest JPL ephemerides with fully consistent treatment of planetary and lunar laser ranging data is DE430 (Folkner et al. [14]). The dynamical model for DE430 includes a frictional damping between the fluid core and the elastic mantle of some celestial bodies. However, this damping term is not suitable for extrapolation more than several centuries into the past. In order to cover a longer time span, the ephemeris DE431 was integrated without the lunar core/mantle damping term.

The JPL planetary ephemerides are saved as files of Chebyshev polynomials fit to the Cartesian positions and velocities of the planets, Sun, and Moon, typically in 32-day intervals. Most JPL planetary ephemeris files include Chebyshev polynomials fit to the lunar libration angles, which are integrated along with the planetary positions. Many ephemeris files also fit to the 1980 IAU nutation series. The positions are integrated in astronomical units (AU), but with polynomials stored in units of kilometers. The integration time units are days of barycentric dynamical time (TDB). Prior to DE430, the value of the astronomical unit was estimated from measurements of planetary orbits using the Gaussian gravitational constant. Starting with DE430, the astronomical units has been fixed to the value 149597870.700 km as adopted by the International Astronomical Union in 2012. This value is the standard value used throughout this thesis.

In compliance with Standish [39], in order to produce an ephemeris, observational data (optical, VLBI, radar and spacecraft) containing measurement errors are combined with dynamical models containing modelling imprecisions. A best fit is developed to statistically minimise those errors. The resulting ephemeris has an associated uncertainty that fluctuates with time. Uncertainties in major planet ephemerides range from 10 cm to more than 100 km in the state-of-the-art JPL/DE-405 ephemeris, used as the basis for spacecraft navigation, mission planning and radar astronomy. Cartesian state vectors are output in all their 16 decimal-place glory. This does not mean all digits are physically meaningful. The full-precision may be of interest to those studying the ephemerides or as a source of initial conditions for subsequent integrations, as they're used here. On top of this basic uncertainty, the mass parameter used to compute osculating element output is rarely known to better than 5 significant figures. Small-body elements are reported in the optical frame (i.e., FK5/J2000.0). This frame is currently thought to differ by no more than 0.01 arcseconds from the ICRF of the planetary ephemeris DE-405. Until a gener-

ally agreed upon transformation from one frame to the other is defined and implemented, they will be treated as being the same.

The Earth is assumed to be a rigid body and solid Earth tides affecting station location are not included. Of course, precession and nutation effects are included, as is polar motion. CT-TAI terms less than 20 μ sec are omitted. These and other Earth-model approximations result in topocentric station location errors, with respect to the reference ellipsoid, of less than 20 meters. However, many optical site positions (latitude and longitude) are reported far less accurately and can be many kilometres off.

Solar relativistic effects are included in all planet, lunar and small body dynamics, excluding satellites. Relativity is included in observables via 2nd order terms in stellar aberration and the deflection of light due to gravity fields of the Sun (and Earth, for topocentric observers). Deflections due to other gravity fields can potentially have an effect at the 1e-4 arcsec level, but are not currently included here. Satellites of other planets, such as Jupiter's, could experience deflections at the 1e-3 arcsec level as well. Light time iterations are Newtonian. This affects light-time convergence at the millisecond level and position at 1e-6 arcsec level.

Spacecraft in low Earth orbit (i. e., ISS, HST, Swift, GALEX and so on) need frequent updates to maintain high accuracy. LEO predicts more than a few days into the future can have tens or hundreds of Km of error.

Among the many ephemeris files available, the DE-405 and the latest DE-430 have been used as main models throughout this work.

- (i) DE405: created in May, 1997; it includes both nutations and librations. It covers JED 2305424.50 (1599 December 09) to JED 2525008.50 (2201 February 20), in total almost 602 years.
- (ii) DE430: created in April, 2013; it includes librations and 1980 nutation series. It covers the time span from JED 2287184.5 (1549 December 21) to JED 2688976.5 (2650 January 25) for a rough total of 1101 years and is at present the reference to the International Celestial Reference Frame version 2.0.

The JPL planetary and lunar ephemerides are available to the general public via a secure ftp server on the NASA and JPL ports. For LINUX-based systems, as the one we used for all the main calculations in the thesis (MacBookPro 2.9 Ghz Intel Core i7 8 Gb RAM, two 1.6 GHz DDR3 memory modules), the ephemeris are given as 20-years ascii blocks that must be converted to binary files before the interpolation and reading are applied. For this procedure a tool, provided by E.M. Standish, running on Matlab® has been used. It essentially converts the ascii file to a more computer-friendly binary format on which the extrapolation of the data is done. The input are a header containing the main

information on the ephemeris used (e.g. DE405 or DE430) and the ascii file itself. The epoch in Julian days are specified and the program interpolates, by means of the Chebyshev polynomials recursive formula, the state vectors of the main celestial bodies (9 planets, Sun and Moon).

$$\begin{aligned} T_{i+1}(x) &= 2xT_i(x) - T_{i-1}(x) \\ T'_{i+1}(x) &= 2(T_i(x) + xT'_i(x)) - T'_{i-1}(x) \end{aligned}$$

where the starting values are $T_0(x) = 1$ and $T_1(x) = x$. A GUI is available and makes all the procedure easy to implement and understand.

For the purposes of this thesis, a more self-extracting and automatic procedure was sought. In this optic the program has been lightly modified, and at last even make faster and less interactive. The source code gives the possibility to do a test to a more accurate pre-downloaded dataset. Running several tests for large time spans (several centuries) it has been realised the errors don't seem to have a regular structure, but rather vary randomly with time, always being bounded by 10^{-14} . The only results that showed errors larger than the expected values were the lunar librations and nutations; these values won't be used as initial guess for an integration procedure.

The JPL ephemeris records provide very precise coordinates, in a solar system barycenter frame, for the following 13 items:

- | | |
|--------------------------|---------------------|
| 1. Mercury | 8. Neptune |
| 2. Venus | 9. Pluto |
| 3. Earth-Moon barycenter | 10. Geocentric Moon |
| 4. Mars | 11. Sun |
| 5. Jupiter | 12. Nutations |
| 6. Saturn | 13. Librations |
| 7. Uranus | |

Of course an algorithm has been developed that allows the centre of the state vectors to shift according to will. Care must be exercised when using the information on Earth and Moon given by this ephemeris file. The state vector of the Moon is given as relative to the Earth, which has to be calculated. Simple geometrical considerations lead to the state vectors expressed in the solar system barycenter frame. Let $\mu_{rat} = 81.300569074190619$ be the mass ratio between the Earth and the Moon, then

$$\mathbf{r}_E = \mathbf{r}_{CG} - \frac{\mathbf{r}_M^{rel}}{1 + \mu_{rat}} \quad (4.11)$$

$$\mathbf{r}_M = \mathbf{r}_E + \mathbf{r}_M^{rel} \quad (4.12)$$

In order to validate the results of the integration, the need for other celestial bodies state vectors arise. This is accomplished by means of the free web-interface *HORIZONS*, compiled by the JPL group and based on the latest and most accurate model of the DE430. The website tool can be found at <http://ssd.jpl.nasa.gov/horizons.cgi>. Its interface accepts several inputs, among the most important are:

- 1. Ephemeris type: vector table, observer table or orbital elements
- 2. Target body;
- 3. Observer location;
- 4. Time span;
- 5. Table settings: a set of options can be specified here, time format and measure and reference system for instance;
- 6. Output/Display.

In this work, the vectors ephemeris table is used, which generates a cartesian state vector table of any object (target body) with respect to any major body (observer location). The time span might be either given in normal Gregorian calendar days or in Julian days. The reference units used are Km and seconds, in any case readily transformed into astronomical units and days by simple arithmetic operations. The reference plane is the standard ICRF/J2000.0 and the coordinate system refers to the Earth mean equator and the equinox at the reference epoch. Other options are not relevant for the purposes of this thesis.

4.2.1 Julian days count

It's clear that as the complexity of the astrodynamics problem increases, e. g. with the increased number of accounted celestial bodies, the dynamical system describing the phenomenon becomes nonautonomous. Hence, the need for a convenient and practical way to deal with times and time differences arises. The calendar dates, featuring years, months and days, we are used to exploit in the everyday life are problematic. The Gregorian calendar, now used universally for civil purposes, and the Julian calendar, its predecessor in the western world, are not suitable for astronomical problems. Two reasons would be for instance the different size of months and the leap years. Another method to express the date was sought: the *Julian days count*.

The Julian days count is a uniform count of days and fractions since noon Universal Time on January 1, 4713 BCE (Julian proleptic² calendar). Once one has the Julian day number of a particular date in history, it is easy to calculate time elapsed between it and any other Julian day number, by a straightforward subtraction. Thanks to their simplicity and readiness, Julian days numbers are widely used as time variables within the astronomical world. Note that the time scale that is the basis for Julian days count is Universal Time, and that 0h UT corresponds to a Julian date fraction of 0.5. The use of Universal Time is convenient for astronomers, that can only observe celestial bodies from Earth at night.

The Julian days count (see Jefferys [27]) has nothing to do with the Julian calendar introduced by Julius Caesar. In fact, it is named after Julius Scaliger, the father of Josephus Justus Scaliger, who invented the concept. It can also be thought of as a logical follow-on to the old Egyptian civil calendar, which also used years of constant lengths. Scaliger chose this particular date in the remote past because it was before recorded history and because in that year three important cycles coincided with their first year of the cycle: the 19-year Metonic Cycle, the 15-year Indiction Cycle (a Roman Taxation Cycle) and the 28-year Solar Cycle (the length of time for the old Julian Calendar to repeat exactly).

A large number of days has transpired since JD 0, almost 2.5 million days. Events that occurred several millennia in the past, though plausibly very interesting, are no concern for modern space missions that are rather like to happen in the nearby future. For this reason, instead of storing and using six digits numbers, plus floating points, it's easier to rescale the zero for the Julian days. *modified Julian days* (or simpler MJD) are instead used. Modified Julian days are the number of days uniformly counted from 0h UT January 1, 2000 (JD 2451544.5).

The conversions from familiar Gregorian calendar dates to Julian day numbers is mainly done automatically, either from the HORIZONS web-interface or by the free online converter, found at <http://aa.usno.navy.mil/data/docs/JulianDate.php>.

Gregorian date to Julian days count 4.1. *This is a simple algorithm to calculate the Julian day number of any date given on the Gregorian calendar. The Julian day number so calculated will be for 00:00 hours, GMT, on that date.*

1. Express the date as YMD , where Y is the year, M is the month number (Jan = 1, Feb = 2, etc.), and D is the day in the month.

² The Julian proleptic calendar is produced by extending the Julian calendar backwards to dates preceding AD 4, when the quadrennial leap year was established. The leap years that were actually observed between the implementation of the Julian calendar in 45 BC and AD 4 were erratic.

2. If the month is January or February, subtract 1 from the year to get a new Y, and add 12 to the month to get a new M. (Thus, January and February are thought as being the 13th and 14th month of the previous year).
3. Dropping the fractional part of all results of all multiplications and divisions, let

$$\begin{aligned} A &= \frac{Y}{100} & B &= \frac{A}{4} & C &= 2 - A + B \\ E &= 365.25(Y + 4716) & F &= 30.6001(M + 1) & JD &= C + D + E - 1524.5 \end{aligned}$$

This is the Julian day number for the beginning of the date in question at 0 hours, Greenwich time. Note that this always gives a half day extra. That is because the Julian day begins at noon, Greenwich time.

EXAMPLE Let's compute the Julian day number for July 22, 2014.

$$\begin{aligned} A &= 20 & B &= 5 & C &= -13 \\ E &= 2458132 & F &= 244 & JD &= 2456860.5 \end{aligned}$$

The result is in accordance with the online converter.

Similar algorithms are available, that convert a Julian day number to a Gregorian date. However, they are more numerous and require special attention according to the actual year in Gregorian date.

Julian days count to Gregorian date 4.2. This algorithm converts Julian days count date into Gregorian date. Dropping the fractional part of all results of all multiplications and divisions:

$$\begin{aligned} Z &= JD + 0.5 & W &= \frac{Z - 1867216.25}{36524.25} & X &= \frac{W}{4} \\ A &= Z + 1 + W - X & B &= A + 1524 & C &= \frac{B - 122.1}{365.25} \\ H &= 365.25C & E &= \frac{B - H}{30.6001} & F &= 30.6001E \\ D &= B - H - F & M &= \begin{cases} E - 1 & \text{if } E \leq 13 \\ E - 13 & \text{if } E > 13 \end{cases} & Y &= \begin{cases} C - 4715 & \text{if } M \leq 2 \\ C - 4716 & \text{if } M > 2 \end{cases} \end{aligned}$$

EXAMPLE Let's compute the zero for the modified Julian days, JD 2451544.5.

$$\begin{aligned} Z &= 2451545 & W &= 15 & X &= 3 \\ A &= 2451558 & B &= 2453082 & C &= 6715 \\ H &= 2452653 & E &= 14 & F &= 428 \\ \text{day} &= 1 & \text{month} &= 1 & \text{year} &= 2000 \end{aligned}$$

4.3 VALIDATION OF THE DYNAMICAL PROBLEM INTEGRATION

In this section numerical integrations of selected celestial bodies are performed by means of the tool developed for this thesis. The resulting state vectors are then compared with the values calculated via web-interface *HORIZONS*, taken as exact reference.

A validation procedure of this kind should theoretically require a relatively large amount of data and simulations to establish a statistical population on which reliable affirmations, error analysis and forecasts can be made. Since this problem is highly time-and (hardware) space-demanding, it has been tackled in a slightly simpler way: instead of randomly selecting celestial bodies to be integrated, they are split into different categories, for instance related to their orbits or mass, and some representative examples for each category are chosen. The Sun, the main planets, Pluto and the Moon are extrapolated from the ephemeris files and should be treated as exact. The other celestial objects which pertain to the solar system, a part from its central star and the revolving planets, are the dwarf planets, the natural satellites or moons, the asteroids, the comets, the Oort Cloud bodies and the meteoroids. Among these, the asteroids represent surely the largest category and shall therefore analysed in a more detailed fashion.

Table 4.5: Recognised dwarf planets

Dwarf planet	Satellites
Ceres	
Sedna	
Haumea	Hi’ika Namaka
Eris	Dysnomia
Makemake	
Pluto	Charon

One of the main assumptions made at the beginning of Chapter 3 was the restrictiveness of the dynamical problem, the mutual gravitational influence be discarded. That is, the celestial object at hand, does not sense the gravitational influence of other bodies and, in turn, these bodies are not influenced by its gravity. It’s straightforward to imagine that this hypothesis looses validity for those celestial objects whose mass is large enough to sensibly perturb the orbit and the dynamical features of the main objects contained in the ephemeris. An integration performed on such objects would accordingly produce large errors. In fact, there are several objects orbiting the solar system that have masses similar to the one of Pluto, or even bigger. This is the case for the

bigger moons of Jupiter and Saturn, and for the majority of the dwarf planets. Caution shall be hence exerted when interpreting the results for such small bodies. Just to name a few, the Galilean moons, Titan, Triton and Eris are more massive than Pluto, whereas Haumea, Makemake and Charon are smaller of approximately one order of magnitude.

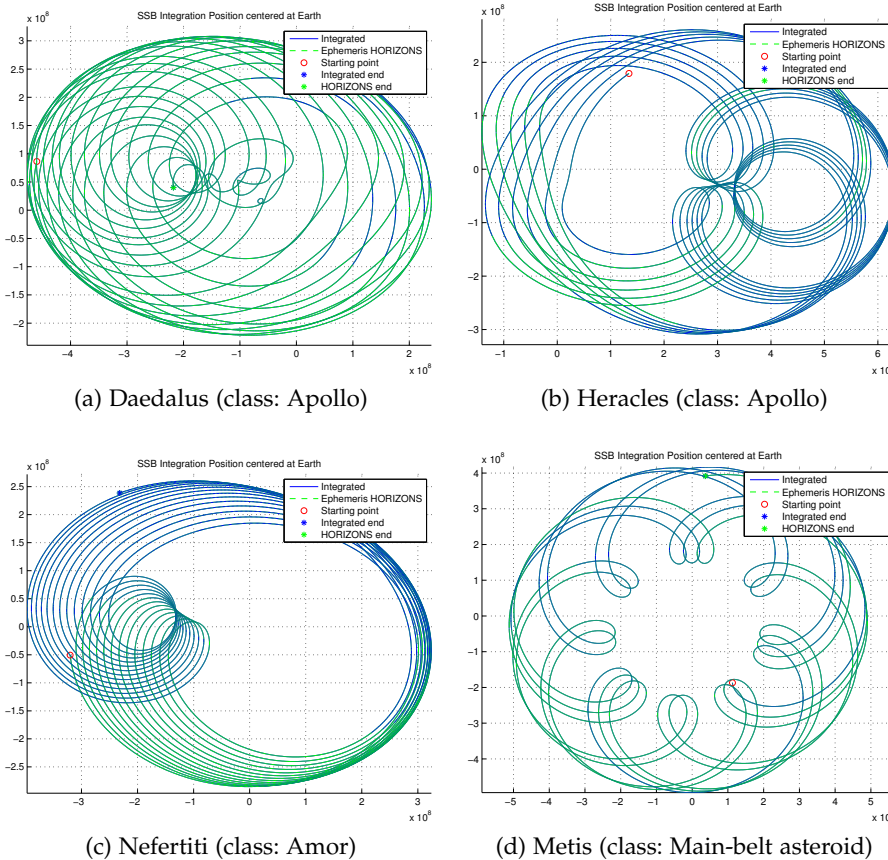


Figure 4.1: x-y projection of orbital trajectories of different small objects, centred at Earth

In Table 4.6 the more massive natural satellites of planets are listed and ordered according to their mass. Table 4.5 lists the dwarf planets recognised by the International Astronomical Union (IAU), and some of their natural satellites. To be more precise, the IAU General Assembly that gathered in Prague in 2006 came out with a Resolution that is now the worldwide accepted definition and standard classification for celestial bodies in the solar system.

IAU General Assembly Resolution 5A 4.3. *The rules established and formalised by resolution 5A read:*

- (1) *A "planet" is a celestial body that (a) is in orbit around the Sun, (b) has sufficient mass for its self-gravity to overcome rigid body forces so that it assumes a hy-*

drostatic equilibrium (nearly round) shape, and (c) has cleared the neighbourhood around its orbit.

- (2) A "dwarf planet" is a celestial body that (a) is in orbit around the Sun, (b) has sufficient mass for its self-gravity to overcome rigid body forces so that it assumes a hydrostatic equilibrium (nearly round) shape, (c) has not cleared the neighbourhood around its orbit, and (d) is not a satellite.
- (3) All other objects, except satellites, orbiting the Sun shall be referred to collectively as small solar-system bodies.

With Resolution 6A, written during the very same assembly, the dispute about Pluto was finally settled: the celestial body named Pluto belongs to the dwarf planets category.

Table 4.6: List of several natural satellites of planets, ordered by mass

Planet		Natural Satellites			
Earth	Moon				
Mars	Phobos	Deimos			
Jupiter	Ganymede Himalia Pasiphaë	Callisto Amalthea Carme	Io Elara	Europa Thebe	
Saturn	Titan Tethys Hyperion Pandora	Rhea Enceladus Janus	Lapetus Mimas Epimetheus	Dione Phoebe Prometheus	
Uranus	Titania Miranda Juliet	Oberon Puck Belinda	Ariel Sycorax	Umbriel Portia	
Neptune	Triton Galatea Halimede	Proteus Despina Neso	Nereid Thalassa Sao	Larissa Naiad Laomedea	

The class of small space objects represented by the asteroids is the main source for the validation procedure it is carried out here. They are so numerous that a precise and unique classification is difficult, if not impossible. Vast amount of information is available on astrodynamical almanacs and on the Internet. The same subdivision adopted by the JPL Small-Body database

search engine, at http://ssd.jpl.nasa.gov/sbdb_query.cgi#x, is followed here. Namely, asteroids are divided according to their distance from the Sun. Let a , q , Q be the semi-major axis, the perihelion and the aphelion, respectively, expressed in astronomical units, of the asteroid; and e is the eccentricity of its orbit. These parameters are extrapolated as mean osculating elements of the orbit, that is assuming instantaneously Keplerian trajectories. Asteroids are then classified as follows:

- (1) *Atira*: also known as IEO (Interior Earth Orbits), the orbit is entirely contained within the Earth orbit, $Q < 0.983$
- (2) *Aten*: near-Earth asteroid, $a < 1$ and $Q > 0.983$;
- (3) *Apollo*: near-Earth asteroid, $a > 1$ and $q < 1.017$;
- (4) *Amor*: near-Earth asteroid, $1.017 < q < 1.3$;
- (5) *Mars-crosser*: the asteroid crosses the orbit of Mars, $1.3 < q < 1.666$ and $a < 3.2$;
- (6) *Inner main-belt asteroid*: $a < 2$ and $q > 1.666$;
- (7) *Main-belt asteroid*: $2 < a < 3.2$ and $q > 1.666$;
- (8) *Outer main-belt asteroid*: $3.2 < a < 4.6$;
- (9) *Jupiter trojan*: trapped in Jovian Lagrangian points $L_{4,5}$ such that $4.6 < a < 5.5$ and $e < 0.3$;
- (10) *Centaur*: orbits between Jupiter and Neptune, $5.5 < a < 30.1$;
- (11) *Transneptunian object*: orbits outside Neptune path, $a > 30.1$.

Table 4.7 shows some examples of asteroids, split according to this classification and Figure 4.1 represents the x-y orbits section of some, centred at Earth. An interesting example is shown in Figure 4.2, where the orbit of Achilles, a Jupiter trojan, is shown in the Sun-Jupiter roto-pulsating frame. It's clear how the asteroid keeps orbiting in a quasi-period fashion around the Jovian L_4 .

The data on celestial bodies comes from the HORIZONS web-interface database mentioned above and it is geocentric. The error calculations, on the other hand, will be performed in a solar system barycentric frame of reference. The simulations for the validation of the integrators will be done for three time intervals: short (27 years), medium (113 years) and long period (428 years), as described in Table 4.8.

The integration process, generally, produces results that are not the same size of the comparison population. An interpolation technique, such as a simple cubic spline, is necessary to evaluate the error at each discrete time along

Table 4.7: Asteroids

Category		Asteroids		
Atira		Atira		
Aten	Aten	Khufu	Apophis	
Apollo	Icarus Daedalus Heracles	Geographos Cerberus Zeus	Toro Dionysus Beowulf	Apollo Camillo
Amor	Eros Florence	Amor Nefertiti	Quetzalcoatl Lyapunov	Seneca Camarillo
Mars-crosser	Aethra Nemo Shenzhou	Brucia Dvorak	Rosina Wisdom	Sirene Eureka
Inner-belt		Sequoia	Einstein	Vulcano
Main-belt	Pallas	Juno	Vesta	Astrea
	Hebe	Flora	Metis	Hygiea
	Parthenope	Victoria	Eunomia	Fortuna
	Circe	Atalante	Harmonia	Daphne
	Aurora	Artemis	Lacrimosa	Mr. Spock
	Jabberwock			
Outer-belt	Cybele	Hermione	Syilla	
Jupiter Trojan	Achilles	Aenas	Diomedes	Philoctetes
Centaur	Hidalgo	Damocles	Amucus	
Transneptunian	Chaos	Varuna	Rhadamanthus	

Table 4.8: Periods for the validation

Period	Starting date	Ending date	Time span
Short	2011 30 August	2038 July 22	27 years
Medium	1987 12 July	2100 December 25	113.5 years
Long	1789 3 December	2217 September 17	428 years

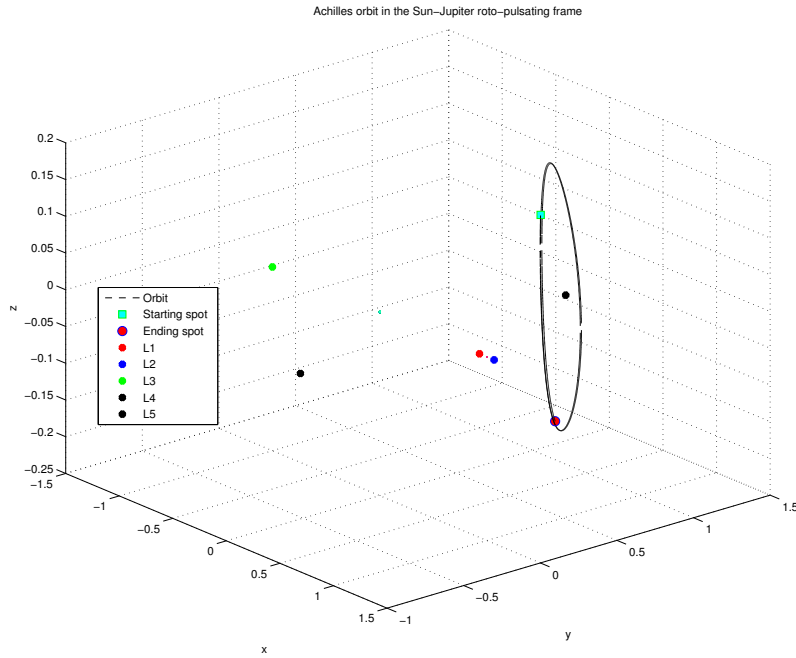


Figure 4.2: Trajectory of the Jupiter trojan Achilles, Sun-Jupiter roto-pulsating frame

the integrated trajectory. Since data interpolation might suffer from instability and poor accuracy, especially when dealing with long intervals and non-smoothly varying polynomials, the numerical integrator deals automatically with the size of the output³. In the case at hand, the numerical solver first integrates at variable step size points in order to respect the user specified tolerances, and at last the orbit is evaluated at specified points. With this convention the error is simply calculated as difference between the *HORIZONS* data and the integrated result:

$$\mathbf{err} = \mathbf{x}_{\text{HORIZONS}} - \mathbf{x}_{\text{integrated}} \quad (4.13)$$

As mentioned earlier, the amount of data that has been analysed is fairly large and the presentation is limited here to some significant cases. The examples selected barely serve as illustration on how the validation process has been conducted and shows that neglecting perturbations can sometimes lead to tangible errors. Nonetheless, for the large part of the cases the errors are under the tolerance that this work is intended to establish. It is remarkably important to note that such errors keep increasing without bounds, showing

³ Were an interpolation procedure be necessary, it should be done in the SSB reference frame, where the state vector function, solely known numerically, will show presumably fair property as far as data interpolation methods are concerned.

an almost-periodic trend that follows a mild linear increase. Hence, as time passes, an epoch will surely appear, for which the local error exceeds the fixed tolerance and of which unacceptable state vectors follow; this is often the case for the long period simulations. The reader can however rest assured, in fact the purpose of this thesis is not creating an integrator that can rival the one JPL is already using since years; instead the goal is to propagate an initial condition in time under the gravitational flow in order to find trajectories with special properties, such as dynamical substitutes, or to continue orbits calculated in the RTBP to the more general n-body problem. What is more, the celestial body the attention is focused on, is not a natural body, but it is rather a spacecraft and as such it can be controlled periodically to reduce the errors occurring in the state vector. For the same reason, the integration time should be coherent with the life-span of artificial satellites, which depends mainly on on-board power, fuel and on possibility of monitor and active control. The long-period results exceed the error tolerance, but they refer at the same time to a condition that is far beyond truthful for an average spacecraft in outer space. Finally, in order to have accurate results the restrictive assumptions should be released and the main perturbation effects accounted for. Such effects as relativity, planets oblateness and solar pressure shall hence be considered in these cases.

Table 4.9: Maximum position and velocity error of the SSB integration for various asteroids classes. Short and medium periods

Asteroid class	Position error (Km)		Velocity error (m/s)	
	Short	Medium	Short	Medium
Atira	2938.41	8314.07	1.2965	3.885
Aten	4.06069e7	18710	8704.08	8.489
Apollo	3579.21	2.56593 e5	4.1138	78.25
Amor	1351.17	45326.6	0.1886	7.305
Mars-crosser	2022.02	12229.7	0.1657	1.149
Inner-belt asteroid	782.42	5386.27	0.06219	0.4345
Main-belt asteroid	1974.84	33860.8	0.1184	2.074
Outer-belt asteroid	630.22	2607.05	0.02194	0.09602
Jupiter trojan	170.94	269.39	3.24 e-3	4.72 e-3
Centaur	136.08	3192.06	5.16 e-3	0.1752
Transneptunian object	0.955	7.688	2.11 e-6	7.3 e-6
Dwarf planet	222.16	2956.21	9.69 e-3	0.1395

4.3.1 Solar system barycentric integration

The analysis of the errors is much more easily performed on a SSB frame instead that in a non-inertial frame. This is because the contribution of the error can be addressed to the main perturbations neglected in this work, according to the position of the celestial body with respect to the Sun. For instance, a close-passage near Earth can substantially modify the trajectory due to oblateness of the planet and a highly elliptic orbit that rapidly accelerates near the Sun can be heavily influenced by the solar pressure and by relativity effects, directly depending on the velocity magnitude of the celestial body. Moreover, apparent perturbation frequencies may arise in a non-inertial reference.

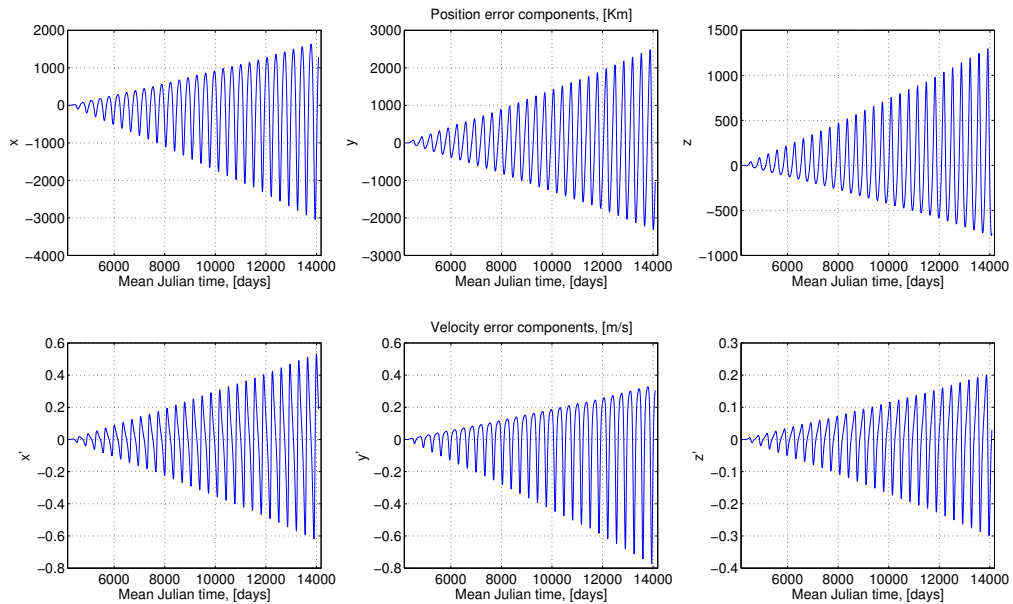


Figure 4.3: Error trend for Aten, class of the near-Earth asteroids Aten (Short period: 27 years). SSB integration.

Figures 4.3 and 4.4 show the errors trends for 2 different examples. The selected celestial bodies pertain to different classes and overall show that the mean error trend increases with time and that the error magnitude shows its major contribution for celestial bodies nearer the Earth. This is probably due to the fact that Centaurs, Transneptunian objects and other far small objects have an orbiting space that is ‘clearer’ from other major massive bodies with respect to near-Earth objects that might encounter in their trajectories a massive body several time, hence being influenced by their oblateness, not to mention the fact that the nearer an object is to the Sun the stronger the solar pressure acts upon it. Figure 4.5 shows the error trend for the long period in the case of Juno.

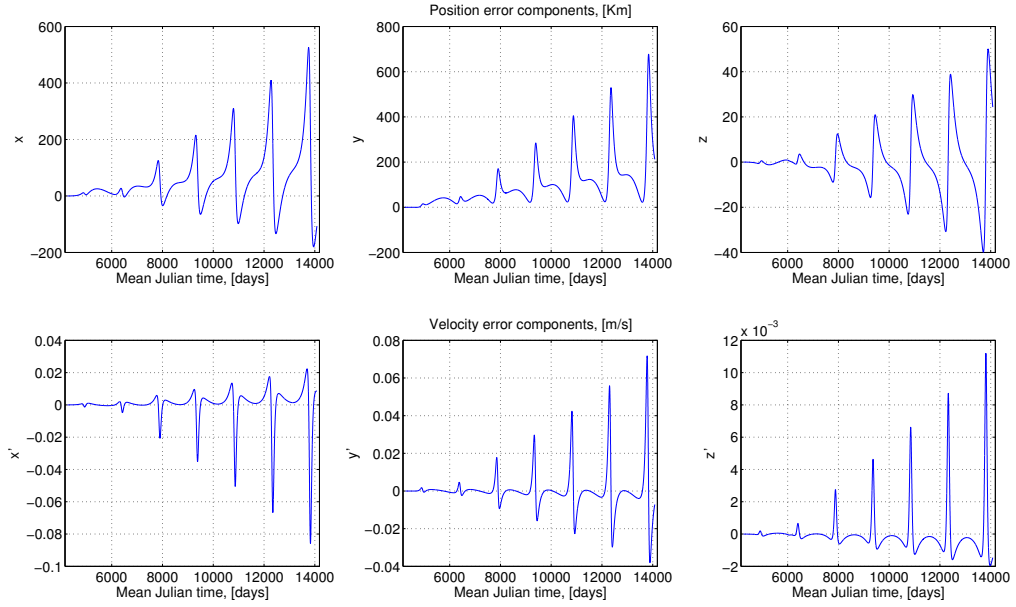


Figure 4.4: Error trend for Quetzalcoatl, class of the Amor (Short period: 27 years). SSB integration.

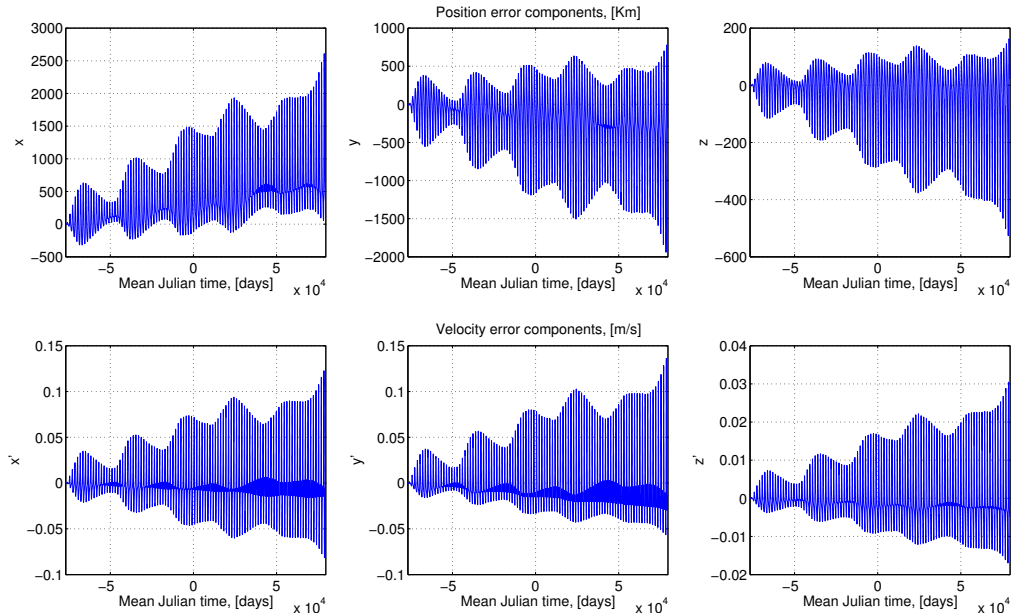


Figure 4.5: Error trend for Juno, class of the Main-belt asteroids (Long period: 428 years). SSB integration.

Table 4.10: Maximum position and velocity error of the SSB integration for various asteroids classes. Long period

Asteroid class	Position error (Km)	Velocity error (m/s)
Atira	32330.5	13.55
Aten	6.964644e7	29066.2
Apollo	4.428825e8	59378.8
Amor	3.72081 e5	51.94
Mars-crosser	1.50228 e5	14.08
Inner-belt asteroid	13312.7	1.049
Main-belt asteroid	1.91241 e5	10.87
Outer-belt asteroid	74383.4	2.67
Jupiter trojan	342.50	4.15 e-3
Centaur	9762.74	0.6158
Transneptunian object	71.714	7.25 e-7
Dwarf planet	33666.9	1.57

Table 4.9 displays the largest error, in norm and for each category, that occur in the integration. Both position and velocity are shown for the short and medium periods, respectively. Note that the boxed errors are much larger than the average. These boxed values corresponds to Apophis, the asteroid that was believed to have dangerous probability to be in Earth-collision trajectory⁴. I conjecture that this large error is caused by the possibility of impact. In fact, the integrator used in this work allows impacts to happen, but loses validity after the collision. This wrong prediction might give the massless body sufficient energy to escape the solar system gravitational pool, hence producing large errors. For this reason Apophis has been neglected in further error analysis. Table 4.10 is dedicated to the long period errors. The errors value of the class Aten for the medium and long periods have been calculated excluding

⁴ Apophis caused a brief period of concern in December 2004 because initial observations indicated a probability of up to 2.7% that it would hit Earth in 2029. Estimates puts its diameter at roughly 325 m. Additional observations provided improved predictions that eliminated the possibility of an impact on Earth or the Moon in 2029. However, a possibility remained that during the 2029 close encounter with Earth, Apophis would pass through a gravitational keyhole, a small region no more than about 800 m wide, that would set up a future impact on April 13, 2036. This possibility kept the asteroid at level 1 on the Torino impact hazard scale until August 2006, when the probability that Apophis would pass through the keyhole was determined to be very small. During the short time when it had been most concerning, Apophis set the record for highest rating on the Torino Scale, reaching level 4.

Apophis for obvious reasons. Note how in the long run, two further celestial objects escape the solar system. They both are NEO.

4.3.2 Roto-pulsating integration

The integration in the roto-pulsating frame is a little more delicate. The accuracy of the results turns out, as expected, to depend strongly on the selection of the primaries. It's intuitive to think that, if the contribution of a celestial body that has been considered as perturbation in the dynamic model actually gives rise to a force that is comparable to the primaries gravitational effects, then the method might lose its stability and accuracy properties. The results are in accordance with this conjecture. In the following, the validation is carried out in both the Sun-Jupiter and the Sun-Earth system for asteroids of various classes. In Figure 4.6 trajectories of 4 different celestial bodies can be seen.

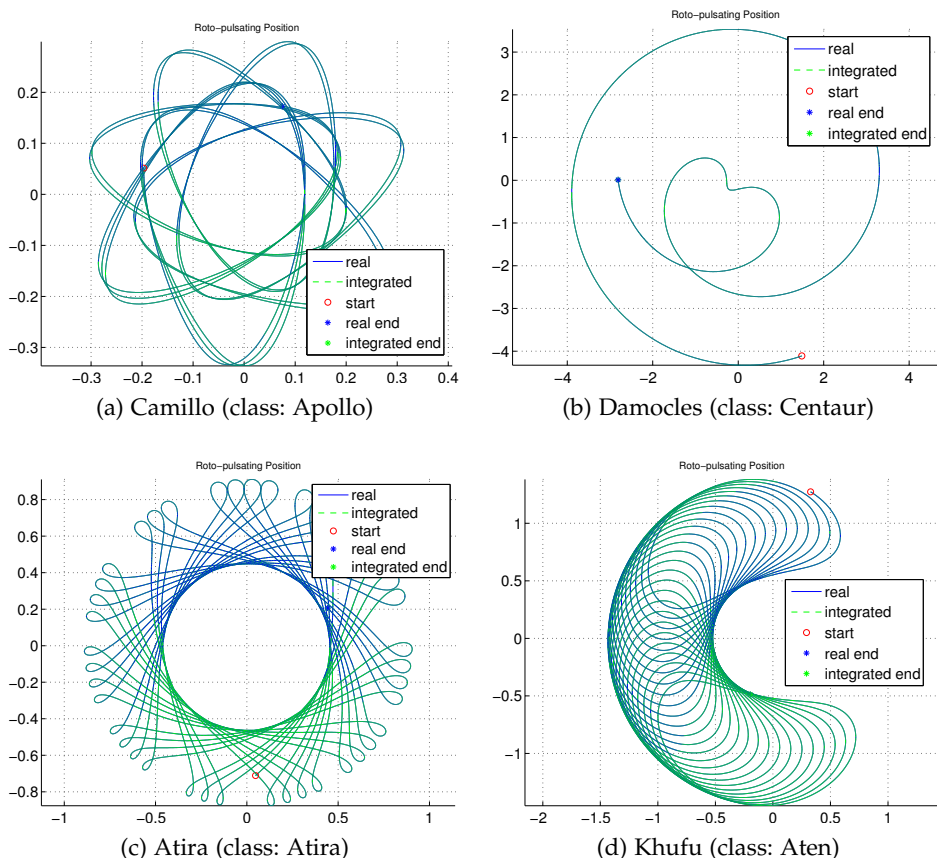


Figure 4.6: x-y projection of orbital trajectories of different small objects in the Sun-Jupiter (top figures) and in the Sun-Earth synodic frame (bottom figures)

Due to the computational effort⁵ the integration has been performed only for the short period: 27 years. The error trends for longer periods might be extrapolated from these results without performing the integration, and assuming quasi-linear error increase behaviour.

SUN-JUPITER SYNODIC FRAME Figures 4.7 and 4.8 display the error trend for Icarus and Aneas. The Apollo-class asteroid exhibits a steady increase in the error superimposed to an oscillation. On the other hand, the results concerning the Jupiter trojan are quite satisfactory: the error of integration of a trajectory near the Lagrangian point seems to increase at a mild pace, and shows low frequency content. This result assures that the integration of unknown objects and the propagation of initial conditions in the neighbourhood of the libration points has bounded error. The key for reliability and trust-region of subsequent procedures dwells in this result. For the objective intended to pursue, namely the seek of quasi-periodic orbits in the neighbourhood of libration points, it is of paramount importance that the integrator possesses high precision and efficiency in those zones.

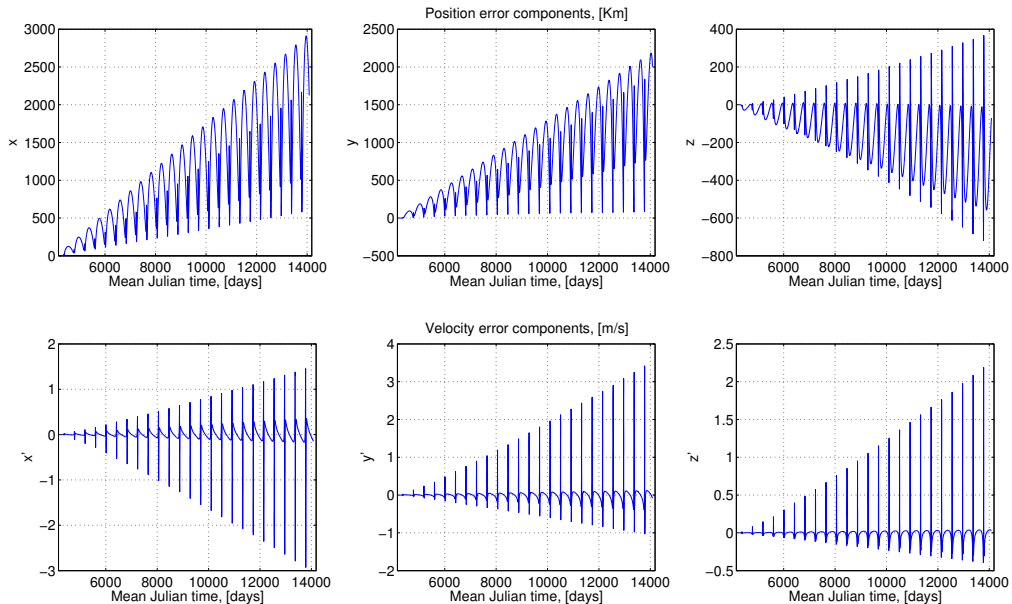


Figure 4.7: Error trend for Icarus, class of the Apollo. Sun-Jupiter synodic frame

In general, the integration in the roto-pulsating Sun-Jupiter system produces errors that are very similar, both in trend and numerical value, to the ones obtained during the solar system barycenter integration. Table 4.11 shows the numerical values for the Sun-Jupiter and Sun-Earth systems error. Furthermore,

⁵ Integration of an Amor-class asteroid for 27 years requires 742 seconds in the Sun-Jupiter system, and 50 minutes in the Sun-Earth system, on a MacBookPro 2.9 Ghz Intel Core i7 8 Gb RAM, two 1.6 GHz DDR3 memory modules.

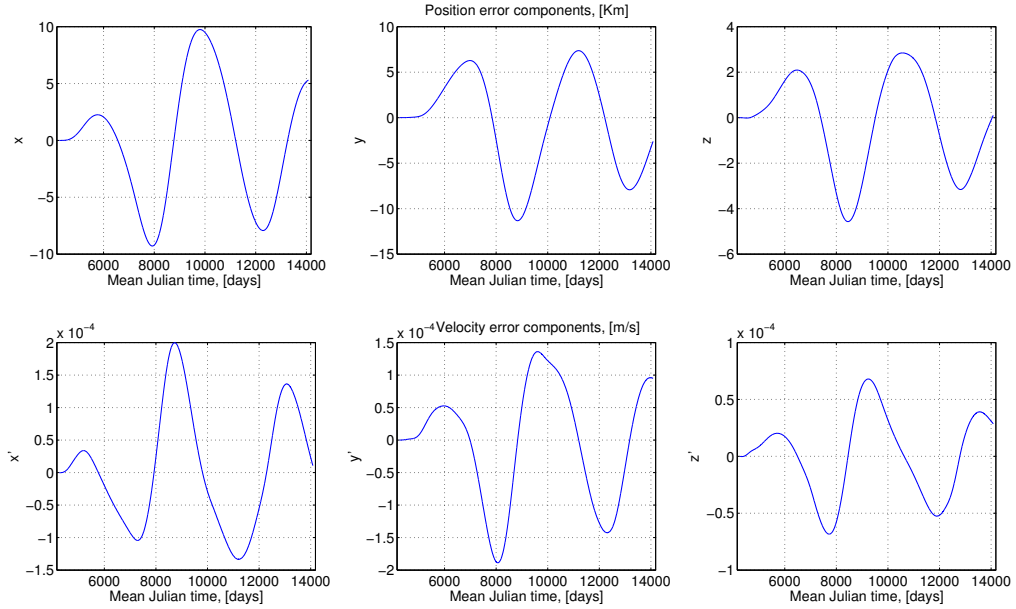


Figure 4.8: Error trend for Aneas, class of the Jupiter trojan. Sun-Jupiter synodic frame

Table 4.11: Maximum error of the roto-pulsating integration for various asteroids classes. Short period

Asteroid class	Position error (Km)		Velocity error (m/s)	
	Sun-Jupiter	Sun-Earth	Sun-Jupiter	Sun-Earth
Atira	2939.83	1813.24	1.297	0.7994
Aten	3222.47	4226.49	0.8086	1.776
Apollo	3579.24	50490.4	4.099	25.52
Amor	1262.06	70529.4	0.1748	7.345
Mars-crosser	1922.21	48036.5	0.1574	3.788
Inner-belt asteroid	819.66	9901.82	0.06501	0.7721
Main-belt asteroid	2028.40	42639.8	0.1217	2.614
Outer-belt asteroid	529.49	35326.4	0.01848	1.189
Jupiter trojan	94.87	1.24584 e5	1.899 e-3	2.296
Centaur	1919.99	2.46778 e6	0.1404	180.14
Transneptunian object	2509.49	2.89210 e6	6.432 e-3	7.145
Dwarf planet	5286.81	6.07655 e6	0.01295	14.34

it is clear from Figure 4.6 that the trajectory shape, and hence the main dynamical component, is preserved; even though large errors occur. This is because the problem features a wide range of astrodynamical distances within the solar system. It's easy to prove that the relative error is quite low when analysing objects orbiting tens of Astronomical Units away and featuring errors of thousand of Kilometers⁶. The most critical case corresponds to Eris⁷, as integrated in the Sun-Earth system: its relative error is 4%. The asteroid Atira has 0.0012% of relative error and Heracles (pertaining to the Apollo-class) 0.0337%.

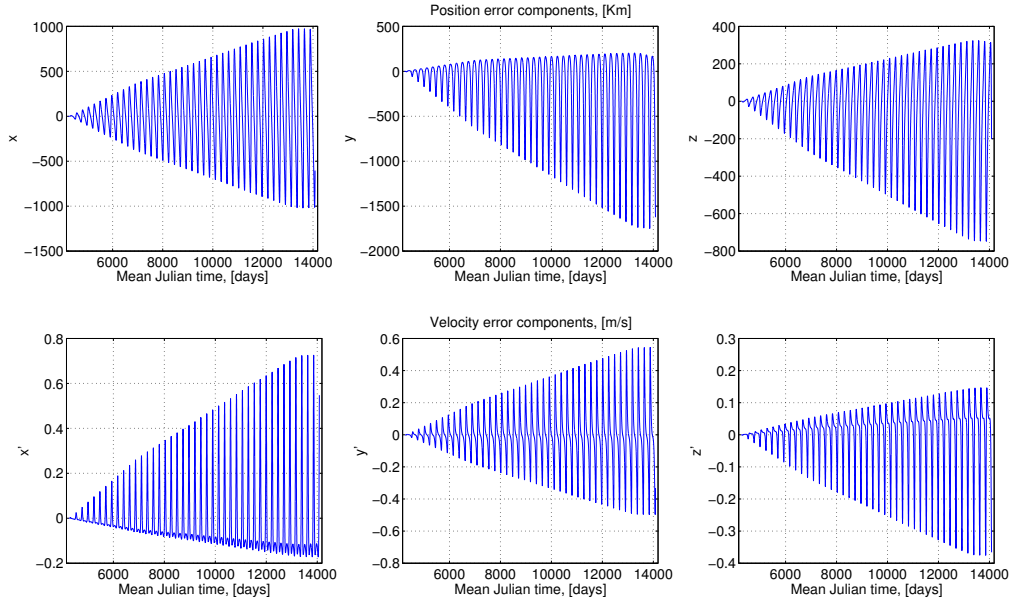


Figure 4.9: Error trend for Atira, class of the Atira. Sun-Earth synodic frame

SUN-EARTH SYNODIC FRAME The integration in the Sun-Earth system produces results that are much more amenable to errors, due to the perturbations from the other celestial bodies that are in fact much higher than the gravitational contribution of the primaries for some classes of small objects and for trajectories far from Earth. If ordered by mass, Earth occupies the sixth position in the solar system, after the Sun, Jupiter, Saturn, Neptune and Uranus. It's quite reasonable at this point, looking at the distribution of small objects trajectories within the solar system, to understand why position and velocity errors magnitude are larger and larger as the selected small object pertain to a category whose orbital path lies far away from Earth and its natural attractor

⁶ 149600 Km is just 0.1% of a AU.

⁷ Eris is the most-massive known dwarf planet in the Solar System and the ninth-most-massive body known to directly orbit the Sun. Estimated to be 2.326 (± 12) Km in diameter and 27% more massive than Pluto, or about 0.27% of the Earth's mass. As of 2014, its distance from the Sun is 96.4 AU, roughly three times that of Pluto, and with the exception of some comets it is currently the most distant known natural object in the solar system.

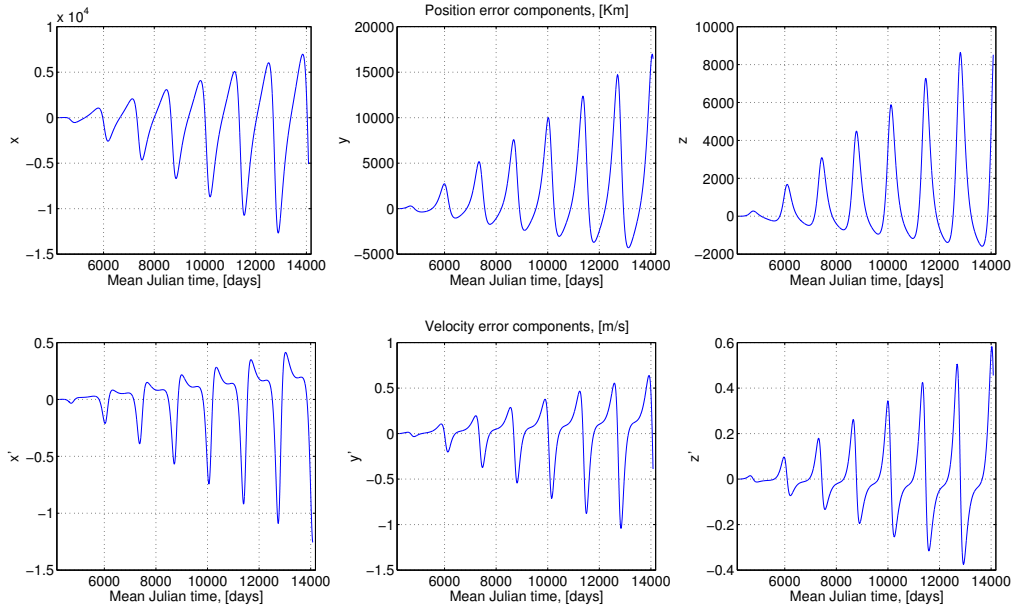


Figure 4.10: Error trend for Brucia, class of the Mars-crossers. Sun-Earth synodic frame

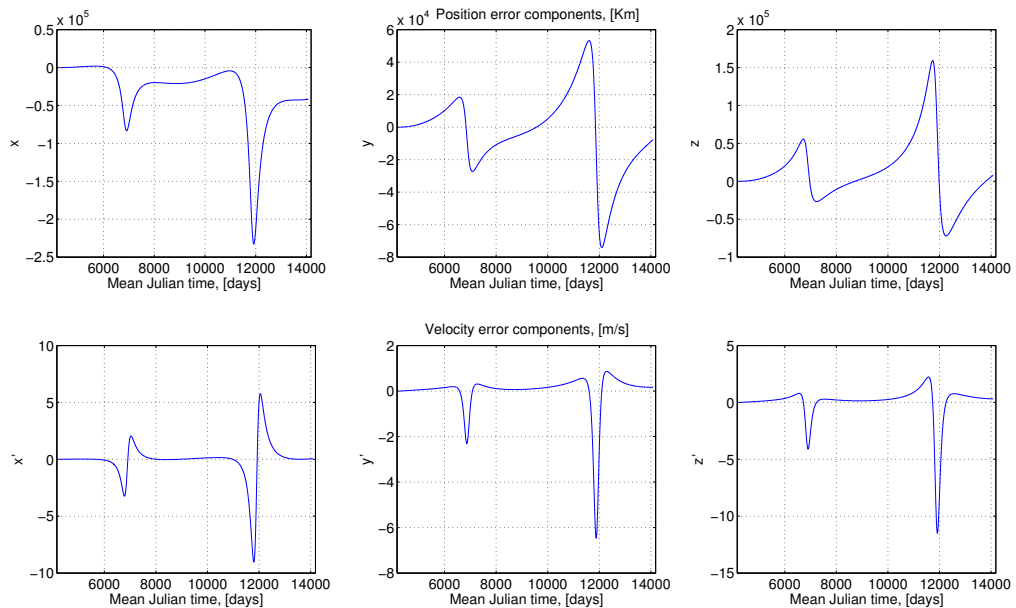


Figure 4.11: Error trend for Hidalgo, class of the Centaurs. Sun-Earth synodic frame

might be another of the main planets. Furthermore, it's interesting to note how errors tend to have a steady increase with time and a quasi-periodic fashion. Figures 4.9 and 4.10 display the error trend for two different asteroids. Note that the Near-Earth-Object Atira features fairly small numerical values of the error. This response was expected, since the Sun and Earth are the natural attractors for such a celestial body. For far objects the errors trends are very similar to the ones obtained in the Sun-Jupiter synodic system. An example is Hidalgo, in Figure 4.11, showing exactly the same error trend (two neat discontinuities resembling a second order system resonance and anti-resonance behaviour) for both Sun-Jupiter and Sun-Earth synodic frames, but in the latter the error magnitude is of the thousands of kilometers, compared to few hundreds Km for the first case.

4.3.2.1 Natural satellites

Validation for natural satellites takes its own special position within the framework of this work. Due to their fast dynamics, it is difficult to disclose the problem in the SSB frame; however, this type of motion is naturally represented in a system that accounts for their main attractor. Writing the dynamics in the synodic reference which contains the Sun and the satellite primary attractor, not only the integration is faster, but also the dynamics itself is represented in a framework more compliant with the reality of the problem at hand.

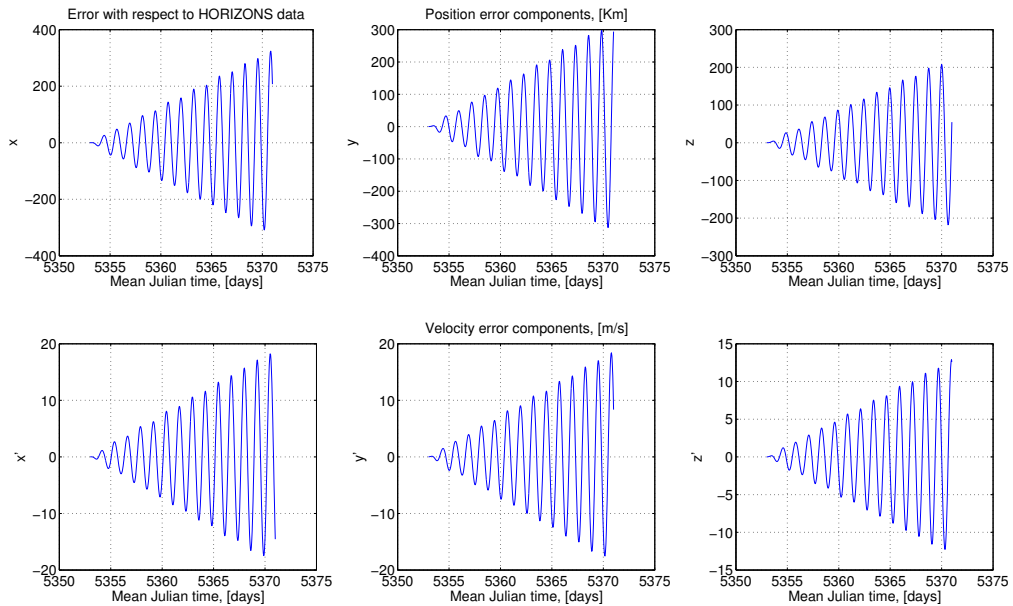


Figure 4.12: Error trend for Deimos, natural satellite of Mars. Sun-Mars synodic frame

Another common feature of natural satellites is the spatial vicinity to the primary, which makes the satellite dynamics more sensible to perturbations. The effect of oblateness of the master planet cannot be neglected and umbra-

penumbra zones fully envelopes the satellite when it orbits in the ‘dark side’. For these reasons the validation procedure has been applied to several natural satellites for a relatively short time, but always to grant at least several revolutions to occur, ranging from 4-10 for large orbits to 20-40 for smaller and faster orbits. Table 4.12 shows the maximum position and velocity errors, in norm, for several satellites, highlighting primary body, integration time and completed revolutions. Figure 4.12 displays the error trend for Phobos, the largest martial satellite. The error trend shows the usual oscillation superimposed to a linear increase; in this case the increase is steeper if compared to the error trend of the asteroids.

Finally, errors ascribable to big moons must be interpreted with care. In fact, the problem solved here is restricted, and can’t account for the legitimate mutual influence among massive objects, such as a moon orbiting very close to a planet. The data presented in Table 4.12 regarding Callisto, Io and Titan shall not be used as a reliable reference.

Table 4.12: Maximum error for several selected natural satellites in their natural synodic frame

Satellite	Error		Primary	ΔT (revs) [days]
	Position [Km]	Velocity [m/s]		
Deimos	363.8454	20.9841	Mars	18 (14)
Phobos	2949.6312	685.3064	Mars	18 (56)
Callisto	20531.096	88.24	Jupiter	167 (10)
Io	29876.269	1210.856	Jupiter	18 (10)
Pasiphae	3164.351	0.7271	Jupiter	3630 (4)
Mimas	57232.12	4324.9191	Saturn	18 (19)
Phoebe	921.403	0.13606	Saturn	3630 (6)
Titan	109360.447	511.04	Saturn	167 (10)
Ariel	17238.69	496.318	Uranus	167 (66)
Oberon	12436.88	66.6353	Uranus	167 (12)
Sycorax	1022.682	0.1239	Uranus	3630 (2)
Nereid	1371.418	1.6851	Neptune	3655 (10)
Triton	76307.983	946.181	Neptune	167 (28)
Charon	34898.008	563.697	Pluto	167 (26)

4.3.3 Double-way validation

In this section a set of random initial conditions will be propagated forward in time by means of both the SSB integrator and the synodic integrator. Since the astrodynamics model is chaotic by nature, attention is exerted when considering large time spans. In particular, escape from the solar system is theoretically allowed (even though requiring a huge amount of energy), in which case the gravitational model used so far is no longer valid. Moreover, collisions with other major celestial bodies are allowed to occur as well, situations which lead to a singularity in the equations, that the numerical procedure cannot deal with.

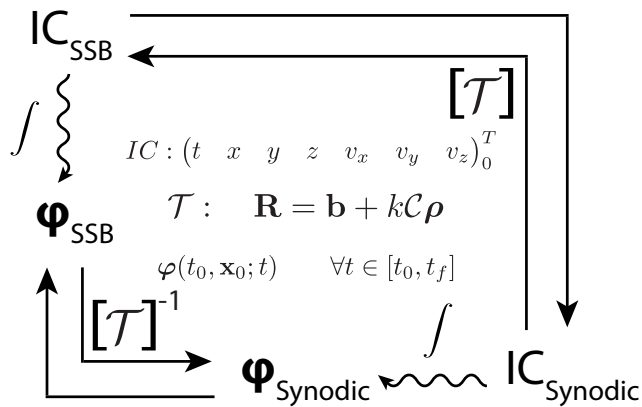


Figure 4.13: Double-way validation scheme

For these reasons, and in order to select initial conditions which exhibit at least physical meaning in some approximated models, Keplerian trajectories have been chosen as seeding points. To this extent, the orbit is first calculated in the perifocal frame of the selected primary and then rotated to the planetocentric frame of reference at date January 1, 2000 by means of Eq. (2.21). Several cases have been analysed for each major synodic frame in the solar system. In order to simplify somehow the problem and to have common parameters for benchmark among the study-cases, three out of six orbital parameters have been fixed in the selection of the initial conditions for all the Keplerian trajectories propagated in the complete solar system model. That is, the right ascension of the ascending node, the inclination and the argument of periapsis have been fixed.

$$\Omega = 71^\circ$$

$$i = 65^\circ$$

$$\omega = 17^\circ$$

The other three parameters are specified as periapsis distance, eccentricity and true anomaly.

Table 4.13: Parameters of the double-way validation objects

ID	Synodic frame	Primary	Orbital parameters			ΔT [days]
			r_p [Km]	e []	θ [$^\circ$]	
1A	Sun-Mercury	Mercury	6e3	0.7	260	21
1B			13e3	1.9	265	1600
2A	Sun-Venus	Venus	18e3	0.15	0	23
2B			8e3	5	275	365
3A	Sun-Earth	Earth	36e3	0	0	15
3B			1e4	1.12	230	365
4A	Sun-Mars	Mars	1e4	0.95	0	365
4B			4e3	10.5	275	1825
5A	Sun-Jupiter	Jupiter	2e5	0.2	215	12
5B			75e3	1.05	215	6570
5C		Sun	3e6	0.1	0	20
5D			1e6	1	195	73000
6A	Sun-Saturn	Saturn	2e6	0.45	0	1460
6B			1e5	1	195	10950
7A	Sun-Uranus	Uranus	45e3	0.75	0	35
7B			1e6	6.6	265	36500
8A	Sun-Neptune	Neptune	31e3	0.25	0	4
8B			8e4	1.05	205	73000
9A	Sun-Pluto	Pluto	4e3	0.5	0	25
9B			6e3	1.22	216	73000
10A	Earth-Moon	Earth	42e3	0	0	15
10B			1e4	2.1	245	365
10C		Moon	3e3	0.7	0	20
10D			7e3	0.7	0	60
10E			1.9e3	3.33	255	90

Table 4.14: Errors of the double way validation study cases

ID	err _{SSB}		err _{Syn}	
	Position [Km]	Velocity [m/s]	Position [Km]	Velocity [m/s]
1A	0.7406	1.6536e-4	0.6575	1.4657e-4
1B	7425.403	8.27e-3	6368.717	3.546e-3
2A	0.4472	9.7571e-5	0.433	9.4389e-5
2B	167.207	5.569e-5	162.4	2.073e-5
3A	8.9e-3	5.805e-7	91e-3	5.892e-7
3B	95.2235	1.6332e-5	96.8373	6.607e-6
4A	34.9364	3.6e-3	31.5887	3.2e-3
4B	652.3022	6.853e-5	639.4532	3.8548e-5
5A	0.0837	9.561e-6	0.0877	1e-5
5B	83.645	3.79e-6	80.0579	3.026e-6
5C	0.0317	2.094e-6	0.0332	2.191e-6
5D	721.8388	3.746e-6	717.7808	1.224e-5
6A	0.2662	4.589e-7	0.28	4.815e-7
6B	71.7087	7.166e-7	74.6553	3.728e-8
7A	0.3954	7.5363e-5	0.381	7.261e-5
7B	91.4271	1.465e-7	87.8892	1.218e-7
8A	0.052	2.372e-5	0.0549	2.363e-5
8B	606.2235	1.063e-6	609.581	8.106e-7
9A	0.0522	5.2917e-6	0.0679	6.873e-6
9B	47.057	4.397e-8	51.5613	2.451e-8
10A	0.072	5.095e-6	0.0746	5.173e-6
10B	1.1704e5	0.0138	1.1148e5	0.3132
10C	1.538	5.643e-4	1.6417	5.996e-4
10D	3.57	1.2e-3	3.3982	1.2e-3
10E	291.6487	8.88e-5	281.999	3.809e-4

The integration results are then transformed, the solar system barycentric integration results are rotated to the synodic frame with proper primaries selection, and the roto-pulsating integration results are in turn transformed into state vectors referred to the solar system centre of gravity. The transformation is described in Chapter 3. A direct comparison can at this point be made between the two methods. This procedure is schematised in Figure 4.13.

This kind of validation process seems to be unnecessary and redundant. In fact, it serves as mean to establish the error trend for all the orbits that were not suitable for the SSB or synodic validation procedure. Trajectories typical of the 2-body problem can be continued to the real ephemeris dynamics and considerations on the whole dynamical flow might be derived. It is important to note that, in these cases, there is no benchmark with reliable and commonly established results (like *HORIZONS*). The comparison is implemented solely between the results of the SSB and synodic integrator, that are approximated models. Assuming that the SSB integration is much more accurate than the synodic one, it becomes important to assess information about their difference. The synodic integrator will indeed be the starting point for all the derivations in subsequent chapters and will be treated as exact thanks to this validation process. Table 4.13 shows the cases that have been studied, providing for each seeding point the values of the orbital free parameters, the integration time, the primary, and an identification number ID. The errors, norm of the position and velocity vectors, are displayed in Table 4.14, for the corresponding ID. In this case there are two errors: err_{SSB} , the difference between the SSB integration and the transformed synodic integration results, and err_{Syn} , the difference between the transformed SSB integration and the synodic integration results.

5

METHOD AND RESULTS

This chapter conveys the results of the present thesis. The iterative procedure implemented to obtain such outcome is primarily based on the solution of a two-point boundary value problem (sometimes simpler referred as TPBVP) and retraces somehow the procedure used in Lian et al. [29]. The differential problem is not the classic one because some of its fundamental parameters are allowed to vary in a non conventional way. Notwithstanding, in Section 5.1, the classic formulation is briefly addresses, closely following Stoer and Bulirsch [40]. The variation to the classic TPBVP and the description of the iterative algorithm occupies Section 5.2. The last part is entirely dedicated to the presentation of the results; that is, dynamical substitutes of collinear points are calculated and graphically displayed for several synodic systems; and quasi-periodic orbits, corresponding to several Jacobian energy levels, (i.e., Halo and Lissajous orbits) are flown under the real ephemeris dynamics to find their equivalent.

5.1 TWO-POINT BOUNDARY VALUE PROBLEM

In this section a brief description of boundary value problems and on techniques to solve them are addressed. Thorough analysis and demonstrations of mathematical theorems standing at the basin of this kind of differential problems go beyond the scope of this thesis.

In particular, the two-point boundary value problem is object of interest. The system of first-order differential equations (3.37) which governs the space-craft dynamics requires suitable boundary conditions. In the simplest case, the question is what trajectory will the object follow in space and time if put at a certain point and with a certain velocity at a precise epoch. This obviously corresponds to specifying initial conditions at a fixed initial epoch. The integration scheme is straightforward and provides the trajectory of the spacecraft as unique solution, given a certain tolerance threshold. On the other hand, if a Lambert's problem or a rendezvous one have to be solved, the conditions provided are the ones at the boundaries, for instance the initial and final positions. It is proven that this problem does not admit, if it does at all, an unique solution; what is more, the solution is strongly affected by boundary condition

variations, not to mention the strong sensitivity to the ‘exactness’ of the initial guess, need to start the method.

On the whole, boundary value problems are more general than the initial value problems. In these, one seeks a solution $\mathbf{x}(t) \in \mathbb{R}^n$ of a system of n ordinary differential equations

$$\dot{\mathbf{x}} = \mathbf{f}(\mathbf{x}, t) \quad (5.1)$$

satisfying n general non-linear two-point boundary conditions in the form

$$\mathbf{r}(\mathbf{x}(t_a), \mathbf{x}(t_b)) = \mathbf{0} \quad (5.2)$$

where $t_a \neq t_b$ are given different epochs in \mathbb{R}^1 , and $\mathbf{r} : \mathbb{R}^{2n} \rightarrow \mathbb{R}^n$. The boundary condition equation can be linear through square matrices $\mathcal{A}, \mathcal{B} \in \mathbb{R}^{n \times n}$, and thus linearly separated thanks to the superimposition principle.

$$\begin{aligned} \mathcal{A}\mathbf{x}(t_a) + \mathcal{B}\mathbf{x}(t_b) &= \mathbf{c} & \text{or} & \mathcal{A}_1\mathbf{x}(t_a) = \mathbf{c}_1 \\ \mathcal{B}_2\mathbf{x}(t_b) &= \mathbf{c}_2 \end{aligned}$$

The boundary value problem might be adapted to a large variety of mathematical conundrums, such as eigenvalue problems (if the differential equations depend on a parameter σ , then determine for which set of the parameter the solution exists and is unique), free boundaries (the boundary conditions are known, but not the time t_b that must be determined as part of the solution) and so on.

In this thesis, two methods have established to solve the TPBVP: *simple shooting* and *multiple shooting*. They are both based on the concept of shooting, a fake initial problem is solved until the final requested boundary condition is satisfied. The name of the technique derives directly from its numerical execution: it’s like blindly shooting (i.e., forward propagation in time of a fake initial-value problem) where the ‘aim’ is iteratively adjusted to satisfy the target state.

5.1.1 The simple shooting technique

Suppose one wants to solve the system of n ordinary differential equations described in (5.1), subjected to general non-linear boundary condition (5.2). The simple shooting method requires the same dynamical system to be solved as a common initial value problem, where some components of the initial condition are unknown. Let \mathbf{s} be the collection of both known and unknown components of the initial condition.

$$\begin{cases} \dot{\mathbf{x}} = \mathbf{f}(\mathbf{x}, t) & t \in [t_a, t_b] \\ \mathbf{x}(t_a) = \mathbf{s} & \mathbf{s} \in \mathbb{R}^n \end{cases} \quad (5.3)$$

The solution of the system will give $\mathbf{x}(t; \mathbf{s})$. At this point the solution must satisfy the boundary condition of the original problem, (5.2), implying:

$$\mathbf{F}(\mathbf{s}) := \mathbf{r}(\mathbf{s}, \mathbf{x}(t_b; \mathbf{s})) = 0 \quad (5.4)$$

The solution of the problem stems then from the root finding of the non-linear function $\mathbf{F} : \mathbb{R}^n \rightarrow \mathbb{R}^n$. A multi-dimensional Newton's method can be applied:

$$\mathcal{J}(\mathbf{s}^{(i)})(\mathbf{s}^{(i+1)} - \mathbf{s}^{(i)}) = -\mathbf{F}(\mathbf{s}^{(i)}) \quad (5.5)$$

where the index (i) stands for the iteration step and $\mathcal{J} \in \mathbb{R}^{n \times n}$ is the Jacobian of \mathbf{F} .

$$\mathcal{J}(\mathbf{s}^{(i)}) = \left[\frac{\partial F_j(\mathbf{s})}{\partial s_k} \right]_{\mathbf{s}=\mathbf{s}^{(i)}} \quad (5.6)$$

Carefully applying the differentiation chain rule and the properties of the gradient, it is easy to show that the Jacobian sees the contribution of two parts:

$$\mathcal{J}(\mathbf{s}) = \mathcal{D}_{\mathbf{s}} \mathbf{r}(\mathbf{s}, \mathbf{x}(t_b; \mathbf{s})) + \mathcal{D}_{\mathbf{x}} \mathbf{r}(\mathbf{s}, \mathbf{x}(t_b; \mathbf{s})) \mathcal{Z}(t_b; \mathbf{s}) \quad (5.7)$$

where

$$\mathcal{D}_{\mathbf{u}} \mathbf{r}(\mathbf{u}, \mathbf{v}) = \left[\frac{\partial r_j(\mathbf{u}, \mathbf{v})}{\partial u_k} \right] \quad (5.8)$$

$$\mathcal{D}_{\mathbf{v}} \mathbf{r}(\mathbf{u}, \mathbf{v}) = \left[\frac{\partial r_j(\mathbf{u}, \mathbf{v})}{\partial v_k} \right] \quad (5.9)$$

$$\mathcal{Z}(t_b; \mathbf{s}) = \mathcal{D}_{\mathbf{s}} \mathbf{x}(t_b; \mathbf{s}) = \left[\frac{\partial x_j(t_b; \mathbf{s})}{\partial s_k} \right] \quad (5.10)$$

Note that the Jacobian of the boundary condition must be calculated at each iteration step, this operation is the most time-consuming step in the method. The problem of the calculation of the Jacobian is a double one in the sense that, not only it might seriously affect the computational efficiency of the whole technique, its analytical form may even be unknown and some numerical approximation must therefore be used. Among the most common is approximating the Jacobian by means of a forward finite difference scheme. Thus, \mathcal{J} will be approximated by the matrix:

$$\mathcal{J}(\mathbf{s}) \simeq \left[\frac{\mathbf{F}(s_1, \dots, s_j + \Delta s_j, \dots, s_n) - \mathbf{F}(s_1, \dots, s_j, \dots, s_n)}{\Delta s_j} \right] \quad (5.11)$$

This calculation requires $\mathbf{F}(s_1, \dots, s_j + \Delta s_j, \dots, s_n)$ to be determined through the solution of the corresponding initial-value problems. For the sake of generality, another common way of calculating the Jacobian is by solving the n^2

differential equations which govern the state transition matrix dynamics, coupled with the orbital dynamics.

$$\begin{aligned}\dot{\mathbf{x}} &= \mathbf{f}(\mathbf{x}) & \mathbf{x}(t_0) &= \mathbf{x}_0 \\ \dot{\Phi} &= \left[\frac{\partial \mathbf{f}}{\partial \mathbf{x}} \right] \Phi & \Phi(t_0) &= \mathcal{I}_{6 \times 6}\end{aligned}\tag{5.12}$$

For linear boundary conditions the problem somewhat simplifies, yielding:

$$\begin{aligned}\mathbf{F}(\mathbf{s}) &= \mathcal{A}\mathbf{s} + \mathcal{B}\mathbf{x}(t_b; \mathbf{s}) - \mathbf{c} \\ \mathcal{J}(\mathbf{s}) &= \mathcal{A} + \mathcal{B}\mathcal{D}_{\mathbf{s}}\mathbf{x}(t_b; \mathbf{s})\end{aligned}$$

where the second term of the Jacobian can be again calculated by means of a finite difference scheme.

In summary, the method consists of the following steps:

1. Choose a starting guess $\mathbf{s}^{(0)}$ and $\forall i = 0, 1, \dots$ perform:
 - a) determine $\mathbf{x}(t_b; \mathbf{s})$ by solving the initial-value problem (5.3) for $\mathbf{s} = \mathbf{s}^{(i)}$, and compute the function $\mathbf{F}(\mathbf{s}^{(i)}) = \mathbf{r}(\mathbf{s}^{(i)}, \mathbf{x}(t_b; \mathbf{s}^{(i)}))$;
 - b) choose sufficiently small numbers $\Delta s_j \neq 0$, $j = 1, \dots, n$, and determine $\mathbf{x}(t_b; \mathbf{s}^{(i)} + \Delta s_j \mathbf{e}_j)$, where \mathbf{e}_j indicates that for each j just the corresponding component in the vector $\mathbf{s}^{(i)}$ is modified;
 - c) compute the Jacobian by means of the forward finite difference scheme described in equation (5.11) and solve the linear system coming from the Newton's method application; a proper factorisation of the Jacobian might be used to speed up the numerical inversion.
2. The method is terminated when the correction applied by the Newton's method, $\Delta \mathbf{s}^{(i)} = \mathbf{s}^{(i+1)} - \mathbf{s}^{(i)}$, goes beneath a selected tolerance, or when a maximum number of iterations is reached.

In each step of the method the solution of $n + 1$ initial value problems and of a n^{th} order system of linear equations is required. Reminding the convergence properties of the Newton's method, the simple shooting technique cast in this form may diverge accordingly to the trustworthiness of the initial guess solution, $\mathbf{s}^{(0)}$, that of course is not known a priori.

The self-evident and strong dependance of the initial value problem solution from its initial condition, \mathbf{s} , together with the increase of the time interval, seriously impairs the practical utility of the simple shooting method.

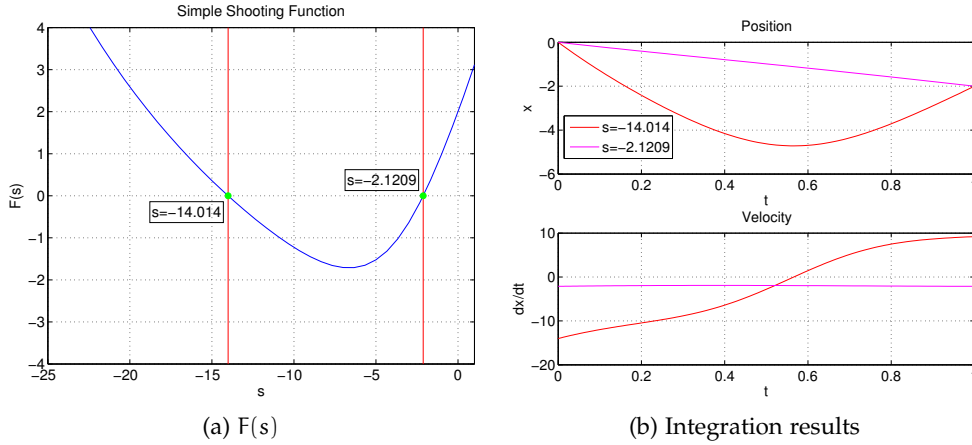


Figure 5.1: Example of a simple shooting

EXAMPLE In this paragraph an example of the application of the simple shooting method for a simple non-linear ordinary second order differential equation is shown.

$$\begin{cases} \ddot{x} + 0.34\dot{x} - 1.4x = 0.1(x^4 + \dot{x}^2) \\ x(0) = 0 \\ x(1) = -2 \end{cases}$$

It turns out that the function the Newton's method has to find the root of, possesses 2 real roots in the interval of interests. There are hence 2 possible initial conditions on the velocity that respect the boundary value problem. In Figure 5.1 the numerical results are plot for clarity of comparison.

5.1.2 The multiple shooting method

The multiple shooting method can be seen as the generalisation of the simple shooting, where the independent variable domain t is divided in $m - 1$ subintervals with a proper discretisation strategy. The idea underlying this technique is to apply simultaneously in each time subinterval a simple shooting technique and requiring the solution of the discretised differential problem to be piecewise continuous up to a selected tolerance. To this aid the time interval is divided into:

$$t_0 = t_1 < t_2 < \dots < t_m = t_f \quad (5.13)$$

The general boundary value problem

$$\begin{cases} \dot{\mathbf{x}} = \mathbf{f}(\mathbf{x}, t) \\ \mathbf{r}(\mathbf{x}(t_0), \mathbf{x}(t_f)) = 0 \end{cases} \quad (5.14)$$

is solved in the new time grid subjected to initial condition of the form

$$\mathbf{x}(t_k) = \mathbf{s}_k \quad k = 1, \dots, m-1 \quad (5.15)$$

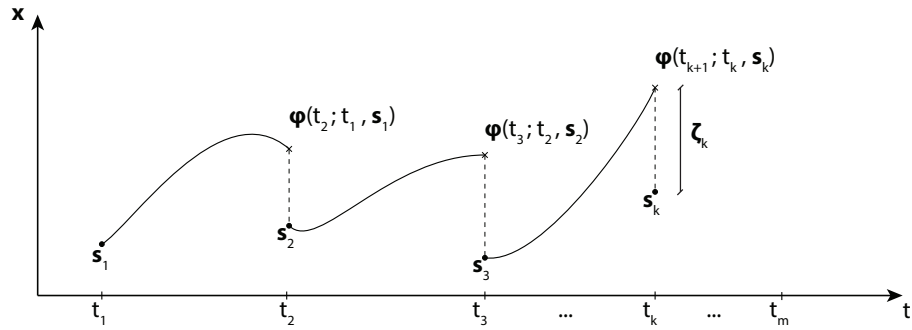


Figure 5.2: Multiple shooting strategy and defects vector

The problem is then to determine the vectors \mathbf{s}_k , $k = 1, \dots, m$, such that the function

$$\begin{aligned} \mathbf{x}(t) &= \mathbf{x}(t; t_k, \mathbf{s}_k) \quad \text{for } t \in [t_k, t_{k+1}); \quad k = 1, \dots, m-1 \\ \mathbf{x}(t_f) &= \mathbf{s}_m \end{aligned} \quad (5.16)$$

is continuous and satisfies the boundary condition of the differential problem (5.14). At each time subinterval the corresponding initial value problem is solved, the difference between its flux at the right boundary and the expected, or guessed, solution is the *defect*. The multiple shooting strategy is schematically represented in Figure 5.2. Requiring the function to be continuous yields to $m(m-1)$ conditions, namely all the defects must be null, or at least below a certain tolerance, and the boundary condition must be respected.

$$\varphi(t_{k+1}; t_k, \mathbf{s}_k) - \mathbf{s}_{k+1} = 0 \quad \forall k = 1, \dots, m-1 \quad (5.17a)$$

$$\mathbf{r}(\mathbf{s}_1, \mathbf{s}_m) = 0 \quad (5.17b)$$

The first equation represents $(m-1)$ conditions that force the piecewise function to be continuous at the boundaries of each subinterval; the second equation underlines the respect of the general nonlinear boundary condition. The unknowns of the problem are $m(m-1)$ components of the vectors \mathbf{s}_k , $k = 1, \dots, m$.

The conditions in equation (5.17) can be expressed in a more compact way, by properly defining the unknown and defects vectors.

$$\mathbf{F}(\mathbf{s}) := \begin{bmatrix} \mathbf{F}_1(\mathbf{s}_1, \mathbf{s}_2) \\ \mathbf{F}_2(\mathbf{s}_2, \mathbf{s}_3) \\ \vdots \\ \mathbf{F}_{m-1}(\mathbf{s}_{m-1}, \mathbf{s}_m) \\ \mathbf{F}_m(\mathbf{s}_1, \mathbf{s}_m) \end{bmatrix} = \begin{bmatrix} \zeta_1 \\ \zeta_2 \\ \vdots \\ \zeta_{m-1} \\ \mathbf{r}(\mathbf{s}_1, \mathbf{s}_m) \end{bmatrix} = 0 \quad \text{and} \quad \mathbf{s} = \begin{bmatrix} \mathbf{s}_1 \\ \vdots \\ \mathbf{s}_k \\ \vdots \\ \mathbf{s}_m \end{bmatrix} \quad (5.18)$$

where

$$\zeta_k = \varphi(t_{k+1}; t_k, \mathbf{s}_k) - \mathbf{s}_{k+1} \quad k = 1, \dots, m-1 \quad (5.19)$$

Note that $\mathbf{s} \in \mathbb{R}^{nm}$ and $\mathbf{F}(\mathbf{s}) : \mathbb{R}^{nm} \rightarrow \mathbb{R}^{nm}$.

Again, the zero of the nonlinear function $\mathbf{F}(\mathbf{s})$ is sought and the Newton's method can be applied directly to (5.18). The numerical technique requires of course the Jacobian of the function $\mathbf{F}(\mathbf{s})$. Thanks to the fact that each defect depends solely on the subinterval boundary values, the Jacobian will result in a block diagonal matrix, except for the last rows which depend instead on the boundary condition the problem is subjected to.

$$\mathcal{J}(\mathbf{s}) = \begin{bmatrix} \Phi_1 & -\mathcal{I}_{n \times n} & 0 & & 0 \\ 0 & \Phi_2 & -\mathcal{I}_{n \times n} & \ddots & \\ \ddots & \ddots & \ddots & \ddots & 0 \\ 0 & & \ddots & \Phi_{m-1} & -\mathcal{I}_{n \times n} \\ \mathcal{A} & 0 & \dots & & \mathcal{B} \end{bmatrix} \quad (5.20)$$

where:

$$\Phi_k = \mathcal{D}_{\mathbf{s}_k} \mathbf{F}_k(\mathbf{s}) = \mathcal{D}_{\mathbf{s}_k} \varphi(t_{k+1}; t_k, \mathbf{s}_k) \quad k = 1, \dots, m-1 \quad (5.21)$$

$$\mathcal{A} = \mathcal{D}_{\mathbf{s}_1} \mathbf{r}(\mathbf{s}_1, \mathbf{s}_m) \quad (5.22)$$

$$\mathcal{B} = \mathcal{D}_{\mathbf{s}_m} \mathbf{r}(\mathbf{s}_1, \mathbf{s}_m) \quad (5.23)$$

The matrices which form the diagonal of the Jacobian are the *State Transition matrices* of the differential problems in each time subdomain. These matrices can be calculated, as done in the preceding section, by means of a forward finite difference method scheme; note that in this way at each iteration step $n(m-1)$ additional initial value problems must be solved numerically (i.e., n each state transition matrix). At this point it is evident the computational effort of this technique.

The Newton's method can be applied to provide the following iteration step (i):

$$\mathcal{J}(\mathbf{s}^{(i)})\Delta\mathbf{s} = -\mathbf{F}(\mathbf{s}^{(i)}) \quad \text{where} \quad \Delta\mathbf{s} = \mathbf{s}^{(i+1)} - \mathbf{s}^{(i)} \quad (5.24)$$

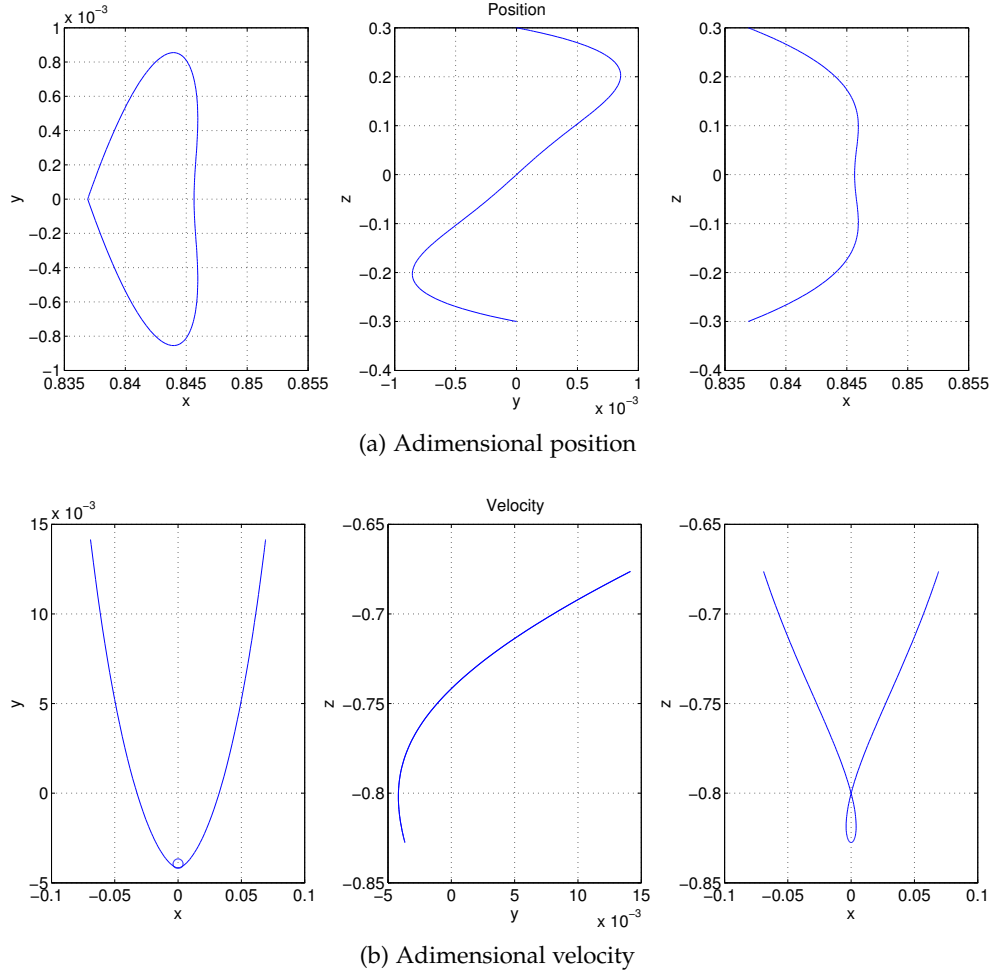


Figure 5.3: Solution of a Lambert problem trajectory with the multiple shooting method

COMPARISON In order to let the reader understand the difference between the simple and multiple shooting method a simple Lambert's problem is solved in the framework of the RTBP. Equations (2.33) are solved in the Earth-Moon system case for the following boundary conditions:

$$\begin{aligned} \mathbf{x}(t_0) &= [x_{L_1}, 0, 0.3]^T & t_0 &= 0 \\ \mathbf{x}(t_f) &= [x_{L_1}, 0, -0.3]^T & t_f &= \frac{\pi}{4} \end{aligned} \quad (5.25)$$

The time lapse chosen corresponds to one eighth of the lunar period around the Earth, that's roughly 3.5 days.

Table 5.1: Shooting techniques results for a RTBP example

Method	Iterations	Error	Machine Time [sec]
Simple Shooting	42	3.174870e-13	5.333757
Multiple Shooting	6	2.729287e-15	2.012456

In Figure 5.3 the integration results are shown. In order to converge towards the same trajectories, the two methods have been started with the same initial seed, a cosine function, set a tolerance error of $1e - 12$, corresponding to 15 cm, and maximum iterations of 45. Note how the spacecraft plenty exploits the dynamic the three-dimensional space to reach the goal.

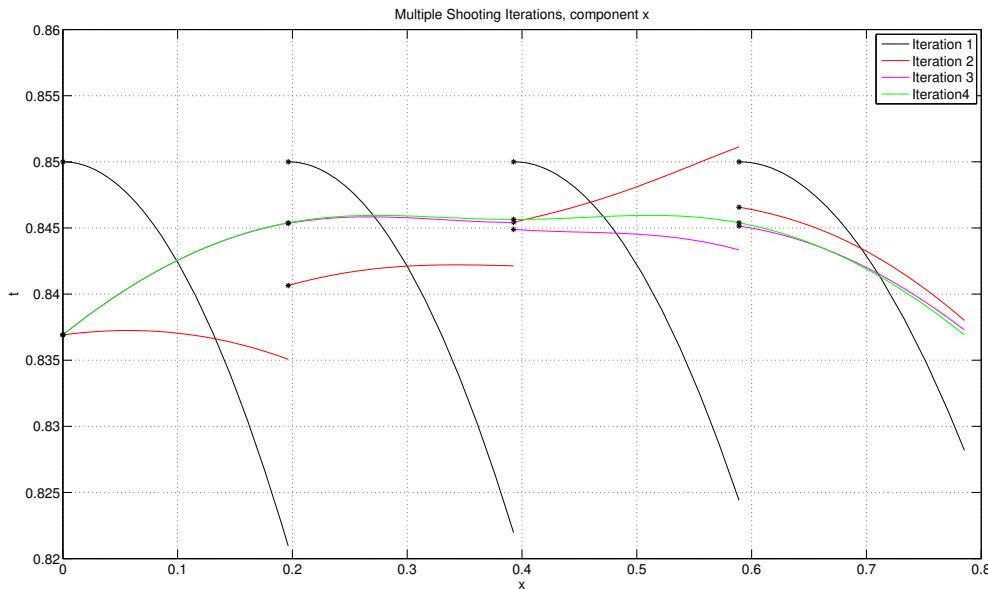


Figure 5.4: Iterations of the multiple shooting method for the component x of the Lambert problem trajectory

In Figure 5.4 the first four iterations of the multiple shooting method for the example presented are shown. It is patent the convergence rapidity of the method, even started with a poor seed function.

5.2 THE TRAJECTORY REFINEMENT ALGORITHM

The primary objective of this work is to refine trajectories, calculated within the framework of a simplified gravitational model (i. e., the CRTBP), in the real

ephemeris n-body problem. The refinement procedure, inspired by Lian et al. [29], is achieved by means of an iterative algorithm that consists of three main steps: *evaluation of a compliant initial seed orbit*, *modified multiple shooting*, and *interpolation-extrapolation of the nodes by Fourier analysis*.

The combination of the multiple shooting with the Fourier analysis allows the determination of more accurate seeding points when increasing the covered time span in the shooting procedure. The need for such cumbersome technique arises because of the large sensitivity of the multiple shooting when solving for the real dynamics. The adjective modified has been used together with multiple shooting because the TPBVP is formulated in a slightly different fashion. That is, the technique has to cope with the fact that no boundary conditions are actually known, and the sole requirement is to produce a piecewise continuous trajectory which stays as ‘close’ as possible in phase space to the initial seed. In order to attain this, the multiple shooting is coupled with an optimisation, tackled here in two ways. In the first place, the classical optimal problem is translated into a *non-linear programming* (often termed NLP) method by means of direct transcription of the dynamics and the problem is then solved for a finite set of variables when a proper objective function is specified (see Betts [7] and Conway [10] for more details). In details, a NLP problem is a decisional problem concerning a scalar algebraic function and an algebraic vector of constraints. As opposite to the optimal control problem, no dynamics is involved into a NLP problem, because in this case the dynamics is merely seen as a constraint that the NLP must satisfy. The second approach is to solve the matching non-linear equations (corresponding to the constraints) using a Newton method, in which the norm of the correction is minimised at each step. In this case the linear system that must be solved for the computation of the corrections is well-conditioned. As far as the Fourier analysis is concerned, the most general approach is the collocation procedure described in the Appendix, B.3. However, for the sake of computational efficiency, the interpolation is carried out here through another optimisation. The sum of the quadratic distances of each node from the trigonometric approximated polynomial, whose unknown are the amplitudes, is minimised. The frequencies are estimated looking at the maxima of its Fourier transform. This method might produce slightly inaccurate results; nonetheless, they will be not the final solution, instead they are used as initial seeds to for the shooting, and do not impair the results.

The whole iterative procedure invokes three functional components. A more detailed description requires the introduction of some notation. Let T_0 be the initial epoch, which should be specified due to the non-autonomous nature of the n-body problem, ΔT the time-span covered by a certain set of nodes, ΔT_0 the time-span considered for the initial guess provided by the RTBP, and ΔT^* the final time-span it is desired to achieve. N denotes the number of nodes, and N_{\min} the minimum number of nodes required by the Fourier analysis to

be consistent. During the process, either a ratio γ_P is used to enlarge ΔT at each step, $\Delta T = \gamma_P \Delta T$, or a constant time step δT is added to the previous one, $\Delta T = \delta T + \Delta T$. It is obvious that the former way needs less iterations and is then computationally more efficient.

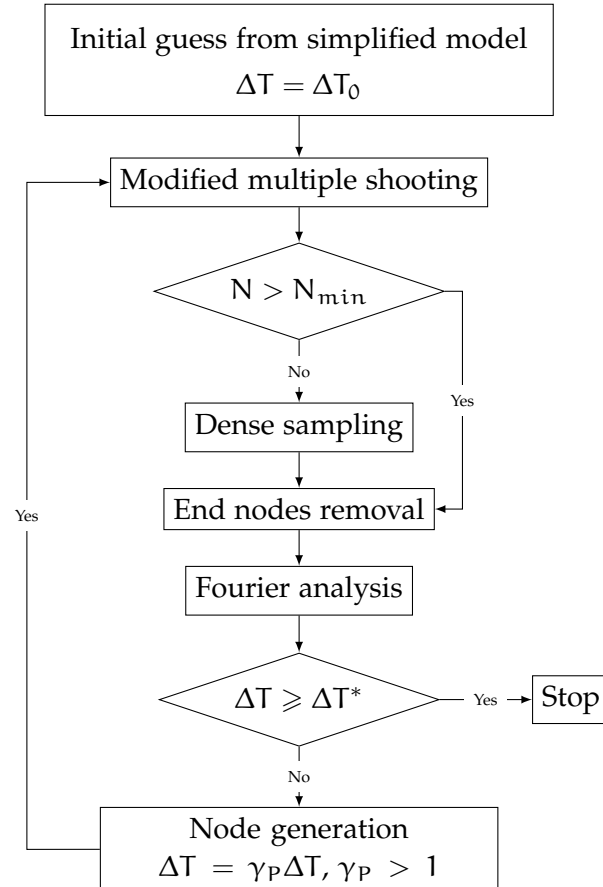


Figure 5.5: Flux diagram of the iterative algorithm for orbits refinement

The basic procedure for trajectories refinement in the n -body problem is shown as flux diagram in Fig. 5.5 and consists basically of the following steps:

- STEP 1** Using a simplified gravitational model, generate a sequence of nodes as initial guess for *Step 2*;
- STEP 2** Fix the initial epoch, T_0 , and for a given time-span ΔT , perform the modified multiple shooting with the initial guess;
- STEP 3** If $N < N_{min}$, do a denser sampling using the sequence of nodes obtained in *Step 2* by numerical piecewise integration;
- STEP 4** At both ends of the resulting sequence, remove some nodes to cope with the fact that no boundary conditions are required in the shooting method;

STEP 5 Do the Fourier analysis of the six state components of the trajectory computed in *Step 4*. With the set of basic frequencies, compute the amplitudes of the trigonometric approximation polynomial of the orbit;

STEP 6 Check the total time-span condition: if $\Delta T \geq \Delta T^*$, go to *Step 8*, otherwise, go to *Step 7*;

STEP 7 Extrapolate the new set of nodes as initial guess for a larger time-span $\Delta T = \gamma_P \Delta t$, $\gamma_P > 1$, using the trigonometric approximations of the coordinates computed in *Step 5*; then go to *Step 2*;

STEP 8 Stop.

The multiple shooting procedure is performed in a parallel fashion, due to its high computational demand. In particular, the Copernicus workstation at Politecnico di Milano has been used together with the Matlab® parallel toolbox. A maximum of 12 processors have been exploited, due to license limitations on the Matlab® platform software.

5.2.1 The modified multiple shooting

Here the problem is addressed of modifying the classic multiple shooting so as to deal with free boundary conditions. The fundamental principles in the classical shooting technique are preserved, and eventually the zero of a non-linear multi-variable function have to be found by Newton method. In particular, the vectorial function (5.18) is deprived of the last row, representing exactly the boundary condition. The new function contains only the defects vector and is termed $\mathbf{c}(\mathbf{s})$.

$$\mathbf{c}(\mathbf{s}) := \begin{bmatrix} \mathbf{c}_1(\mathbf{s}_1, \mathbf{s}_2) \\ \mathbf{c}_2(\mathbf{s}_2, \mathbf{s}_3) \\ \vdots \\ \mathbf{c}_{m-1}(\mathbf{s}_{m-1}, \mathbf{s}_m) \end{bmatrix} = \begin{bmatrix} \zeta_1 \\ \zeta_2 \\ \vdots \\ \zeta_{m-1} \end{bmatrix} = \mathbf{0} \quad \text{and} \quad \mathbf{s} = \begin{bmatrix} \mathbf{s}_1 \\ \vdots \\ \mathbf{s}_k \\ \vdots \\ \mathbf{s}_m \end{bmatrix} \quad (5.26)$$

where the defect vectors are those describe in Eq. (5.19). Note that, for the n -body problem, $\mathbf{c}(\mathbf{s}) : \mathbb{R}^{6m} \rightarrow \mathbb{R}^{6(m-1)}$ and $\mathbf{s} \in \mathbb{R}^{6m}$. The problem is to seek the zero of the function

$$\mathbf{c}(\mathbf{s}) = \mathbf{0} \quad (5.27)$$

The problem cast in this form possesses $6m$ degrees of freedom, whilst Eq. (5.27) provides just $6(m-1)$ conditions; 6 equations are therefore missing to

properly define the problem. An optimisation procedure shall be implemented in order to shatter the underdetermination.

In the subsequent derivation the need for the Jacobian of the function \mathbf{c} , \mathcal{J}_c , will arise.

$$\mathcal{J}_c(\mathbf{s}) = \begin{bmatrix} \Phi_1 & -\mathcal{I}_{n \times n} & 0 & & & 0 \\ 0 & \Phi_2 & -\mathcal{I}_{n \times n} & \ddots & & \\ \ddots & \ddots & \ddots & & & 0 \\ 0 & & \ddots & \Phi_{m-1} & -\mathcal{I}_{n \times n} \end{bmatrix} \in \mathbb{R}^{6(m-1) \times 6m} \quad (5.28)$$

where the state transition matrices, Φ_k , are given by (5.21).

As stated above, the first approach deals with the constrained minimisations of a scalar functional in the sense of non-linear programming. Thus, a carefully chosen scalar objective function is minimised, subjected to constraints that play the role of the dynamics. Let $f(\mathbf{s}) : \mathbb{R}^{6m} \rightarrow \mathbb{R}^1$ be the objective function, then the minimisation problem can be stated as:

$$\min_{\mathbf{s}} f(\mathbf{s}) \quad \text{subject to} \quad \mathbf{c}(\mathbf{s}) = 0 \quad (5.29)$$

From simple theory of calculus variations (see Gelfand and Fomin [16]), the problem can be solved introducing the *Lagrange multipliers*. Let $\lambda \in \mathbb{R}^{6(m-1)}$ be the vector of $6(m-1)$ multipliers, then the minimisation problem is formally equivalent to minimise an augmented performance index:

$$\mathcal{L}(\mathbf{s}, \lambda) = f(\mathbf{s}) + \lambda^T \mathbf{c}(\mathbf{s}) \quad (5.30)$$

The problem consists now in formulating the necessary condition for a stationary point of the Lagrangian function; this is achieved by imposing that its first variation is zero, namely $\delta \mathcal{L} = 0$.

Applying the variations for \mathbf{s} and the multipliers λ to the Lagrangian function:

$$\begin{aligned} \nabla_{\mathbf{s}} \mathcal{L} &= \mathbf{g} + \mathcal{J}_c^T \lambda = 0 \\ \nabla_{\lambda} \mathcal{L} &= \mathbf{c} = 0 \end{aligned} \quad (5.31)$$

where \mathbf{g} is the gradient of the objective function, $\mathbf{g} = \nabla_{\mathbf{s}} f(\mathbf{s})$. Note that the second equation is again the respect of the dynamics in a NLP sense. The system (5.31) is non-linear in the variables \mathbf{s} and λ ; a Newton method shall hence applied to calculate its zero. Let

$$\mathbf{y} = \begin{pmatrix} \mathbf{c} \\ \boldsymbol{\lambda} \end{pmatrix} \quad \Psi = \begin{pmatrix} \mathbf{g} + \mathcal{J}_c^T \boldsymbol{\lambda} \\ \mathbf{c} \end{pmatrix}$$

be the new independent variable and function whose zero is sought, $\Psi(\mathbf{y})$, respectively; then, in order to apply the Newton method, the gradient of the function Ψ must be provided.

$$\nabla_{\mathbf{y}} \Psi(\mathbf{y}) = \begin{bmatrix} \mathcal{H}_{\mathcal{L}} & \mathcal{J}_c^T \\ \mathcal{J}_c & 0_{6(m-1) \times 6(m-1)} \end{bmatrix} \quad (5.32)$$

where $\mathcal{H}_{\mathcal{L}}$ is the Hessian of the Lagrangian with respect to \mathbf{s} , defined as:

$$\mathcal{H}_{\mathcal{L}} = \nabla_{\mathbf{s}}(\mathbf{g} + \mathcal{J}_c^T \boldsymbol{\lambda}) = \nabla_{\mathbf{s}}^2 f + \sum_{i=1}^{m-1} \lambda_i \nabla_{\mathbf{s}}^2 c_i \quad (5.33)$$

Provided a generic initial guess $\mathbf{y}^{(0)}$, the corrections to construct the solution at a subsequent step, are given by solving the linear system

$$\begin{bmatrix} \mathcal{H}_{\mathcal{L}} & \mathcal{J}_c^T \\ \mathcal{J}_c & 0 \end{bmatrix} \begin{pmatrix} \Delta \mathbf{s} \\ \boldsymbol{\lambda}^{(i+1)} \end{pmatrix} + \begin{pmatrix} \mathbf{g}(\mathbf{s}^{(i)}) \\ \mathbf{c}(\mathbf{s}^{(i)}) \end{pmatrix} = 0 \quad (5.34)$$

where $\Delta \mathbf{s} = \mathbf{s}^{(i+1)} - \mathbf{s}^{(i)}$. The term $\mathcal{J}_c^T \boldsymbol{\lambda}$ has been dropped in the first element of the known vector because the variation of $\boldsymbol{\lambda}$ has been dropped as well, retaining only the term $\boldsymbol{\lambda}^{(i+1)}$. The linear system (5.34) is often referred as *Karush-Huhn-Tucker system*. Observe that an equivalent way to define a search direction $\Delta \mathbf{s}$ is to minimise the quadratic form

$$\min_{\Delta \mathbf{s}} \frac{1}{2} \Delta \mathbf{s}^T \mathcal{H}_{\mathcal{L}} \Delta \mathbf{s} + \mathbf{g}^T \Delta \mathbf{s} \quad \text{subject to} \quad \mathcal{J}_c \Delta \mathbf{s} = -\mathbf{c}$$

It is noteworthy that in this case the constraint is linear. This is the reason why this problem is also referred as a quadratic programming (QP) problem.

Due to its desirable properties, a convenient selection of the objective function is a quadratic form of the constraint function itself:

$$f(\mathbf{s}) = \frac{1}{2} \mathbf{c}^T \mathcal{M} \mathbf{c} \quad \Rightarrow \quad \mathbf{g} = \frac{1}{2} \mathcal{J}_c^T (\mathcal{M} + \mathcal{M}^T) \mathbf{c}$$

The matrix $\mathcal{M} \in \mathbb{R}^{6m \times 6m}$ can be chosen to weigh in a different manner the contribution of each state. It is desirable this matrix to be non-singular (i. e.,

$\det \mathcal{M} \neq 0$). The difficulty of the whole method probably resides in the discrete computation of the constraint Hessian, $\mathcal{H}_{\mathcal{L}}$.

The second way of solving the problem (5.27) is to apply directly the Newton method and to ask an optimisation procedure to minimise the corrections that each step exerts to the state. In this case the convergence is still assured and the resulting linear system is well-defined. The main drawback is the sensible increase of iterations needed to satisfy a certain tolerance threshold. The direct application of the Newton method yields:

$$\mathcal{J}_c(\mathbf{s}^{(i)})\Delta\mathbf{s} + \mathbf{c}(\mathbf{s}^{(i)}) = 0 \quad \Delta\mathbf{s} = \mathbf{s}^{(i+1)} - \mathbf{s}^{(i)} \quad (5.35)$$

This is a linear set of underdetermined equations. In this case the problem is overcome by minimising a quadratic form of the Newton method corrections at each step, weighed by a matrix \mathcal{M} with the same properties of the first approach. The constraint vector is the equation of the Newton method at step (i). As before, the formalism of the Lagrangian multipliers is introduced and the Lagrangian function reads:

$$\mathcal{L}(\Delta\mathbf{s}, \boldsymbol{\lambda}) = \frac{1}{2}\Delta\mathbf{s}^T \mathcal{M} \Delta\mathbf{s} + \boldsymbol{\lambda}^T [\mathcal{J}_c(\mathbf{s}^{(i)})\Delta\mathbf{s} + \mathbf{c}(\mathbf{s}^{(i)})] \quad (5.36)$$

The conditions for null variation yield:

$$\begin{aligned} \nabla_{\Delta\mathbf{s}} \mathcal{L} &= \frac{1}{2}(\mathcal{M} + \mathcal{M}^T)\Delta\mathbf{s} + \mathcal{J}_c^T(\mathbf{s}^{(i)})\boldsymbol{\lambda} = 0 \\ \nabla_{\boldsymbol{\lambda}} \mathcal{L} &= \mathcal{J}_c(\mathbf{s}^{(i)})\Delta\mathbf{s} + \mathbf{c}(\mathbf{s}^{(i)}) = 0 \end{aligned} \quad (5.37)$$

As usual for problems of this kind, the constraint equation appears again in the variation. This linear system can be solved for $\Delta\mathbf{s}$ and $\boldsymbol{\lambda}$. After some simple mathematical manipulations:

$$\begin{aligned} \boldsymbol{\lambda} &= \frac{1}{2}[\mathcal{J}_c(\mathcal{M} + \mathcal{M}^T)^{-1}\mathcal{J}_c^T]^{-1}\mathbf{c} \\ \Delta\mathbf{s} &= -(\mathcal{M} + \mathcal{M}^T)^{-1}\mathcal{J}_c^T[\mathcal{J}_c(\mathcal{M} + \mathcal{M}^T)^{-1}\mathcal{J}_c^T]^{-1}\mathbf{c} \end{aligned} \quad (5.38)$$

The advantage of this approach is that it is easily implemented and possesses a straightforward quasi-analytical form. The exception is course the computation of the Jacobian, \mathcal{J}_c , common factor of all methods.

5.3 DYNAMICAL SUBSTITUTES OF LIBRATION POINTS

As explained in preceding sections, the solar system restricted n-body equations of motion are non-autonomous, and there are no relative equilibrium

points in this model. Nevertheless, they can be defined in several ways. For instance, geometrically, as the points that belong to the instantaneous primaries plane of motion and such that the distances to both primaries fulfil the same relationships as in the CRTBP. The effects of the remaining solar system bodies, as well as the generally elliptical motion of the primaries, prevent these points to be relative equilibrium ones. The dynamical substitutes of the equilibrium points are defined as those solutions of the equations of motion that have as basic frequencies only those of the perturbing bodies.

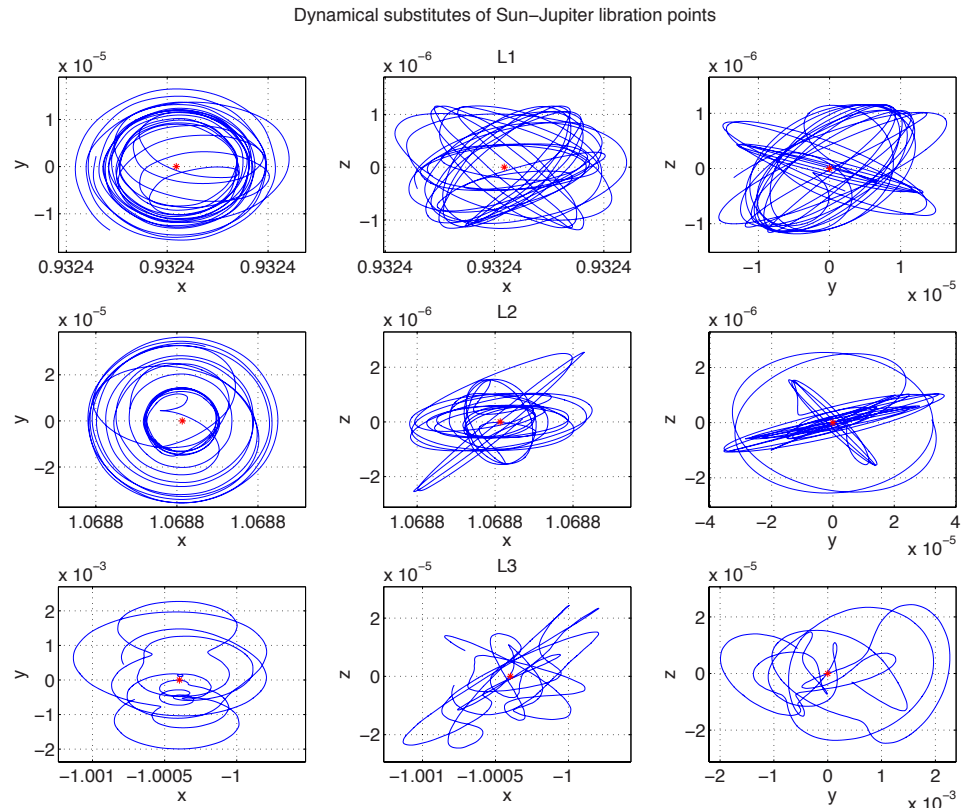


Figure 5.6: Coordinate projections of the dynamical substitutes of the L_1 (top), L_2 (middle) and L_3 (bottom) of the Sun-Jupiter system in the real ephemeris n -body dynamics (only the first 110 years of the computed orbits are displayed)

Using the numerical method described in the preceding section, dynamical substitutes of the three collinear libration points for the Sun-Jupiter, Earth-Moon and Sun-Earth systems are computed. It must be remarked that, for each point, these substitutes are not unique since they depend, for instance, on the initial epoch at which they are computed. The initial epoch has been fixed to MJD 0 in this thesis (0 UT on January 1, 2000), and for all the refinement procedures. The initial seeds used for the procedure are the three equilibrium points of the CRTBP along a certain time interval. Dynamical substitutes of the Sun-

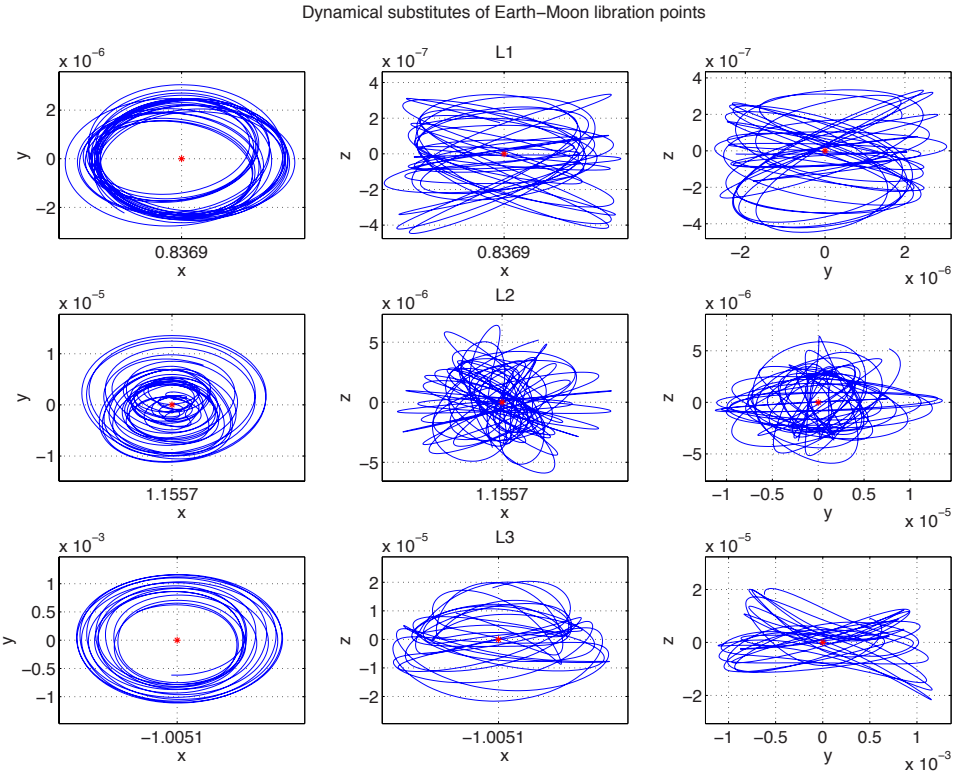


Figure 5.7: Coordinate projections of the dynamical substitutes of the L_1 (top), L_2 (middle) and L_3 (bottom) of the Earth-Moon system in the real ephemeris dynamics (1 year of computed orbits are displayed)

Jupiter collinear points have been calculated for 150 years; Earth-Moon ones for 5 years; and Sun-Earth's for a period of 20 years. The Fourier analysis for the trigonometric approximation and extrapolation polynomial has been used only in the Sun-Earth case. Indeed, this turned out to be the most difficult case the algorithm can handle, due to the high chaotic behaviour in the neighbourhood of $L_{1,2}$ of the Sun-Earth restricted three-body dynamics. In this case, to attain the convergence of the method and in order to span a large time interval, the procedure has been started with $\Delta T_0 = 2$, $\Delta T^* = 20$ (unity of mea-

Table 5.2: Approximate order of magnitude [Km] of dynamical substitutes orbits

	Sun-Jupiter	Earth-Moon	Sun-Earth
L_1	6.1371271472472e+03	0.6286745320244	1.5918748522451e+04
L_2	1.2561253618450e+04	2.0198145994667	3.0544517847013e+04
L_3	6.3489316851462e+05	2.4072623488698e+02	4.3900718438948e+04

surements is year), and $\gamma_P = 1.5$. With these parameters, 7 iterations suffice to reach the final desired time.

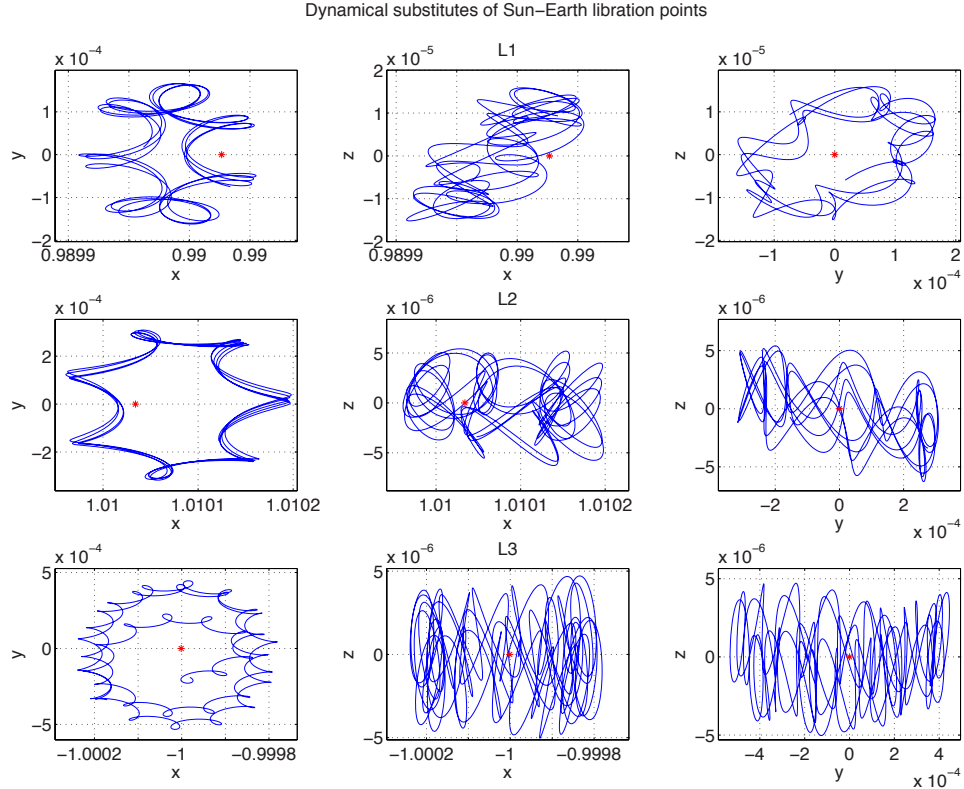


Figure 5.8: Coordinate projections of the dynamical substitutes of the L_1 (top), L_2 (middle) and L_3 (bottom) of the Sun-Earth system in the real ephemeris n -body dynamics (only the first 10 years of the computed orbits are displayed)

The resulting orbits are shown in Figures 5.6, 5.7, and 5.8 for Sun-Jupiter, Earth-Moon and Sun-Earth case, respectively. For the sake of clarity, and due to the large amount of data, only the first 10 iterations are shown, where an iteration corresponds to the primary revolution period (i.e., roughly 11 years for the Sun-Jupiter case, 1 month for Earth-Moon, and 1 year for the Sun-Earth).

These results are in agreement with those obtained by means of other methods by Gómez et al. [20], Hou and Liu [24], and Lian et al. [29]. As can be seen in Figures 5.6, 5.7, and 5.8, the sizes of the dynamical substitutes orbits are fairly small for every system. An exception is the dynamical substitutes of the Sun-Earth system, which orbit at tens of thousands of Kilometers about the collinear points. Table 5.2 displays the order of magnitude of such orbits for each gravitational system and discriminating for the collinear libration points. There is a patent increase of the dynamical substitute orbit amplitude along

with the decrease of the Jacobi constant, that is the orbit is larger for larger energy content.

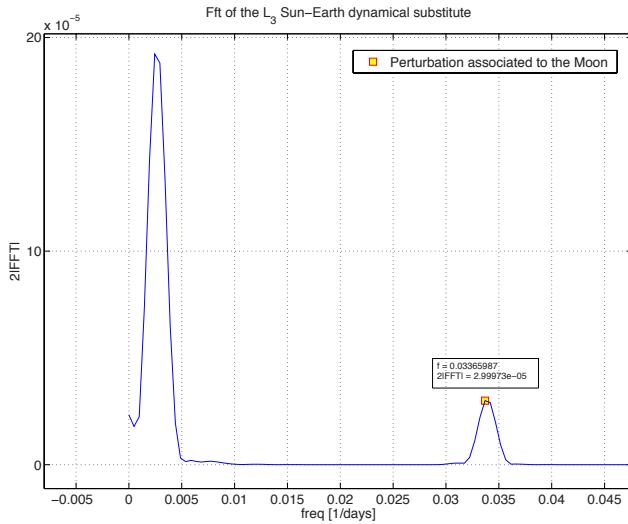


Figure 5.9: Fourier transform of the Sun-Earth L_3 dynamical substitute, x-component

As far as the Earth-Moon case is concerned, though smaller, the orbit of L_1 moves in a more ‘regular’ way (a torus-like shape) than the substitutes of L_2 and L_3 , which in some sense reflect the fact that dynamics around L_2 point is more rich and complex. Quite the contrary, the totality of Sun-Jupiter dynamical substitutes reveal a high chaotic behaviour, in particular the path around L_2 manifest the tendency to change orbital plane periodically. Last but not least, the Sun-Earth dynamical substitutes, relatively the largest in amplitude, show a clear-cut quasi-periodic behaviour. The Fourier transform of the x-component of the L_3 dynamical substitute, Figure 5.9, exhibits the contribution due to the Moon on the gravitational system. The largest peak, on the other hand, corresponds to a period of 409.5 days.

The refinement of the collinear libration points has been parallel-executed in Copernicus, the workstation of Politecnico di Milano. A typical generated output file is shown in Figure 5.10. Two values of time are displayed. Refinement time is the first value, whilst the second indicates the time needed to reintegrate the initial condition, necessary to check if consistency is attained. Namely, the optimiser output is flown under the real ephemeris dynamics, and the obtained orbit should be equal to the corresponding dynamical substitute. It happened in the course of simulations, that the specified tolerance was either too strict, or too loose. The effect was either a very slow, if at all, convergence, or errors in the dynamics that, propagated forward, gave rise to an orbit detaching the sought solution and allowed the massless particle to move far away from the libration point, according to its Jacobi energy. Another possible cause of error is the vicinity of the orbit to a bifurcation phenomenon,

Figure 5.10: Copernicus output text file for the computation of the Sun-Jupiter L₂ dynamical substitute

ascrivable for instance to the bifurcation of planar Lyapunov orbit to the halo family. During the iterations the algorithm ‘jumps’ between the two possible options and ends up refining a different kind of orbit. A curious example occurred when computing the Earth-Moon L_3 dynamical substitute for 2 years, 36 subintervals and with very strict optimisation parameters. The procedure output a Lissajous orbit featured (see Eqs. 2.72) by:

$$\begin{aligned} A_x &= 4.5e - 5 & A_z &= 8.088e - 6 \\ \phi &= -0.159627563322632 & \psi &= 1.88600760372549 \end{aligned}$$

The very same situation might occur in the refinement of halo orbits characterised by very small amplitude parameters. This occurrence should not surprise, in fact also differential corrections in the framework of CRTBP might produce a planar Lyapunov orbit when seeking a small-amplitude halo one. Figure 5.11 shows the ‘accidentally’ refined Lissajous orbit and the corresponding linearised path in the RTBP.

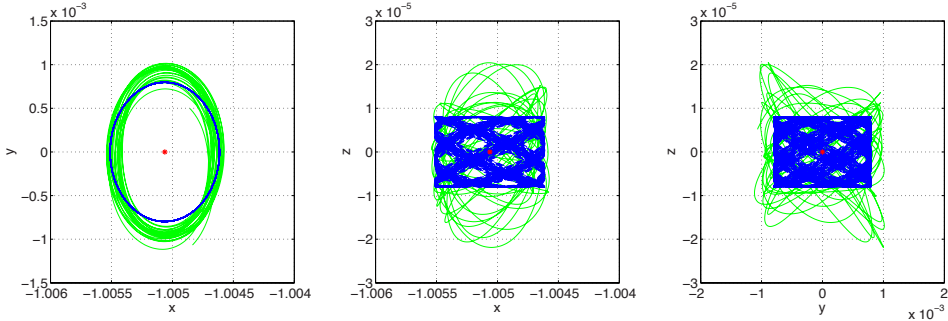


Figure 5.11: Coordinate projections of the refined Lissajous orbit of the Earth-Moon system L_3 in the real ephemeris n-body dynamics

5.4 QUASI-PERIODIC ORBITS REFINEMENT

This section is devoted to the refinement of periodic orbits around both L_1 and L_2 of the Sun-Jupiter, Earth-Moon and Sun-Earth gravitational systems; which include the halo orbits and the planar Lyapunov ones.

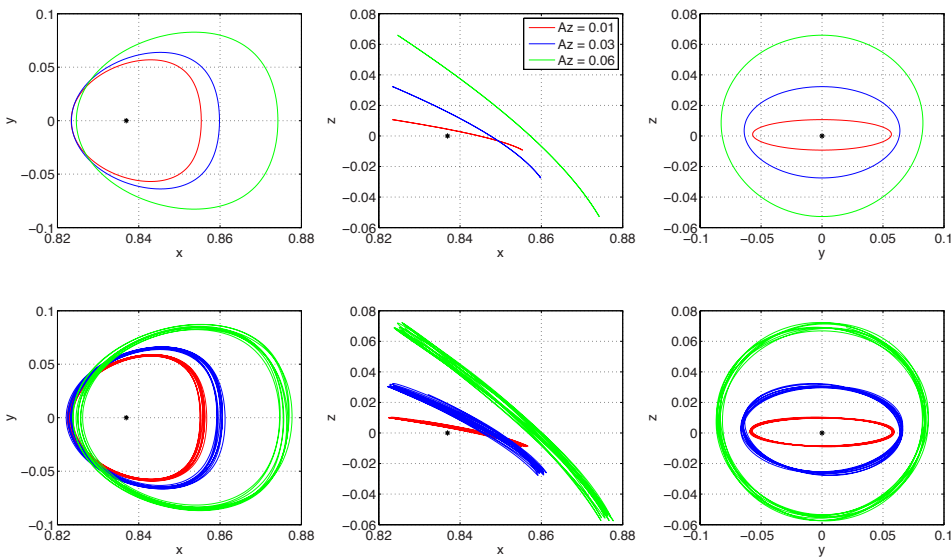


Figure 5.12: Initial CRTBP guess (top) and refinement (bottom) of halo orbits with $A_z = 0.01$ (smallest orbit), $A_z = 0.03$, and $A_z = 0.06$ (largest orbit) of the Earth-Moon L_1 libration point. Only the first year is plotted here

5.4.1 The halo family

Recalling 2.3.3, halo orbits in the CRTBP are spatial periodic solutions that bifurcate from the planar Lyapunov orbits at a given amplitude. Due to the symmetry of the problem with respect to the x-y plane, there appear two fami-

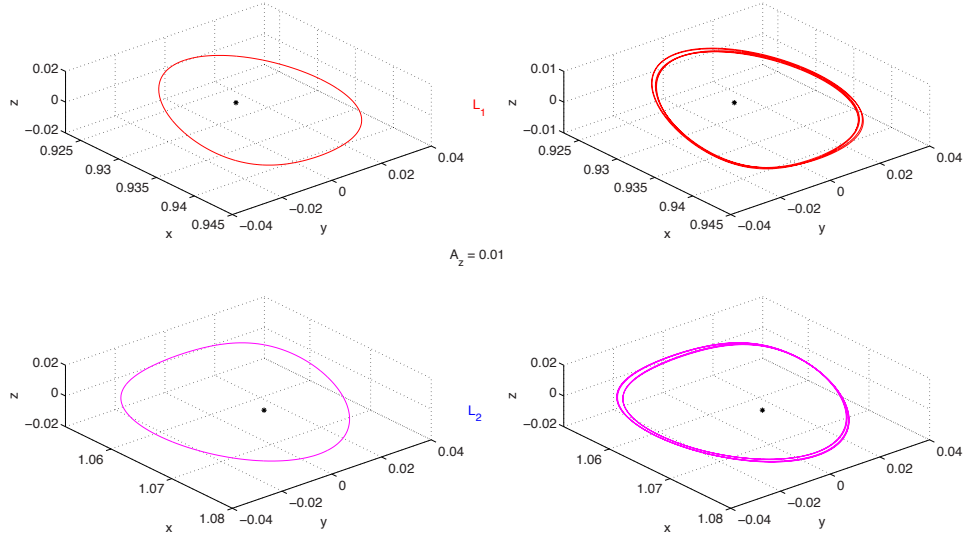


Figure 5.13: Halo orbits ($A_z = 0.01$) and their numerical 50-year refinements around L_1 (top) and L_2 (bottom) of the Sun-Jupiter gravitational system. On the left hand side the orbits of the CRTBP taken as initial seeds are shown, and on the right hand side their refinements

lies of halo orbits at the bifurcation. In the following, just the northern family¹ orbits are refined to the n-body problem dynamics. Halo orbits can be characterised by an amplitude parameter, A_z , which is the first coefficient of the Fourier expansion of the z coordinate in normalised units, in which the unit length is taken as the distance between the libration point and the small primary. Different values of A_z univocally correspond to different energy levels, and thus to different values of the Jacobi constant, C_J . In other words, given any of these two parameters, one particular halo orbit is specified.

Figure 5.12 displays the refinement of three halo orbits about the Earth-Moon first libration point, associated to three different values of the amplitude, $A_z = (0.01 \quad 0.03 \quad 0.06)$. Note that larger amplitude means larger orbital path, and therefore smaller Jacobi energy, C_J . The refinement has been done for 4 years, but for the sake of presentation clarity, only the first year is graphed. Figure 5.13 shows a three-dimensional view of the refinement operated on two halo orbits about L_1 and L_2 of Sun-Jupiter system, for a period of 50 years. Both the CRTBP halo seeds have been calculated with a fixed amplitude of $A_z = 0.01$. Finally, in Figure 5.14, two halo orbits about the Sun-Earth L_2 point are considered, whose amplitudes are $A_z = 0.002$ and $A_z = 0.005$. Again, larger amplitude corresponds to larger orbital path, and thus to a higher total energy content, E . From the obtained results and the presented figures, it is clear that the numerical refinement procedure of a halo orbit produces a quasi-

¹ Maximum z-amplitude along the positive z direction.

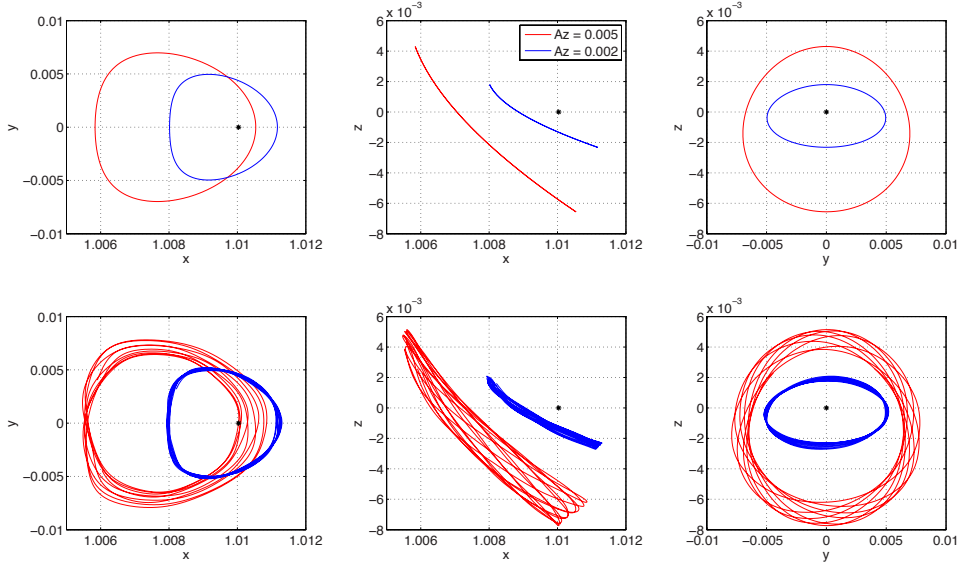


Figure 5.14: Initial CRTBP guess (top) and refinement (bottom) of halo orbits with $A_z = 0.002$ (smallest orbit), and $A_z = 0.005$ (largest orbit) of the Sun-Earth L₂ collinear point. Only the first 11 years are plotted here

periodic one, whereas the baseline shape and size do not change for most of the orbits.

A Fourier analysis of the refined halo-type orbit about Sun-Earth L₂ libration point, whose x-component is depicted in Figure 5.15, shows that the main single halo frequency is maintained. In addition, since the refined orbit is now quasi-periodic, other frequencies appear. In particular, the frequency corresponding to Mercury and the Moon are highlighted. Note that the perturbative effects of other massive planets are present, but cannot be resolved by the Fourier transform due to the limited total period (11 years).

5.4.2 The planar Lyapunov family

According to Lyapunov theorem (see Siegel et al. [38]), two Lyapunov families of periodic orbits emanate at the collinear libration points, with frequencies associated with the two purely imaginary eigenvalues of the linear part of the CRTBP vector field, as obtained in the last part of 2.3.3. The bounded solutions in the neighbourhoods of these libration points will be, in general, quasi-periodic Lissajous orbits. The planar Lyapunov orbit is located on the x-y plane, giving an in-plane motion boundary to the Lissajous orbits. The vertical Lyapunov orbit, which has zero in-plane motion, sets an out-of-plane limit for the Lissajous ones of the same energy. In this work, just planar Lyapunov orbits are objects of the refinement procedure. In particular, 5.16 displays the refinement of two planar Lyapunov orbits emanating from the first libration

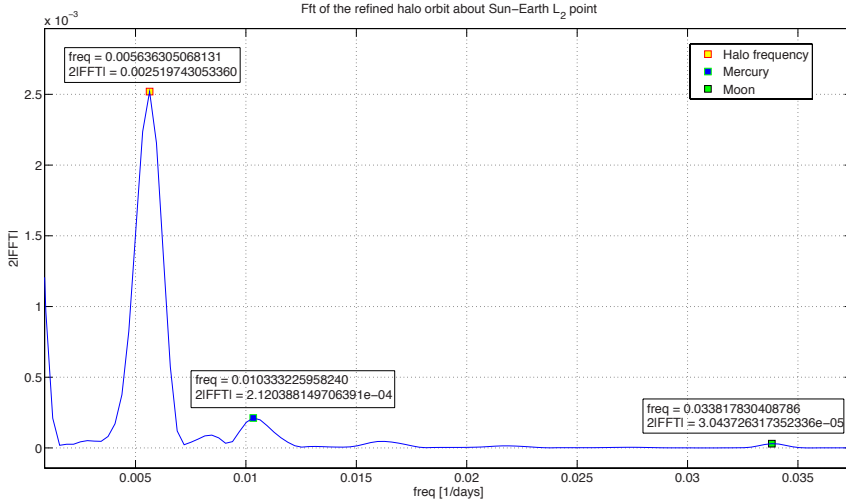


Figure 5.15: Fourier transform of the $A_z = 0.01$ halo orbit abut the L_2 of Sun-Earth gravitational system, x-component

point, L_1 , of Sun-Jupiter system. The seed orbits, calculated in the CRTBP, are characterised by two distinct values of Jacobi constant, that is $C_J = 3.02$ and $C_J = 3.039$. The iterative procedure has been started (for both orbits) with $\Delta T_0 = 4$, $\Delta T^* = 20$ (unity of measurements is year), and $\gamma_P = 1.3$. With these parameters, 7 iterations suffice to reach the final desired time. For either of the two Lyapunov families, orbits with different amplitudes are associated to different energy levels (values of the Jacobi constant); as expected, the orbit with higher C_J has smaller amplitude. In Figure 5.17 the refinement of a planar Lyapunov orbit about the Earth-Moon system second collinear point L_2 is shown. The Lyapunov orbits has Jacobi energy $C_J = 3.15$, and the numerical refinement has been done for 1 year.

From Figures 5.16 and 5.17, one can evince that, due to the gravitational perturbative effects of massive bodies unrelated to the RTBP dynamics, the refinements of the planar Lyapunov orbits are no longer on the $z = 0$ plane but they have a small amplitude oscillation along the z -direction. The frequency of this oscillation is close to the vertical frequency of the small z -amplitude Lissajous orbit, this is, to the frequency associated to the imaginary eigenvalue of the third component of the linear vector-field. Figure 5.18 depicts the Fourier transform of the z -component of the $C_J = 3.15$ Lyapunov orbit about the Earth-Moon L_2 . Lastly, although the refined orbits of both families are all quasi-periodic, the baseline shapes and sizes of the periodic orbit have sustained.

Results for orbits refined over longer time spans will be presented in a paper by the author of this thesis and Dr. Francesco Topputto later on.

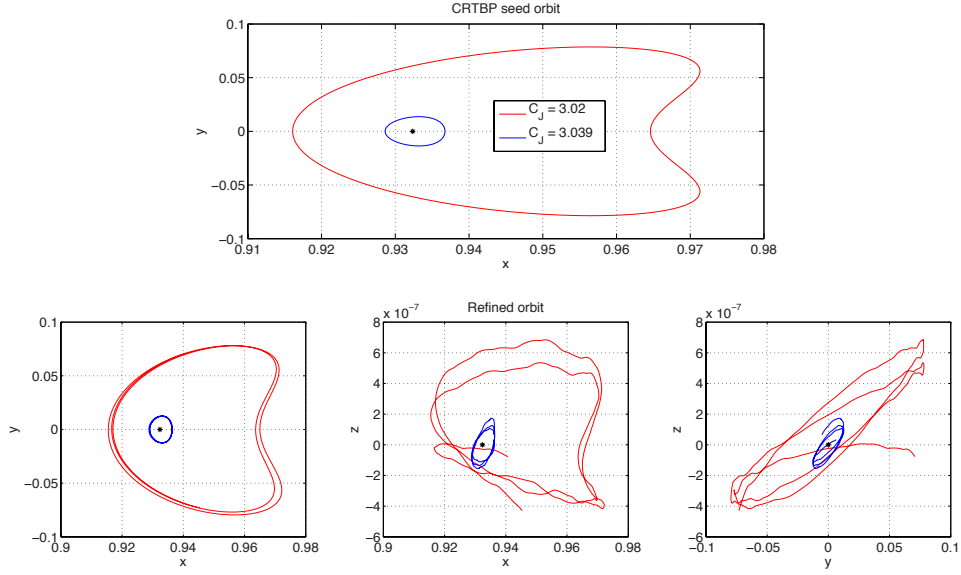


Figure 5.16: Initial CRTBP guess (top) and 20-year numerical refinement (bottom) of planar Lyapunov orbits with $C_J = 3.039$ (smallest orbit), and $C_J = 3.02$ (largest orbit) of the Sun-Jupiter L_1 libration point

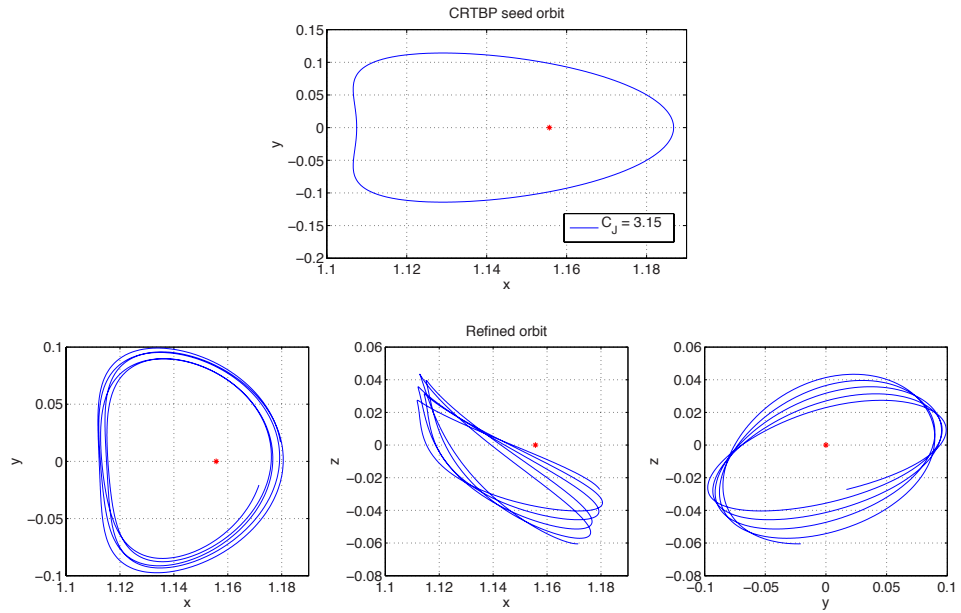


Figure 5.17: Initial CRTBP guess (top) and 1-year numerical refinement (bottom) of planar Lyapunov orbit characterised by Jacobi energy $C_J = 3.15$, of the Earth-Moon L_2 collinear point

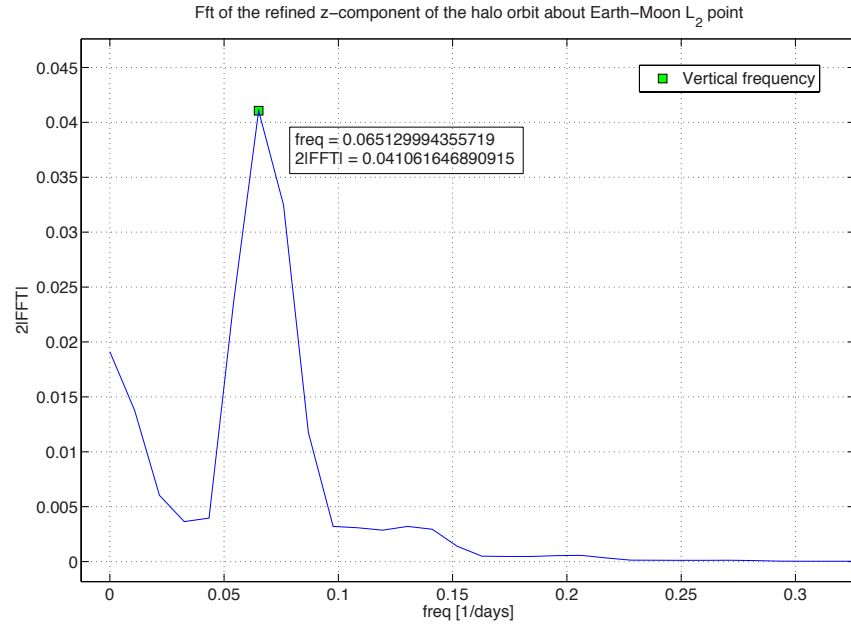


Figure 5.18: Fourier transform of the z-component of the $C_J = 3.15$ planar Lyapunov orbit abut the L_2 of Earth-Moon system

6

FINAL REMARKS

At the end of the present thesis exposition, it is worth to discuss the methodologies implemented and the results presented. Moreover, it is significant to suggest prospective work related to the study proposed.

6.1 CONCLUSIONS

The main purpose of this thesis was the development of an automatic procedure, able to refine general trajectories into the real solar system ephemeris. This problem has been studied from an engineering standpoint: the seeding orbits were calculated and designed first in a simplified gravitation model; then they were refined in the n-body problem by means of the algorithm proposed, coded in Matlab[®].

In the first chapters of the thesis, the mathematical models, useful to describe the physics associated with the astrodynamics problems of interests, have been given, along with a brief introduction on the problem at hand. Special emphasis has been put in the restricted three-body problem and in the structure of the phase space around the equilibrium points. The majority of interesting space trajectories surge indeed from this model. Writing the n-body problem as perturbation of the simpler RTBP has allowed a convenient and efficient application of a multiple shooting strategy for the refinement procedure. The optimal control problem has been introduced together with the numerical techniques used throughout the thesis. The OCP has been transcribed into a parameter optimisation problem and solved as a standard NLP problem, where the dynamics has been viewed as a constraint.

The algorithm can handle both constrained and unconstrained boundary conditions. Although the implementation has been quite cumbersome, it revealed to be appealing for complicated aerospace applications, and assured versatility and robustness. The intricacy ensued from the compatibility between ephemeris data and synodic integration. The shooting part has been addressed by means of a dedicated parallel computing strategy. The results obtained in this work make the algorithm very appealing and potentially applicable for real space applications.

Results have been sought for the dynamical substitutes of several three-body systems. Two different space applicative scenarios have been objects of particular interest: the classic problem that concerns the Earth-Moon system, and the Sun-Jupiter synodic frame, easy to disclose because of its mass preponderance in the solar system, making it minimally affected by perturbations. The analysed cases numerically demonstrate and show that quasi-periodic orbits exist in the neighbourhood of the unstable collinear points in the complete gravitational model. Thus, these orbits can be plenty exploited by a space mission in the real scenario. The drawback is that, due to the calculation requirements in terms of time and to the size of the ephemeris data into the future, these trajectories are calculated for limited periods, compatible with the synodic reference at hand.

Moreover, interesting solutions of the RTBP have been refined to the real solar system. Halo and Lissajous orbits with either prescribed amplitude or Jacobian energy for various synodic frames were computed and processed by the refinement algorithm. Their main orbital frequency components, a single one for the Halo-type trajectories, are maintained with slight variation over the years. This lead to a full quasi-periodicity, leaving the original orbital shape essentially unvaried.

Both problems, dynamical substitutes of collinear points and RTBP special orbits refinement, were treated under the same perspective: the algorithm propagates forward in time a ‘good’ initial guess by integrating in the roto-pulsating frame, and then solves the matching equations. The convergence to a general solution strongly depends on the initial seed. Finally, the methodology proposed revealed to be very flexible and robust, as they could be applied to different applicative scenarios.

6.2 PROSPECTIVE WORK

The future developments, related to the refinement in highly nonlinear astrodynamics of simplified space trajectories, can be divided into three main different paths. On one side, further investigations on the effect of perturbations is suggested. Secondly, deeper studies on the mathematical models describing the dynamics are required. In particular the algorithm should embed resonant and bifurcation behaviours, taking explicit advantage from these phenomena. Lastly, propelled interplanetary trajectories could be refined in the complete model, for instance by means of a switching synodical frame of reference.

In this thesis perturbations have been almost completely neglected. Relativistic effects are taken into account solely in the solar system barycentric integrator, but the procedure has not been adjusted to work in the non-inertial roto-pulsating frame. What is more, drag dissipation, oblateness of attractors and solar pressure should be taken into account for more a precise set of results.

As far as the chaotic nature of the restricted problem, the dynamical system theory forecasts bifurcation and resonant motion to occur in specific circumstances. This kind of events were not accounted and the shooting just forced the dynamics to be as close as possible to provided initial seed. If a bifurcation occurred, the trajectory would completely change its phase portrait; however, the algorithm will still try to seek an optimal solution. What is more, it has been demonstrated that resonant hops can lead to escapes from the synodic frame. Prospective work could be improving the code by explicitly accounting for these effects.

Interplanetary trajectories, composed by both ballistic and propelled arcs, have not been refined by the algorithm. A dedicated session should be implemented and collaboration with an already existing and designed space mission trajectory could be refined to the ephemeris model.

APPENDIX

A

ROTATION MATRICES PROPERITES

A.1 PROPERTIES OF $\mathcal{C}^T \dot{\mathcal{C}}$

$$\begin{aligned}
\mathbf{e}_2 \cdot \dot{\mathbf{e}}_1 &= -\mathbf{e}_1 \cdot \dot{\mathbf{e}}_2 = -\mathbf{e}_1 \cdot (\dot{\mathbf{e}}_3 \wedge \mathbf{e}_1) - \mathbf{e}_1 \cdot (\mathbf{e}_3 \wedge \dot{\mathbf{e}}_1) \\
&= -\dot{\mathbf{e}}_3 \cdot (\mathbf{e}_1 \wedge \mathbf{e}_1) - \mathbf{e}_3 \cdot (\dot{\mathbf{e}}_1 \wedge \mathbf{e}_1) \\
&= -\mathbf{e}_3 \cdot [(\frac{k\mathbf{v} - \dot{k}\mathbf{r}}{k^2}) \wedge (\frac{\mathbf{r}}{k})] \\
&= -\frac{\mathbf{e}_3}{k^2} \cdot (\mathbf{v} \wedge \mathbf{r}) \\
&= -\frac{1}{k^2 h} \underbrace{(\mathbf{r} \wedge \mathbf{v}) \cdot (\mathbf{v} \wedge \mathbf{r})}_{-h^2} \\
&= \frac{h}{k^2}
\end{aligned}$$

$$\begin{aligned}
\mathbf{e}_3 \cdot \dot{\mathbf{e}}_1 &= \frac{\mathbf{r} \wedge \mathbf{v}}{h} \cdot \frac{k\mathbf{v} - \dot{k}\mathbf{r}}{k^2} \\
&= \frac{1}{k^2 h} [k\mathbf{v} \cdot (\mathbf{r} \wedge \mathbf{v}) - \dot{k}\mathbf{r} \cdot (\mathbf{r} \wedge \mathbf{v})] \\
&= 0
\end{aligned}$$

$$\begin{aligned}
\mathbf{e}_3 \cdot \dot{\mathbf{e}}_2 &= \mathbf{e}_3 \cdot (\dot{\mathbf{e}}_3 \wedge \mathbf{e}_1) + \mathbf{e}_3 \cdot (\mathbf{e}_3 \wedge \dot{\mathbf{e}}_1) \\
&= \mathbf{e}_3 \cdot \left[\frac{h(\mathbf{r} \wedge \mathbf{a}) \wedge \mathbf{r} - \dot{h}(\mathbf{r} \wedge \mathbf{v}) \wedge \mathbf{r}}{kh^2} \right] \\
&= \frac{\mathbf{e}_3}{kh^2} \left\{ h[(r^2)\mathbf{a} - (\mathbf{r} \cdot \mathbf{a})\mathbf{r}] - \dot{h}[(r^2)\mathbf{v} - (\mathbf{v} \cdot \mathbf{r})\mathbf{r}] \right\} \\
&= \frac{1}{kh^3} \left\{ h[r^2 \mathbf{a} \cdot (\mathbf{r} \wedge \mathbf{v}) - (\mathbf{r} \cdot \mathbf{a})\mathbf{r} \cdot (\mathbf{r} \wedge \mathbf{v})] \right. \\
&\quad \left. - \dot{h}[r^2 \mathbf{v} \cdot (\mathbf{r} \wedge \mathbf{v}) - (\mathbf{v} \cdot \mathbf{r})\mathbf{r} \cdot (\mathbf{r} \wedge \mathbf{v})] \right\} \\
&= \frac{k}{h^2} \mathbf{a} \cdot (\mathbf{r} \wedge \mathbf{v})
\end{aligned}$$

$$= \frac{k}{h} \mathbf{a} \cdot \mathbf{e}_3$$

where the vectorial triple vector property $(\mathbf{A} \wedge \mathbf{B}) \wedge \mathbf{C} = \mathbf{B}(\mathbf{A} \cdot \mathbf{C}) - \mathbf{A}(\mathbf{B} \cdot \mathbf{C})$ has been exploited.

A.2 PROPERTIES OF $\mathcal{C}^T \ddot{\mathcal{C}}$

$$\begin{aligned}\dot{\mathbf{e}}_1 \cdot \dot{\mathbf{e}}_1 &= \frac{1}{k^4} (k^2 v^2 + k^2 r^2 - 2k \dot{k} \mathbf{v} \cdot \mathbf{r}) \\ &= \frac{1}{k^4} [k^2 v^2 + \frac{r^2}{k^2} (\mathbf{v} \cdot \mathbf{r})(\mathbf{v} \cdot \mathbf{r}) - 2(\mathbf{v} \cdot \mathbf{r})(\mathbf{v} \cdot \mathbf{r})] \\ &= \frac{1}{k^4} [r^2 v^2 - (\mathbf{v} \cdot \mathbf{r})^2] \xrightarrow{\text{Lagrange's identity}} \\ &= \frac{\|\mathbf{v} \wedge \mathbf{r}\|^2}{k^4} \\ &= \left(\frac{h}{k^2} \right)^2\end{aligned}$$

$$\begin{aligned}\dot{\mathbf{e}}_2 \cdot \dot{\mathbf{e}}_2 &= (\dot{\mathbf{e}}_3 \wedge \mathbf{e}_1) \cdot (\dot{\mathbf{e}}_3 \wedge \mathbf{e}_1) + (\mathbf{e}_3 \wedge \dot{\mathbf{e}}_1) \cdot (\mathbf{e}_3 \wedge \dot{\mathbf{e}}_1) \\ &\quad + 2(\mathbf{e}_3 \wedge \dot{\mathbf{e}}_1) \cdot (\dot{\mathbf{e}}_3 \wedge \mathbf{e}_1) \\ &= e_1^2 \dot{e}_3^2 - (\mathbf{e}_1 \cdot \dot{\mathbf{e}}_3)^2 + e_3^2 \dot{e}_1^2 - (\mathbf{e}_3 \cdot \dot{\mathbf{e}}_1)^2 + 2(\dot{\mathbf{e}}_3 \cdot \mathbf{e}_3)(\dot{\mathbf{e}}_1 \cdot \mathbf{e}_1) \\ &\quad - 2(\mathbf{e}_1 \cdot \mathbf{e}_3)(\dot{\mathbf{e}}_1 \cdot \dot{\mathbf{e}}_3) \\ &= \dot{e}_1^2 + \dot{e}_3^2\end{aligned}$$

where the vectorial identity $(\mathbf{A} \wedge \mathbf{B}) \cdot (\mathbf{C} \wedge \mathbf{D}) = (\mathbf{A} \cdot \mathbf{C})(\mathbf{B} \cdot \mathbf{D}) - (\mathbf{B} \cdot \mathbf{C})(\mathbf{A} \cdot \mathbf{D})$ and the direction properties of versors have been used.

$$\begin{aligned}\dot{\mathbf{e}}_3 \cdot \dot{\mathbf{e}}_3 &= \frac{h^2 \|\mathbf{r} \wedge \mathbf{a}\|^2 + \dot{h}^2 \|\mathbf{r} \wedge \mathbf{v}\|^2 - 2h \dot{h} (\mathbf{r} \wedge \mathbf{a}) \cdot (\mathbf{r} \wedge \mathbf{v})}{h^4} \\ &= \frac{1}{h^4} \left[h^2 \|\mathbf{r} \wedge \mathbf{a}\|^2 + \frac{1}{h^2} \|(\mathbf{r} \wedge \mathbf{v}) \cdot (\mathbf{r} \wedge \mathbf{a})\|^2 \|\mathbf{r} \wedge \mathbf{v}\|^2 \right. \\ &\quad \left. - 2 \|(\mathbf{r} \wedge \mathbf{v}) \cdot (\mathbf{r} \wedge \mathbf{a})\|^2 \right] \\ &= \frac{1}{h^4} \left[\|\mathbf{r} \wedge \mathbf{v}\|^2 \|\mathbf{r} \wedge \mathbf{a}\|^2 - \|(\mathbf{r} \wedge \mathbf{v}) \cdot (\mathbf{r} \wedge \mathbf{a})\|^2 \right] \\ &= \frac{\|(\mathbf{r} \wedge \mathbf{v}) \wedge (\mathbf{r} \wedge \mathbf{a})\|^2}{h^4}\end{aligned}$$

$$\begin{aligned}
\dot{\mathbf{e}}_2 \cdot \dot{\mathbf{e}}_1 &= \dot{\mathbf{e}}_1 \cdot (\dot{\mathbf{e}}_3 \wedge \mathbf{e}_1) + \dot{\mathbf{e}}_1 \cdot (\mathbf{e}_3 \wedge \dot{\mathbf{e}}_1) \\
&= \frac{\mathbf{e}_1}{(kh)^2} \cdot \{(kv - kr) \wedge [h(r \wedge a) - \dot{h}(r \wedge v)]\} \xrightarrow{\mathbf{e}_1 \parallel \mathbf{r}} \\
&= \frac{\mathbf{e}_1}{(kh)^2} \cdot [khv \wedge (r \wedge a) - khv \wedge (r \wedge v)] \\
&= \frac{\mathbf{r}}{(kh)^2} \cdot \{h[r(v \cdot a) - a(v \cdot r)] - \dot{h}[v^2 r - v(r \cdot v)]\} \\
&= \frac{1}{(kh)^2} \{h[r^2(v \cdot a) - (a \cdot r)(v \cdot r)] \\
&\quad - \frac{1}{h} [(r \wedge v) \cdot (r \wedge a)][r^2 v^2 - (r \cdot v)^2]\} \\
&= \frac{r^2(v \cdot a) - (a \cdot r)(v \cdot r) - (r \wedge v) \cdot (r \wedge a)}{k^2 h} \\
&= 0
\end{aligned}$$

$$\begin{aligned}
\dot{\mathbf{e}}_3 \cdot \dot{\mathbf{e}}_1 &= \frac{kv - kr}{k^2} \cdot \frac{h(r \wedge a) - \dot{h}(r \wedge v)}{h^2} \\
&= \frac{\mathbf{v} \cdot (r \wedge a)}{kh} = -\frac{\mathbf{a}}{k} \cdot \frac{\mathbf{r} \wedge \mathbf{v}}{h} \\
&= -\frac{1}{k} \mathbf{a} \cdot \mathbf{e}_3
\end{aligned}$$

$$\begin{aligned}
\dot{\mathbf{e}}_3 \cdot \dot{\mathbf{e}}_2 &= \dot{\mathbf{e}}_3 \cdot (\dot{\mathbf{e}}_3 \wedge \mathbf{e}_1) + \dot{\mathbf{e}}_3 \cdot (\mathbf{e}_3 \wedge \dot{\mathbf{e}}_1) \\
&= \frac{\mathbf{e}_3}{(kh)^2} \cdot \{(kv - kr) \wedge [h(r \wedge a) - \dot{h}(r \wedge v)]\} \xrightarrow{\mathbf{e}_3 \parallel (r \wedge v)} \\
&= \frac{\mathbf{r} \wedge \mathbf{v}}{(kh)^2} \cdot [kv \wedge (r \wedge a) - kr \wedge (r \wedge a)] \\
&= \frac{\mathbf{r} \wedge \mathbf{v}}{(kh)^2} \cdot \{k[r(v \cdot a) - a(v \cdot r)] - \dot{k}[r(a \cdot r) - r^2 a]\} \\
&= \frac{kr^2 - k(v \cdot r)}{(kh)^2} \mathbf{a} \cdot (r \wedge v) \\
&= 0
\end{aligned}$$

B

FOURIER ANALYSIS

This chapter is intended to provide a brief introduction of the ubiquitous Fourier transform theory, closely following the discussion in Brigham [8]. The term ubiquitous means to be everywhere at the same time. Because of the great variety of seemingly unrelated topics which can be effectively dealt with using the Fourier transform, the modifier ubiquitous is certainly appropriate. Typical application of the Fourier transform include linear systems, antennas (sensitive topic in space system design), optics, stochastic processes and chaos, quantum physics and boundary-value problems in the general form. In this thesis the Fourier transform is used firstly in Section 3.3 to analyse the harmonic content of the motion equations coefficients, and then in Chapter 5 to exploit the harmonic portrait of the dynamical problem at hand in order to improve convergence and speed properties of the multiple shooting technique.

The concept behind the Fourier transform in general is the *transform analysis*: the problem is cast in a simpler and more convenient form by means of a properly chosen transformation function. The problem is then solved in this new simplified form and the solution is eventually transformed back through a simple function inversion, provided the transformation function and its inverse are well-defined (i.e., existence and differentiability) in the domain of the solution.

B.1 THE FOURIER INTEGRAL: A CONTINUOUS REPRESENTATION

The essence of the Fourier transform of a waveform is to decompose or separate the waveform into a sum of sinusoids of different frequencies. If these sinusoids sum exactly to the original waveform the Fourier transform has been found. The pictorial representation of the Fourier transform is typically a diagram which displays the amplitude and frequency of each of the determined sinusoids. For this reason, diagrams often display a collection of arrows at the prescribed frequencies. However, if the function is not periodic, then the Fourier transform will be a continuous function and the harmonic content of the function is unbounded (i.e., the Fourier transform is a summation of sinusoids of all frequencies).

In the traditional sense, the Fourier transform is a *frequency domain representation* of a function, opposed to the common time domain representation. Note that the Fourier transform contains exactly the same information as that of the original function, they differ only in the manner information is presented.

The Fourier integral is defined by the expression:

$$H(f) = \int_{-\infty}^{\infty} h(t)e^{-2\pi jft} dt \quad (B.1)$$

where $h(t)$ is the waveform to be decomposed into a sum of sinusoids, $j = \sqrt{-1}$ is the imaginary unit, and $H(f)$ is the Fourier transform of $h(t)$, provided the integral exists for every value of the parameter f . Adopting the common terminology, t stands for time variable and f is the frequency. In general, the Fourier transform is a complex quantity, $H(f) \in \mathbb{C}$. It can therefore be split into its real and imaginary component:

$$H(f) = R(f) + jI(f) = |H(f)|e^{j\vartheta(f)} \quad (B.2)$$

where $|H(f)| = \sqrt{(R(f)^2 + I(f)^2)}$ is the amplitude of the Fourier spectrum of $h(t)$, and $\vartheta(f) = \tan^{-1} \frac{I(f)}{R(f)}$ is the phase angle of the Fourier transform.

The inverse Fourier transform is defined as:

$$h(t) = \int_{-\infty}^{\infty} H(f)e^{2\pi jft} df \quad (B.3)$$

If functions $h(t)$ and $H(f)$ are related by Eqs. (B.1) and (B.3), the two functions are termed *Fourier transform pair*, identified here as $h(t) \leftrightarrow H(f)$.

To this point, the validity of the Fourier transform and its inverse have not been studied, assuming the integral equations to be well defined for all functions. It's important therefore to point out conditions for the existence of the Fourier integral and its inverse. Without giving detailed proofs, hereafter three conditions for the existence of the FT are shown.

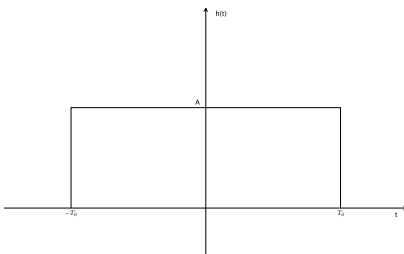
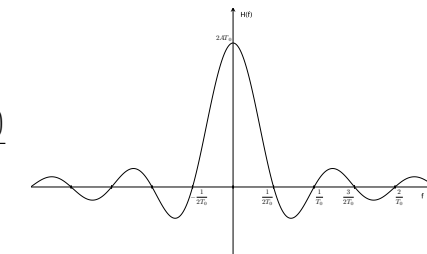
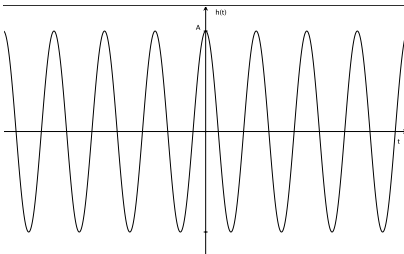
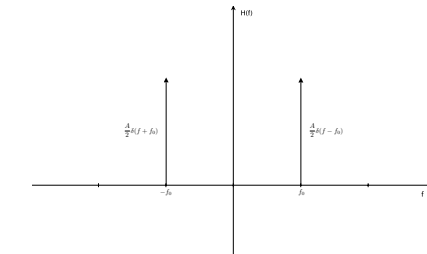
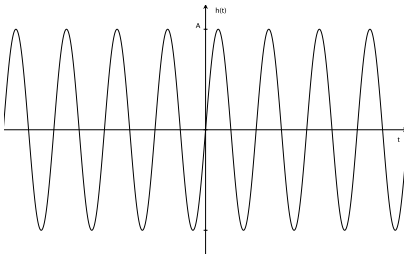
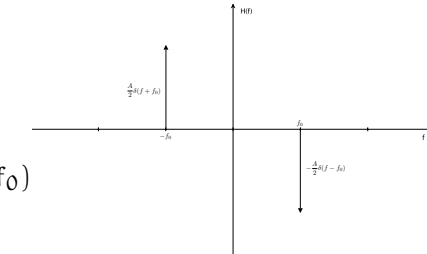
Condition B.1 (sufficient). If $h(t)$ is integrable in the sense

$$\int_{-\infty}^{\infty} |h(t)| dt < \infty \quad (B.4)$$

then its Fourier transform $H(f)$ exists and satisfies the inverse Fourier transform, (B.3).

Condition B.2. If $h(t) = \beta(t) \sin(2\pi ft + \alpha)$ (f and α are arbitrary constants), if $\beta(t+k) < \beta(t)$, and if for $|t| > \lambda > 0$ the function $\frac{h(t)}{t}$ is absolutely integrable in the sense of (B.4), then $H(f)$ exists and satisfies the inverse Fourier transform, (B.3).

Table B.1: Some Fourier transform pairs

Time domain	Fourier pair	Frequency domain
	$h(t) = \begin{cases} A & t < T_0 \\ \frac{A}{2} & t = T_0 \\ 0 & t > T_0 \end{cases} \quad \mathcal{N} \quad H(f) = 2AT_0 \frac{\sin(2\pi T_0 f)}{2\pi T_0 f}$	
	$h(t) = A \cos(2\pi f_0 t) \quad \mathcal{N} \quad H(f) = \frac{A}{2} \delta(f - f_0) + \frac{A}{2} \delta(f + f_0)$	
	$h(t) = A \sin(2\pi f_0 t) \quad \mathcal{N} \quad H(f) = -j \frac{A}{2} \delta(f - f_0) + j \frac{A}{2} \delta(f + f_0)$	

Continues in the next page

Follows from previous page

Time domain	Fourier pair	Frequency domain
	$h(t) = K \quad \mathcal{N} \quad H(f) = K\delta(f)$	
	$h(t) = \sum_{n=-\infty}^{\infty} \delta(t - nT) \quad \mathcal{N} \quad H(f) = \frac{1}{T} \sum_{n=-\infty}^{\infty} \delta(f - \frac{n}{T})$	
	$h(t) = \begin{cases} \frac{1}{2} [1 + \cos(\frac{\pi t}{T_0})] & t < T_0 \\ 0 & t > T_0 \end{cases} \quad \mathcal{N} \quad H(f) = \frac{1}{2} Q(f) + \frac{1}{4} [Q(f + \frac{1}{2T_0}) + Q(f - \frac{1}{2T_0})]$ $Q(f) = \frac{2\pi T_0 f}{\pi f}$	

Concluded from previous page

Condition B.3 (Distribution theory). If $h(t)$ is a periodic or impulse function¹, then $H(f)$ exists only if one introduces the *theory of distribution*, thoroughly explained in Zemanian [51]. The main results of the theory of distribution are:

$$\int_{-\infty}^{\infty} \delta(t - t_0)x(t)dt = x(t_0) \quad \text{where } x(t_0^-) = x(t_0^+) \quad (\text{B.5})$$

$$\int_{-\infty}^{\infty} e^{2\pi jft} df = \underbrace{\int_{-\infty}^{\infty} \cos(2\pi ft) df}_{=0} + j \underbrace{\int_{-\infty}^{\infty} \sin(2\pi ft) df}_{\text{odd function}} = \delta(t) \quad (\text{B.6})$$

Equation (B.5) is also known as *sifting property*. In addition, note how the first integral in (B.6) is meaningless unless it is interpreted in the sense of distribution theory.

Although not specifically stated, all functions for which Conditions B.1 and B.2 hold are assumed to be of *bounded variation*: that is, they can be represented by a curve of finite length in any finite time interval. By means of Condition B.3 the theory is extended to include singular (impulse) functions. In Table B.1 some commonly used Fourier pairs are graphically and analytically shown.

The Fourier transform enjoys a few properties which are basic to a thorough understanding. These fundamental properties are here briefly displayed in Table B.2, without claim of demonstration.

Table B.2: Main properties of the Fourier transform

Time domain	Fourier pair	Frequency domain
Linearity	$x(t) \pm y(t) \xrightarrow{\mathcal{F}} X(f) \pm Y(f)$	Linearity
Symmetry	$H(t) \xrightarrow{\mathcal{F}} h(-f)$	Symmetry
Time scaling	$h(kt) \xrightarrow{\mathcal{F}} \frac{1}{k}H(\frac{f}{k})$	Inverse scale change
Inverse scale change	$\frac{1}{k}h(\frac{t}{k}) \xrightarrow{\mathcal{F}} H(kf)$	Frequency scaling
Time shifting	$h(t - t_0) \xrightarrow{\mathcal{F}} H(f)e^{-j2\pi ft_0}$	Phase shift
Modulation	$h(t)e^{j2\pi tf_0} \xrightarrow{\mathcal{F}} H(f - f_0)$	Frequency shifting

¹ Normally the impulse function, or δ -function, is defined as

$$\begin{aligned} \delta(t - t_0) &= 0 \quad t \neq t_0 \\ \int_{-\infty}^{\infty} \delta(t - t_0) dt &= 1 \end{aligned}$$

That is, the δ -function has undefined magnitude at occurrence time and zero elsewhere, with the additional property that function subtended area is unity. The physical interpretation of an impulse is a *pulse waveform* of very large magnitude and infinitesimal small duration applied at t_0 .

There exists a class of Fourier transform relationships whose importance far outranks those considered so far: the *convolution* and the *correlation*. More attention is dedicated to these properties, again without proof. The convolution $y(t)$ of the functions $x(t)$ and $h(t)$ is defined as:

$$y(t) = \int_{-\infty}^{\infty} x(\tau)h(t - \tau)d\tau = \int_{-\infty}^{\infty} h(\tau)x(t - \tau)d\tau = x(t) * h(t) \quad (\text{B.7})$$

The commutative property is easily demonstrated by means of a variable change. On the other hand, the correlation $\rho_{x,h}$ (following the statistical analysis notation) of the functions $x(t)$ and $h(t)$ is defined as:

$$\rho_{x,h}(t) = \int_{-\infty}^{\infty} x(\tau)h(t + \tau)d\tau \quad (\text{B.8})$$

The convolution is widely used in the field of linear systems of differential equation and state-space representation theory, whilst the correlation is extensively used in stochastic and probability analysis.

Convolution theorem B.1. *If $h(t)$, $H(f)$ and $x(t)$, $X(f)$ are well defined Fourier transform pairs, then the time domain convolution of these two functions is the straight multiplication in the frequency domain. The opposite is also true: a product in the time domain is tantamount to a convolution in the frequency ‘world’.*

$$\begin{aligned} h(t) * x(t) &\propto H(f)X(f) \\ h(t)x(t) &\propto H(f) * X(f) \end{aligned} \quad (\text{B.9})$$

Correlation theorem B.2. *Let $z(t)$ be the correlation of the functions $x(t)$ and $h(t)$, and $X(f)$ and $H(f)$ their well-defined Fourier transforms; then the Fourier transform of $z(t)$ yields a simple multiplication in the frequency domain, provided $H(f)$ is first conjugated.*

$$\begin{aligned} z(t) &= \int_{-\infty}^{\infty} x(\tau)h(t + \tau)d\tau \propto Z(f) \\ Z(f) &= H(f)X^*(f) \end{aligned} \quad (\text{B.10})$$

B.2 THE FOURIER INTEGRAL: A DISCRETE REPRESENTATION

With the era of fast digital computers and efficient data acquisition systems, in most cases the Fourier transform has to deal with sampled or discretised waveforms. The sole knowledge of a function per points requires the definition of the Fourier analysis to be revisited, and extra care must be applied when reconstructing the analytic function form its sampled form, both in time

and frequency domain. In this section the framework for the development of the *discrete Fourier transform*, or DFT, is set forth. In particular the theory of waveform sampling will be outlined through basic notions and theorems.

In the preceding section, the major tools to address both continuous and impulse functions have been outlined. Based on these developments, it's quite straightforward to extend the theory to include sampled waveform in the Fourier analysis. If the function $h(t)$ is continuous at $t = T$, then the sample of $h(t)$ at time T is simply expressed by

$$\hat{h}(t) = h(t)\delta(t - T) = h(T)\delta(t - T) \quad (\text{B.11})$$

where the product is interpreted in the sense of distribution theory. The impulse occurring at T has the amplitude to the function at time T . If $h(t)$ is continuous at $t = nT$ for $n = 0, \pm 1, \pm 2, \dots$, then

$$\hat{h}(t) = \sum_{n=-\infty}^{\infty} h(nT)\delta(t - nT) \quad (\text{B.12})$$

is termed the sampled waveform of $h(t)$ with sample interval equal to T . It is clear at this point, that a sampled waveform can be viewed as an infinite sequence of equidistant impulses, each of whose amplitude is given by the value of $h(t)$ corresponding to the time of occurrence of the impulse. Since Eq. (B.12) is the product of the continuous function $h(t)$ and the sequence of impulses, its Fourier transform can be derived by application of the convolution theorem B.9. Let $\xi(t)$ be the sampling function, that is the sequence of infinite impulses separated by T , and $\Xi(f)$ its Fourier transform, as shown in the fifth row of Table B.1; then the Fourier transform of the sampled waveform is obtained as convolution of $H(f)$ and $\Xi(f)$:

$$F\{\hat{h}(t)\} = H(f) * \Xi(f) \quad (\text{B.13})$$

where by $F\{\cdot\}$ is indicated the Fourier transform. The Fourier transform of the sampled waveform is a periodic, where one period is equal, within a constant, to the Fourier transform of the continuous function $h(t)$ ². It is rather intuitive to think that the sampling time T must be chosen sufficiently small, if one wishes to represent coherently a continuous function by means of a discretisation. This idea is mathematically formulated in the following theorem.

Shannon sampling theorem B.3. *Let $h(t)$ and $H(f)$ be a well-defined Fourier pair; if $H(f)$ is zero for all frequency above a certain value f_c , then the continuous function*

² This statement is strictly valid only if the sampling interval T is ‘sufficiently’ small.

$h(t)$ can be uniquely determined from a knowledge of its sampled values. Furthermore, if $T \leq \frac{1}{2f_c}$ in Eq. (B.12), then:

$$h(t) = T \sum_{n=-\infty}^{\infty} h(nT) \frac{\sin[2\pi f_c(t - nT)]}{\pi(t - nT)} \quad (\text{B.14})$$

Analogously, if the function $h(t)$ is time-limited, that is $h(t) = 0$ for $|t| > T_c$, then its Fourier transform $H(f)$ can be uniquely determined from equidistant samples of $H(f)$. In particular, $H(f)$ is given by

$$H(f) = \frac{1}{2T_c} \sum_{n=-\infty}^{\infty} H\left(\frac{n}{2T_c}\right) \frac{\sin[2\pi T_c(f - \frac{n}{2T_c})]}{\pi(f - \frac{n}{2T_c})} \quad (\text{B.15})$$

There are two necessary constraints for the validity of Theorem B.3. The first requires the function $h(t)$ to be *band-limited* at the frequency f_c : in other terms it must be that $H(f)$ is zero for $|f| > f_c$. The second constraint is about the sample spacing, to be chosen smaller or at least equal to $\frac{1}{2f_c}$. In other terms, the impulse functions in $\Xi(f)$ are required to be separated by at least $f_N = 2f_c$, known as *Nyquist sampling frequency*. This spacing assures that, when $\Xi(f)$ and $H(f)$ are convolved there will be no *aliasing*. In particular, any frequency greater than f_c (if present), will be aliased to a frequency less than f_c and it's undistinguishable from the others³. There is no other way of reducing aliasing other than reducing the sampling rate. It is clear that this reduction has limits, mainly related to the size of the corresponding sampled waveform. Aliasing is then inevitable. A common method to tackle this problem is to 'delete' all the frequencies above a certain value, the so-called *cut frequency*, by means of a wisely selected *low-pass filter*. After a fine tuning of the filter, all the frequencies above the cut one will not influence the Fourier transform, but at the same time no information will be included on this harmonic content.

THE DISCRETE FOURIER TRANSFORM At this point it is desirable to modify the Fourier transform pair in such a manner that the pair is amenable to digital computation. On top of sampling the continuous function to obtain a discrete set of impulses, machine computation further requires the sampled waveform to be of finite size. It is necessary to truncate the sampled waveform by means of a *window function* (for example a rectangular pulse) of width T_0 . Finally, the frequency transform obtained after applying the windowing must be represented by discrete values, and therefore shall be sampled in turn. Thanks to this process both $h(t)$ and $H(f)$ are approximated by N samples. These samples define the discrete Fourier transom pair and approximate the original

³ If the Fourier transform of a continuous function is not band-limited, then all the harmonic content at higher frequency than the Nyquist critical frequency will be amenable to aliasing.

one. Note that sampling in time results in a periodic function of frequency, and sampling in frequency results in aperiodic function of time. Hence, the DFT requires that both the original time and frequency functions be modified such that they become periodic functions.

Let T be the sampling time and N the number of equidistant samples within T_0 , then the Fourier discrete transform yields:

$$\tilde{H}\left(\frac{n}{NT}\right) = \sum_{k=0}^{N-1} h(kT)e^{-j2\pi n \frac{k}{N}} \quad n = 0, 1, \dots, N-1 \quad (\text{B.16})$$

The DFT, $\tilde{H}\left(\frac{n}{NT}\right)$, is periodic with period T_0 which consists of N samples.

Truncation introduces a second source of error, a part from aliasing, in the Fourier transform: this effect is to convolve the aliased frequency transform with the FT of the window function. Graphically, this creates ripples in the frequency transform.

Another common phenomenon that might compromise the validity of the results of the discrete Fourier transform is the *leakage*. For periodic functions, when the length T_0 of the time interval spanned by the samples is not an integer multiple of the period of the function, there appear in the Fourier transform spurious frequencies, that is the frequency transform is different from zero at frequencies not being multiple of the function frequency. Another way to view the same phenomenon is to think the Fourier transform to induce substantial changes to the spectrum of the continuous function, namely the spectrum is discretised as well along with the transform. It is remarkable that leakage can affect also the results of the continuous Fourier transform, provided the original function is somehow truncated. A common strategy to reduce leakage is to carefully select the window function. Example would be the *Hanning window function*. The Hanning function of order n_h is defined as:

$$H_{T_0}^{n_h}(t) = q_{n_h} \left(1 - \cos \frac{2\pi t}{T_0}\right)^{n_h} \quad (\text{B.17a})$$

$$q_{n_h} = \frac{n_h!}{(2n_h - 1)!!} \quad (\text{B.17b})$$

The Hanning function of order 1 is shown in the last row of Table B.1, with a slight scalar modification⁴. The advantages of the Hanning function with respect to other well-known window functions are its simplicity and its degree of differentiability. For instance, $H_{T_0}^n(t)$ has degree $2n$, whereas a general triangle

⁴ The double factorial in Eq. (B.17b), indicated by two exclamation marks, is defined as

$$(2k-1)!! = \prod_{i=1}^k (2i-1)$$

window function has degree just equal to n . This higher degree of regularity implies a faster decay of the Fourier coefficients.

B.3 A REFINED FOURIER ANALYSIS

Ultimately, the Fourier analysis provides a powerful tool to approximate a quasi-periodic function by means of a trigonometric polynomial. The problem at hand can be expressed as follows: given the N samples $\{h(t_k)\}_{k=0}^{N-1}$ of a real-valued quasi-periodic function $h(t)$, which are assumed to be uniformly distributed in the interval $[0, T_0]$, $t_k = \frac{kT_0}{N} \in [0, T_0]$, a trigonometric polynomial approximation with a fixed number of frequencies N_f is sought:

$$Q_h(t) = A_0^c + \sum_{k=1}^{N_f} (A_k^c \cos \frac{2\pi f_k t}{T_0} + A_k^s \sin \frac{2\pi f_k t}{T_0}) \quad (\text{B.18})$$

The unknowns are the $2N_f + 1$ sinusoids coefficients, $\{A_k^c\}_{k=0}^{N_f}$ and $\{A_k^s\}_{k=1}^{N_f}$, and the set of N_f frequencies to be retained, $\{f_k\}_{k=1}^{N_f}$. In total there are $3N_f + 1$ unknowns that have to be determined using the Fourier transform theory.

The procedure has been thoroughly studied, implemented and validated by the ‘Barcelona group’ in Gómez et al. [18]. The iterative procedure consists in three steps that are briefly summarised here.

- (1) Get a first approximation of the frequencies, looking at the maxima of the filtered DFT magnitude;
- (2) Compute the related amplitudes assuming known frequencies;
- (3) Perform a simultaneous improvement of both frequencies and amplitudes.

The basic idea underlying the method is to ask for the equality between the DFT of the sampled initial function and the DFT of its quasi-periodic approximation. Moreover, the procedure is iterative because the number of frequencies N_f to be retained is not known a priori. The number of frequencies is therefore increased iteratively until a prescribed tolerance is met or the N_f becomes too large.

BIBLIOGRAPHY

- [1] Gtoc portal. URL http://sophia.estec.esa.int/gtoc_portal/. (Cited on page 6.)
- [2] E. Belbruno. Random walk in celestial mechanics. *Regular and Chaotic Dynamics*, 14(1):7–17, 2009. (Cited on page 7.)
- [3] Edward Belbruno. *Capture dynamics and chaotic motions in celestial mechanics: With applications to the construction of low energy transfers*. Princeton University Press, 2004. (Cited on page 11.)
- [4] Edward Belbruno. Low energy trajectories and chaos: Applications to astrodynamics and dynamical astronomy. *Annals of the New York Academy of Sciences*, 1065(1):1–14, 2005. (Cited on page 6.)
- [5] Edward Belbruno, Marian Gidea, and Francesco Topputo. Weak stability boundary and invariant manifolds. *SIAM Journal on Applied Dynamical Systems*, 9(3):1061–1089, 2010. (Cited on page 6.)
- [6] Edward A. Belbruno and James K. Miller. Sun-perturbed earth-to-moon transfers with ballistic capture. *Journal of Guidance, Control, and Dynamics*, 16(4):770–775, 1993. (Cited on page 7.)
- [7] John T. Betts. *Practical methods for optimal control and estimation using nonlinear programming*, volume 19. Siam, 2010. (Cited on page 108.)
- [8] E. Oran Brigham. *The fast Fourier transform*. Englewood Cliffs : Prentice-Hall, 1974. (Cited on page 135.)
- [9] C. C. Conley. Low energy transit orbits in the restricted three-body problems. *SIAM Journal on Applied Mathematics*, 16(4):732–746, 1968. (Cited on page 7.)
- [10] Bruce A. Conway. *Spacecraft trajectory optimization*, volume 32. Cambridge University Press Cambridge, UK, 2010. (Cited on page 108.)
- [11] Howard Curtis. *Orbital mechanics for engineering students*. Butterworth-Heinemann, 2013. (Cited on pages xi, 13, and 18.)
- [12] Robert L. Devaney, Luke Devaney, and Luke Devaney. *An introduction to chaotic dynamical systems*, volume 6. Addison-Wesley Reading, 1989. (Cited on page 3.)

- [13] John Earman, Michel Janssen, and John D. Norton. *The attraction of gravitation: new studies in the history of general relativity*, volume 5. Springer, 1993. (Cited on page 3.)
- [14] William M. Folkner, James G. Williams, Dale H. Boggs, Ryan S. Park, and Petr Kuchynka. The planetary and lunar ephemerides de430 and de431. Technical report, JPL Interplanetary Network Progress Report 42-196, 2014. (Cited on page 72.)
- [15] Bernard Friedland. *Control system design: an introduction to state-space methods*. Courier Dover Publications, 2005. (Cited on page 32.)
- [16] Izrail Moiseevich Gelfand and Sergei Vasil'evich Fomin. *Calculus of variations*. Courier Dover Publications, 2000. (Cited on page 111.)
- [17] G. Gómez, A. Jorba, J. Masdemont, and C. Simó. Study refinement of semi-analytical halo orbit theory. *Final Report, ESOC Contract*, 1991. (Cited on page 7.)
- [18] G. Gómez, J. M. Mondelo, and C. Simó. Refined fourier analysis: procedures, error estimates and applications. *Preprint*, 2001. (Cited on page 144.)
- [19] G. Gómez, J. Masdemont, and J. M. Mondelo. Libration point orbits: a survey from the dynamical point of view. In *Libration point orbits and applications, Proceedings of the Conference Aiguablava, Spain*, pages 10–14, 2002. (Cited on pages 7 and 40.)
- [20] G. Gómez, J. J. Masdemont, and J. M. Mondelo. Solar system models with a selected set of frequencies. *ASTRONOMY AND ASTROPHYSICS-BERLIN-*, 390(2):733–750, 2002. (Cited on pages 4 and 116.)
- [21] G. Gómez, J. J. Masdemont, and J. M. Mondelo. Dynamical substitutes of the libration points for simplified solar system models. In *Libration Point Orbits and Applications: Proceedings of the Conference, Aiguablava, Spain, 10-14 June 2002*, page 373. World Scientific, 2003. (Cited on page 7.)
- [22] Gerard Gómez. *Dynamics and Mission Design Near Libration Points: Volume 3, Advanced Methods for Collinear Points*. World Scientific, 2001. (Cited on page 53.)
- [23] Gerard Gómez and José María Mondelo. The dynamics around the collinear equilibrium points of the rtbp. *Physica D: Nonlinear Phenomena*, 157(4):283–321, 2001. (Cited on page 7.)
- [24] X. Y. Hou and L. Liu. On quasi-periodic motions around the collinear libration points in the real earth-moon system. *Celestial Mechanics and Dynamical Astronomy*, 110(1):71–98, 2011. (Cited on pages 7 and 116.)

- [25] Nicola Hyeraci and Francesco Topputo. Method to design ballistic capture in the elliptic restricted three-body problem. *Journal of guidance, control, and dynamics*, 33(6):1814–1823, 2010. (Cited on page 6.)
- [26] Dario Izzo. Lambert’s problem for exponential sinusoids. *Journal of guidance, control, and dynamics*, 29(5):1242–1245, 2006. (Cited on page 6.)
- [27] William H. Jefferys. Julian day numbers, 1998. URL <http://quasar.as.utexas.edu/BillInfo/JulianDatesG.html>. (Cited on page 76.)
- [28] Angel Jorba and Josep Masdemont. Dynamics in the center manifold of the collinear points of the restricted three body problem. *Physica D: Nonlinear Phenomena*, 132(1):189–213, 1999. (Cited on pages 7, 33, and 39.)
- [29] Yijun Lian, Gerard Gómez, Josep J. Masdemont, and Guojian Tang. A note on the dynamics around the lagrange collinear points of the earth-moon system in a complete solar system model. *Celestial Mechanics and Dynamical Astronomy*, 115(2):185–211, 2013. (Cited on pages 7, 99, 108, and 116.)
- [30] Malcolm Longair. A history of astronomy, astrophysics and cosmology. Encyclopedia of Life Support Systems (EOLSS). (Cited on page 1.)
- [31] J. Masdemont and J. M. Mondelo. Notes for the numerical and analytical techniques lectures (draft version). *Advanced Topics in Astrodynamics Summer Course, Barcelona*, 2004. (Cited on page 39.)
- [32] Kenneth Ray Meyer, Glen R. Hall, and Daniel Clyde Offin. *Introduction to Hamiltonian dynamical systems and the N-body problem*, volume 90. Springer, 1992. (Cited on pages 3 and 33.)
- [33] G. Mingotti. *Trajectory Design and Optimization in Highly Nonlinear Astrodynamics*. PhD thesis, PhD thesis, Politecnico di Milano, Milano, Italy, 2010. (Cited on page 24.)
- [34] Anton Pannekoek. *A history of astronomy*. Courier Dover Publications, 1989. (Cited on page 1.)
- [35] Anastassios E. Petropoulos and Jon A. Sims. A review of some exact solutions to the planar equations of motion of a thrusting spacecraft. In *2nd International Symposium Low Thrust Trajectories*, 2002. (Cited on page 6.)
- [36] David L. Richardson. Analytic construction of periodic orbits about the collinear points. *Celestial mechanics*, 22(3):241–253, 1980. (Cited on page 39.)
- [37] Lawrence F. Shampine and Mark W. Reichelt. The matlab ode suite. *SIAM journal on scientific computing*, 18(1):1–22, 1997. (Cited on page 70.)

- [38] Carl L Siegel, Jürgen K Moser, and Jürgen Moser. *Lectures on celestial mechanics*, volume 187. Springer, 1995. (Cited on page 121.)
- [39] E. M. Standish. Jpl planetary and lunar ephemerides, de405/le405. Interoffice memorandum IOM 312.F - 98 -84, Jet Propulsion Laboratory, August 26 1998. (Cited on page 72.)
- [40] Josef Stoer and Roland Bulirsch. *Introduction to numerical analysis*, volume 12. Springer, 2002. (Cited on pages 67 and 99.)
- [41] Steven H. Strogatz. *Nonlinear dynamics and chaos (with applications to physics, biology, chemistry a*. Perseus Publishing, 2006. (Cited on page 3.)
- [42] John Staelnagel. On the parametrization of the three-dimensional rotation group. *SIAM review*, 6(4):422–430, 1964. (Cited on page 50.)
- [43] Endre Süli and David F. Mayers. *An introduction to numerical analysis*. Cambridge university press, 2003. (Cited on page 70.)
- [44] Victor Szebehely. Theory of orbits: the restricted problem of three bodies. Technical report, DTIC Document, 1967. (Cited on pages 22 and 31.)
- [45] Guojian Tang, Gerard Gomez Muntaner, Josep Masdemont Soler, L. Yijun, et al. A note on the dynamics around the l₁, 2 lagrange points of the earth-moon system in a complete solar system model. *Springer Science+Business Media Dordrecht 2013*, January 2012. (Cited on page 7.)
- [46] Francesco Toppato. *Low-thrust non-Keplerian orbits: analysis, design, and control*. PhD thesis, Politecnico di Milano. Dipartimento di ingegneria aerospaziale, 2007. (Cited on pages 24 and 38.)
- [47] Francesco Toppato. On optimal two-impulse earth–moon transfers in a four-body model. *Celestial Mechanics and Dynamical Astronomy*, 117(3):279–313, 2013. (Cited on page 7.)
- [48] David A. Vallado. *Fundamentals of astrodynamics and applications*, volume 12. Springer, 2001. (Cited on page 11.)
- [49] Harry Varvoglis. Solar system dynamics, beyond the two-body-problem approach. In *Recent Advances in Astronomy and Astrophysics: 7 th International Conference of the Hellenic Astronomical Society(AIP Conference Proceedings Volume 848)*, volume 848, pages 613–626, 2006. (Cited on page 7.)
- [50] Bradley J. Wall and Bruce A. Conway. Shape-based approach to low-thrust rendezvous trajectory design. *Journal of Guidance, Control, and Dynamics*, 32(1):95–101, 2009. (Cited on page 6.)
- [51] Armen H. Zemanian. *Distribution theory and transform analysis: an introduction to generalized functions, with applications*. Courier Dover Publications, 1965. (Cited on page 139.)

COLOPHON

This document was typeset using the typographical look-and-feel `classicthesis` developed by André Miede and adjusted by Diogene Alessandro Dei Tos. The style was inspired by Robert Bringhurst's seminal book on typography *The Elements of Typographic Style*.

`classicthesis` is available for both L^AT_EX and L_YX:

<http://code.google.com/p/classicthesis/>

DECLARATION

I hereby declare that this thesis is my original work, it has not been subject to plagiarism, and has not been presented for a degree in any other University.

Milano, July 2014



Diogene Alessandro Dei Tos